

2013•2014
FACULTEIT INDUSTRIËLE INGENIEURSWETENSCHAPPEN
master in de industriële wetenschappen: elektronica-ICT

Masterproef

Flash photography vision system for inkjet drop formation characterization

Promotor :
dr. Jan GENOE

Promotor :
Prof. dr. ir. WIM DEFERME

Copromotor :
Ing. GLEN VANDEVENNE

Gezamenlijke opleiding Universiteit Hasselt en KU Leuven

Steven Nagels

Proefschrift ingediend tot het behalen van de graad van master in de industriële wetenschappen: elektronica-ICT

2013•2014

Faculteit Industriële

ingenieurswetenschappen

master in de industriële wetenschappen: elektronica-ICT

Masterproef

Flash photography vision system for inkjet drop
formation characterization

Promotor :
dr. Jan GENOE

Promotor :
Prof. dr. ir. WIM DEFERME

Copromotor :
Ing. GLEN VANDEVENNE

Steven Nagels

*Proefschrift ingediend tot het behalen van de graad van master in de industriële
wetenschappen: elektronica-ICT*

Acknowledgements

First of all, I would like to express my very great appreciation to both of my promoters, Jan Genoe and Wim Deferme, for their patience, encouragement and general enthusiasm while guiding me through this Master's year. Jan's deep insights and strength in problem-solving helped me overcome problems which at first seemed insurmountable. Wim always took time to listen to my questions and kept his office door open, including for a casual chat. Subsequently, assistance given by Glen Vandevenne was greatly appreciated. His careful guidance and friendly conversations further made sure I never felt alone in dealing with any kind of situation.

Following this, I wish to express my gratitude to Koen Gillissen and Stijn Duchateau for immediately helping me understand the problem I was confronted with and encouraging me to instantly put theories to the test. Furthermore, I would like to offer my special thanks to Jan Mertens and Lieven De Winter. Having them around at the electronics lab of IMO gave me peace of mind, not in the least after they helped me save a critical component. My colleague Yannick Wellens should also not be forgotten. We mutually spent a lot of time at IMO, took time to listen to each other's problems and generally had a lot of laughs.

Finally I would like say that I owe a lot of gratitude to my parents. They provided me with the right conditions and ethics to get me where I am now. My brother furthermore makes sure I keep my feet on the ground and keep my grip. A very special thanks also go out to my girlfriend for keeping my motivation high and my mind at rest.

Abstract (Nederlands)

Flash photography vision system for inkjet drop formation characterization

Auteur: Steven Nagels

Interne promotor: Prof. dr. ir. Jan Genoe

Externe promotor: Prof. dr. ir. Wim Deferme

Op het Instituut voor Materiaalonderzoek (IMO) van de UHasselt ontwikkelt men functionele inktten voor het inkjet printen van bijvoorbeeld RFID antennes. Printen binnen zeer kleine toleranties eist echter kennis van het exact materiaalgedrag tijdens elk van volgende afzettingsfasen: het uitstoten van de inkt, haar val naar het substraat en haar interactie met het oppervlak. In deze masterproef wordt een systeem ontwikkeld om inkjet druppels over de volledige afstand van printkop tot substraat optisch te inspecteren.

Om de vallende druppels zeer scherp in beeld te brengen, wordt gekozen voor *flash photography*. Hierbij is niet de mechanische sluitertijd van de camera maar de duur van de gepulste belichting bepalend voor de effectieve belichtingstijd van de druppel. Verder levert het gebruik van *bi-telecentrische lenzen* meer accurate beelden op door randeffecten en vervorming te beperken. Een *tijdkritische hardware schakeling* garandeert vervolgens betrouwbaar getimede vastlegging van beelden voor verdere verwerking in *LabView*.

Het resultaat bestaat uit twee delen. Enerzijds werd een zorgvuldig samengesteld visiesysteem opgebouwd dat, met gekarakteriseerde nauwkeurigheid, geschikt is om de druppels te observeren. Anderzijds zijn metingen uitgevoerd op de resulterende camerabeelden bij één vaste instelling van de printkop. Hieruit werden een straal van ongeveer $24\mu\text{m}$, snelheid van gemiddeld 1.08m/s en volume van naar schatting 62 picoliter afgeleid als eigenschappen van de hoofddruppel.

Abstract

Flash photography vision system for inkjet drop formation characterization

Author: Steven Nagels

Internal promoter: Prof. dr. ir. Jan Genoe

External promoter: Prof. dr. ir. Wim Deferme

On the Institute for Materials Research of Hasselt University, efforts are being made to develop functional inks for the ink jet printing of applications such as RFID antennas. Printing within very strict boundaries however requires knowledge of the exact material behavior during each of the following deposition stages: ejection of ink, its fall to the substrate and its surface interactions. During this Master's thesis, a system will be developed to inspect ink jet droplets along their entire path from printhead to substrate.

To image falling droplets very precisely, *flash photography* was designated as the method of choice. Not the mechanical shutter speed of the camera, but instead the effective lighting time of the strobed light source is thereby decisive for the effective exposure time of the droplet. The usage of *bi-telecentric lenses* furthermore ensures sharper and more accurate images by reducing side-effects and aberrations. A *time critical hardware circuit* moreover guarantees reliably timed capturing of images for further processing in *LabView*.

The result of this thesis is twofold. On one hand a carefully composed vision system is made which is able to observe droplets and of which the accuracy is determined. On the other hand, measurements have been taken from resulting camera images for one fixed printhead configuration. Properties of the main drop were then ultimately deduced from these measurements and found to include a $24\mu\text{m}$ radius, 1.08m/s average speed and 62 picolitres estimated volume.

Table of Contents

Acknowledgements	I
Abstract (Nederlands)	II
Abstract	III
Table of Contents.....	IV
List of figures.....	VII
List of graphs.....	IX
List of tables	X
List of formulas	XI
List of abbreviations and symbols	XII
1. Introduction.....	1
2. Literature study	3
2.1 Functional inkjet printing	3
2.1.1 Inkjet printing principles.....	3
2.1.2 Commercial functional inkjet systems.....	5
2.1.3 Custom built testing setups	6
2.1.4 Decisive inkjet printing process parameters for vision	8
2.2 Drop formation and influencing parameters.....	9
2.2.1 Drop formation stages/physics	9
2.2.2 Influencing parameters and side effects.....	11
2.3 Machine Vision	18
2.3.1 Fundamental parameters	18
2.3.2 Lens	18
2.3.3 Lighting.....	19

2.3.4	Camera	21
3.	Materials and methods	25
3.1	Ink jetting, imaging and triggering methods	25
3.1.1	Ink jetting.....	25
3.1.2	Image acquisition.....	25
3.1.3	Precise timing between components	28
3.2	Component choice	30
3.2.1	Ink jetting components.....	30
3.2.2	Machine vision components.....	31
3.2.3	Mechanical support	35
3.3	Implementation of the trigger system	38
3.3.1	Component I/O specifications	38
3.3.2	Variations in triggering.....	39
3.4	System operation verification	41
3.4.1	Strobe light output	41
3.4.2	Individual component input-output delay.....	42
4.	Measurements and results	45
4.1	Delay measurements.....	45
4.1.1	Jet Drive III ink jet drive electronics	45
4.1.2	Manta G-125B camera	46
4.1.3	PP880 strobe controller	47
4.2	Drop visualization	48
4.2.1	Telecentric backlight	50
4.2.2	Generic power led	52
4.3	Drop characterization.....	56

5. Discussion and conclusion.....	63
6. Literature.....	65
Appendix A: JetDrive delay measurements data.....	69
Appendix B: Manta delay measurements data	69
Appendix C: PP880 delay measurements data	70
Appendix D: Drop characterization data	70

List of figures

Figure 2-1: Schematic diagram of a continuous inkjet printer [2].....	3
Figure 2-2: Electrostatic ink jetting nozzle with Taylor cone [2].....	4
Figure 2-3: Schematic diagram of a drop-on-demand printhead [2]	4
Figure 2-4: Flash photography setup used by Hongming Dong et al. [17].....	6
Figure 2-5: Flash photography setup at Cambridge University [18].....	7
Figure 2-6: Ultra high speed camera setup at Cambridge University [19]	8
Figure 2-7: Piezo deformation as driving principle for DoD printhead [25]	10
Figure 2-8: Higher pressure waves from constructive interference [25]	11
Figure 2-9: Mist droplet satellites (marked with squares) [25].....	12
Figure 2-10: Long tail break-up into satellites [25].....	13
Figure 2-11: Fast satellite in front of the main droplet [25].....	13
Figure 2-12: Slow trailing drop break off from main drop (slow satellite formation) [25]	13
Figure 2-13: Nozzle plate wetting from overfilling [25].....	14
Figure 2-14: Air entrapment from flooded nozzle dynamics [25].....	14
Figure 2-15: Pre-actuation followed by the main droplet at 30 μ s [25]	16
Figure 2-16: First drop dissimilarity [27].....	16
Figure 2-17: General form and parameters of a bipolar waveform [13]	17
Figure 2-18: Comparison of entocentric (left) and telecentric (right) lenses [29].....	19
Figure 2-19: Comparison of typical light sources [33]	20
Figure 2-20: back, diffuse, directional and dark field lighting, left to right [32].....	21
Figure 2-21: Full frame CCD, frame transfer and interline transfer [33]	23
Figure 2-22: CCD to CMOS integration comparison [33].....	24
Figure 3-1: Schematic overview of high speed camera observations.....	26
Figure 3-2: Schematic overview of continuous mode camera imaging w/ strobe synced to nozzle.....	27
Figure 3-3: Schematic overview of triggered mode camera imaging	28
Figure 3-4: RT OS as an extra layer between OS and hardware [34]	29
Figure 3-5: MicroFab PH-47 printhead [35]	30
Figure 3-6: JetDrive III nozzle drive electronics [36].....	31
Figure 3-7: Manta G-125B spectral sensitivity [37].....	32
Figure 3-8: Manta camera technical drawing [38].....	32
Figure 3-9: TC4M-004C technical drawing [39]	33
Figure 3-10: X42182 relative spectral power distribution (only green is relevant) [41].....	34
Figure 3-11: Generic power led with attached PP880 drive module.....	34
Figure 3-12: Cree XM-L U2 spectral output depicted in blue [42].....	35

Figure 3-13: CAD design of mechanical base	36
Figure 3-14: Complete system overview	37
Figure 3-15: Input (left) and output (right) schematic for Manta camera.....	38
Figure 3-16: Placement of the PV cell in front of light source - PV cell detail in inlay	42
Figure 3-17: Delay measurements wiring	43
Figure 4-1: Composite overview of the nozzle from the camera's perspective	48
Figure 4-2: Exposed nichrome wire coil and normal wirewound resistor as reference.....	49
Figure 4-3: JetDrive III bipolar waveform parameters [44].....	53
Figure 4-4: Original image as obtained with the developed vision system and generic power led.....	54
Figure 4-5: Imaged drop formation at 30 μ s, 60 μ s, 90 μ s and 125 μ s	54
Figure 4-6: Imaged drop formation at 155 μ s, 180 μ s, 210 μ s and 255 μ s	55
Figure 4-7: Imaged drop formation at 275 μ s, 300 μ s, 325 μ s and 370 μ s	55
Figure 4-8: Imaged drop formation at 295 μ s, 430 μ s, 450 μ s and 485 μ s	55
Figure 4-9: Imaged drop formation at 180 μ s.....	56

List of graphs

Graph 3-1: Triggering configuration 1 - all at once	39
Graph 3-2: Triggering configuration 2 - strobe synced to camera	40
Graph 3-3: Triggering configuration 3 - domino effect	40
Graph 4-1: Scope image of delay between trigger input and waveform output	45
Graph 4-2: Scope image of delay between trigger input and 'exposure' signal output	46
Graph 4-3: Scope image of delay between trigger input and light source drive pulse output	47
Graph 4-4: Scope image of optical response (CH2) on long >1s driving pulse.....	50
Graph 4-5: Scope image of optical response (CH2) on short 5 μ s driving pulse	51
Graph 4-6: Scope image of optical response (CH2) measured above lamp	52
Graph 4-7: Scope images of optical response on 28V (left) and 32V (right) pulse amplitudes.....	52
Graph 4-8: Scope images of optical response on 34V (left) and 36V (right) pulse amplitudes.....	53
Graph 4-9: Satellite drop radius as a function of distance	57
Graph 4-10: Satellite drop volume as a function of distance	57
Graph 4-11: Satellite drop speed as a function of distance.....	58
Graph 4-12: Main drop radius as a function of distance	59
Graph 4-13: Main drop volume as a function of distance	59
Graph 4-14: Main drop speed as a function of distance	60

List of tables

Table 2-1: Ranges of drop speed and diameter found in literature.....	9
Table 4-1: Statistic results of JetDrive III delay measurements.....	46
Table 4-2: Statistic results of Manta G-125B delay measurements	47
Table 4-3: Statistic results of PP880 delay measurements.....	48

List of formulas

Formula 2-1: Ohnesorge number [2].....	11
Formula 2-2: Minimum sensor resolution [29]	18
Formula 2-3: Focal length [29].....	18
Formula 2-4: Magnification for telecentric lenses [29]	19

List of abbreviations and symbols

IMO	Institute for Materials Research
RFID	Radio-frequent identification
IMOMECE	Institute for Materials Research in MicroElectronics
OLED	Organic Light Emitting Diode
OPV	Organic Photo-Voltaic (cell)
DoD	Drop-on-Demand
TTL	Typical Transistor Logic
CCD	Charge Coupled Device
SiP	System-in-Package
Oh	Ohnesorge number (symbol)
μ	Viscosity
ρ	Density
σ	Surface tension
L	Characteristic length scale of nozzle
FOV	Field Of View
LED	Light Emitting Diode
IR	Infrared
ASP	Analog Signal Proessing
DSP	Digital Signal Processing
ADC	Analog-to-Digital Conversion
USB	Universal Serial Bus
CMOS	Complementary Metal-Oxide-Semiconductor
FPS	Frames per second
RGB	Red Green Blue
DAQ	Data Acquisition
RT	Real-Time
I/O	Input/Output
GPIO	General Purpose Input-Output
CAD	Computer Aided Design
FET	Field Effect Transistor
BNC	Bayonet Neill–Concelman (connector)
IQR	Interquartile Range
SNR	Singal-to-Noise Ratio

RF

Radiofrequent

PV

Photovoltaic (cell)

Ω

Unit of resistance (ohm)

1. Introduction

The Institute for Materials Research (IMO) is a research institution of Hasselt University. The main focus of IMO lies in developing and characterizing new material systems through fundamental as well as applied research for use in microelectronics, bioelectronics and nanotechnology. It is closely linked to the world-leading research centre in nano-electronics, the Interuniversity Microelectronics Centre (IMEC) of Leuven and contains a local IMEC division called IMOMECEC which performs the majority of applied research programs in collaboration with industrial partners.

As a research domain of IMO, functional printing holds the promise of, among others, foldable light emitting or absorbing devices (OLED/OPV) and intelligent clothing. In the pursuit of this final outcome, the functional printing group uses semiconducting, conducting and dielectric inks whose rheology and surface energy are studied to determine the ink's printability. Besides this, possible deposition techniques such as film casting, inkjet printing, spray coating and screen printing are being looked into as low-cost production methods for future electronic devices. An interesting asset of functional printing is also the wide range of substrates that could be used to print on. Luminescent wallpapers and flexible electronics are already within reach of this technology.

At IMO and in collaboration with the functional printing group, researchers from the chemistry department are developing new functional inks which exhibit certain properties (e.g. conductivity) and therefore are useful in studying the feasibility of producing electronics by various printing methods. Being one of these methods, Drop-on-Demand inkjet printing also is the most versatile and easily applicable way to go. With this technology, which is the same principle as used in everyday consumer inkjet printers, it is possible to deposit picolitre volumes of material solutions with high precision in a non-contact manner and go from design to production with little or no start-up overhead.

An essential factor in order to achieve this high grade of precision, is knowledge about the ink's behavior when fired from the printhead nozzle. Under certain circumstances, the ink will form a tail trailing the main droplet core of which smaller secondary drops or 'satellites' can break loose [1]. These tails can only be tolerated if they recombine with the main droplet before impact. If not, or in the worst case when satellites are formed, it is not possible to predict how and where they will fall on the substrate. This uncertainty is definitely problematic when printing electronics because it could cause short-circuit between neighboring tracks. A strategy has to be developed whereby clever tuning of the waveform parameters leads to emission of droplets with an optimal round shape.

The first challenge of this master's thesis is therefore to develop a vision system for drop formation inspection of newly developed functional inks being fired from a DoD inkjet printhead. Using this vision system as a tool, it should be possible to measure the average speed, shape and volume of all droplets fired from a certain printhead using the same driving waveform.

A second challenge would be to obtain a vast understanding of the influence that both ink characteristics, such as density, viscosity and surface tension, and driving waveform parameters, such as rising time, sustain time, falling time and peak voltage, will have on the drop formation process. The purpose of this gathered knowledge would be as a solid foundation for the development of an optimization strategy to match ink and printhead in an effort to obtain maximum print quality and thus circuit integrity in the case of printed electronics.

The final possible challenge in the limited time span of this thesis could then lie in combining this strategy, which is based on well-known and thoroughly tested inks, with the aforementioned vision system to determine the printability of a series of untested inks or the possible necessary modifications in order to make them printable.

The structure of the hereby presented dissertation is divided into five main chapters. This very introduction is the first one of these chapters. Hereafter, the second chapter will entail all established knowledge which is important in the context of this thesis in the form of a literature study. Its purpose is to deliver to the reader a rich background about ink jet printing, drop formation and machine vision up to the current state of the art. Next, in chapter three, the general approach which was selected for this thesis is revealed. Not only the selected methods and their corresponding components are explained therein, but also the manner in which these components will work together and have their intended operation verified. This in turn serves as foreknowledge to chapter four, in which the measurements and results are presented. Chapter four is to presenting the outcome of experiments performed on the intrinsic delay between components, visualization of droplets and processing of the droplet images. The results are also briefly discussed. Chapter five then contains the extensive overview of these results along with the drawing of a few conclusions from the delivered efforts. A global conclusion for the thesis is ultimately formed at the end of this final chapter.

2. Literature study

2.1 Functional inkjet printing

2.1.1 Inkjet printing principles

Inkjet printing is a widespread technique traditionally used for transferring digital combinations of images and text onto a paper carrier. It is a time-saving method as patterning is performed simultaneously with material deposition. Also, due to its non-contact nature, mechanical damage along with cross-contaminations is avoided. At the core, every inkjet printer consists of a printhead, driving electronics and an ink reservoir. To be able to use inkjet printing successfully for material printing, it is important to understand the different types of inkjet printing and to identify which one is most suitable for material printing. The three main variants of inkjet printing are: continuous, electrostatic and drop-on-demand (DoD) [2].

Continuous inkjet printing

In this inkjet technology, a continuous and evenly spaced stream of drops is formed. In a first step, a continuous jet of ink is ejected from the printhead by means of pressure. This jet is then broken into droplets by applying a regular disturbance to it. To achieve imaging, only certain droplets from the stream are selected. This can be achieved for example by means of electrostatic charging at the nozzle and deflection by a fixed electric field. All ink that doesn't reach the substrate is reused.

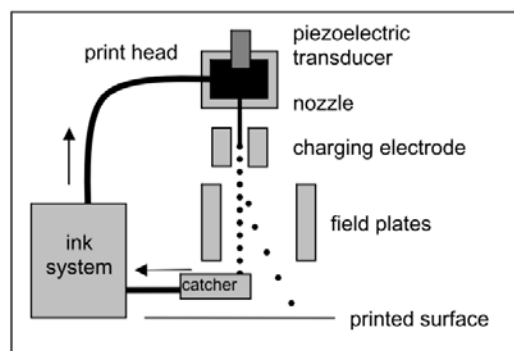


Figure 2-1: Schematic diagram of a continuous inkjet printer [2]

Electrostatic inkjet printing

The electrostatic technique utilizes a potential difference across the liquid in the nozzle and a nearby plate, located on the other side of the substrate. When this potential difference is high enough, the ink will form a conical surface called a Taylor cone which emits droplets [3]. The main advantage of this ink jetting technique can be found in the fact that the emitted droplets can be of a diameter much smaller than the nozzle diameter. It only works with conductive inks though, which in turn is a major disadvantage.

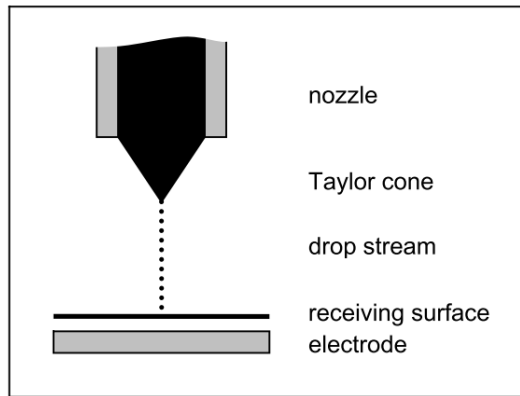


Figure 2-2: Electrostatic ink jetting nozzle with Taylor cone [2]

Drop-on-demand inkjet printing

Drop-on-demand technology only emits droplets when required. A droplet is ejected by rapidly changing between positive and negative pressure. The positive pressure will squeeze out a small amount of ink which will stay linked to the ink in the reservoir. Only by sudden negative pressure the link will be broken at the small nozzle aperture, making the droplet break away from the printhead. DoD systems can be further divided into two categories based on the actuation principle: 1) Bubblejet systems momentarily heat up the ink to produce an unstable gas bubble and positive pressure pushing away the ink. The negative pressure then originates from the collapsing bubble which leaves vacant space, sucking the ink back in. 2) Piezo based DoD printheads use piezoelectric plates which can be changed between exerting positive pressure or negative pressure by reversing their polarity.

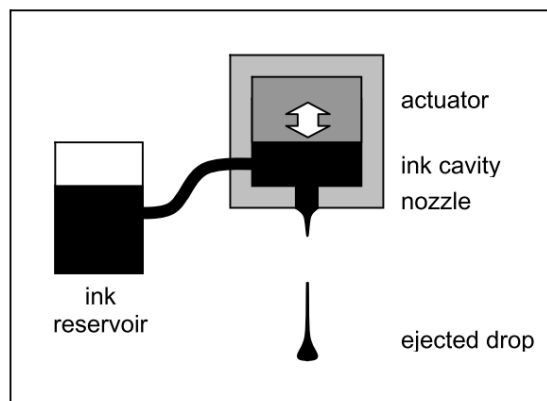


Figure 2-3: Schematic diagram of a drop-on-demand printhead [2]

The most common issue with DoD printing is clogging when solvent has evaporated at the nozzle during standstill. The presence of dried ink particles causes irregularities during the printing of the first few drops, also known as the ‘first drop problem’ [1], [4]. These anomalies will however fade away as more dried ink is removed by each consequent ejected drop.

2.1.2 Commercial functional inkjet systems

Before we start configuring our own inkjet testing platform, it certainly is useful to see what kinds of different solutions already are being used.

Commercial print test solutions

It is currently possible to acquire a complete functional printing solution from large vendors within the industry. The focus of these systems however lies more in studying the printing process and resulting patterns than observing droplets and characterizing inks. Three of these systems were looked into.

The New Mexico based Optomec has a range of AerosolJet printers that doesn't use the popular DoD printhead technology but instead atomizes a liquid sample, creating droplets of 1-5 μm , and then deposits the aerosol using inert carrier gas and sheath gas. Their most complex R&D device is the AerosolJet 300. Minimum feature sizes of 10 μm can be obtained.[5]

Roth & Rau from Germany is the company behind the Pixdro series of functional inkjet printers. Their Pixdro LP50 system has an overall system accuracy of 5 μm , integrated drop and print view and optional laser head assembly. Feature sizes down to 5 μm are possible. It is also compatible with a range of industrial print heads. [6]

The Dimatix Materials Printer DMP 2831 is a benchtop R&D system from FujiFilm USA which utilizes a disposable piezo inkjet cartridge which can be filled with custom testing fluids. It combines a drop-watch camera with a waveform editor to allow drop characteristic optimization and can thus be used to study the effects of changing waveform parameters on drop formation. Features as small as 20 μm can be deposited. [7] It turns out to be an excellent tool to screen materials, but the large drop-to-drop variations limits the application of this tool for demo and production.

Integrated ink testing setups

Complete functional ink jetting solutions which are more focused on inspecting ink behavior are also commercially available. Effective printing possibilities are left out as the purpose of these solutions is to be used in more experimental instead of production environments. The German company Microfab Technologies created a whole range of Jetlab tabletop printing systems intended for microdispensing investigations. Their latest Jetlab 4 is compatible with any of the Microfab print heads, contains a drop watcher (mounted off centre at -15°) with synchronized strobe and a fiducial camera. [8]

Testing components

Components for experimental setups can furthermore be obtained separately to be built into a customized system. They are usually reserved for instances which are interested in more fundamental research.

Microdrop Technologies from Germany sells such components for building your own testing system. Their MD-E-3000 driving electronics can control any one of the Microdrop dispenser heads which nozzle diameter lies between 30 and 100 μm and viscosity range goes from 0.4 up to 100mPas. Droplet size ranges from 15 to 120 μm and travel velocity peaks at 2.5 m/s while emission rates cannot exceed 6 kHz. The unit is configured through a touch panel interface and can be triggered by a TTL input. [9]

Microfab also offers separate electronics and printhead assemblies. Their JetDrive III driving electronics is computer controlled through RS232, can create 8 point trapezoidal waveforms, has a built in strobe delay, input for external trigger and available LabView sample program. It is compatible with all Microfab printheads and has a droplet emission frequency of up to 30 kHz. [10]

Other mentionable companies which provide inkjet drop formation testing components are: Fujifilm, Trident, Konica, Seiko and Xaar. They all provide printing heads with more than one nozzle, which are unnecessary for our drop watching application and will not be discussed further.

2.1.3 Custom built testing setups

As commercial solutions often lack versatility in terms of adjusting the setup and using printheads from different brands, the need is felt to further inspect the possibilities of custom built setups. Many research groups in inkjet printing use systems or components either from MicroFab [11]–[13] or Microdrop [14]–[16]. Three interesting setups have been selected of which the operation and specifications are summarized below.

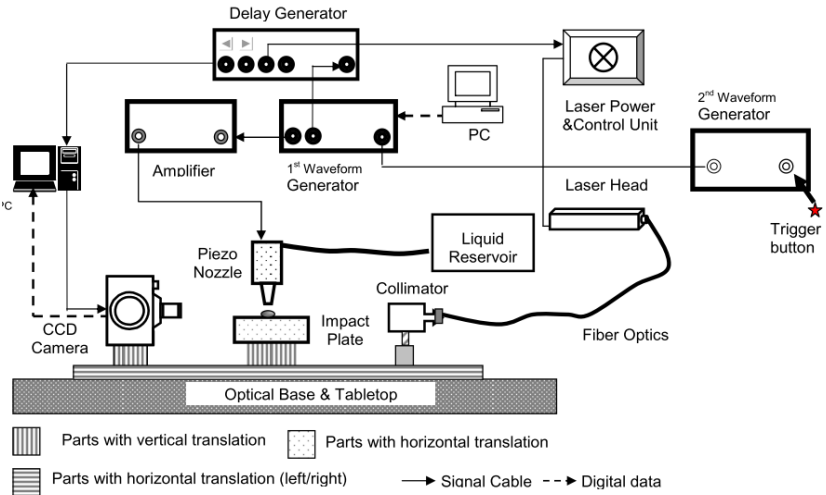


Figure 2-4: Flash photography setup used by Hongming Dong et al. [17]

A first extensively documented inkjet drop watching system can be found in a dissertation of H. Dong at the Georgia Institute of Technology [17]. Its vision system consists of a 640x480 pixels, low speed

CCD camera combined with a 200 ns laser flash for flash photography ‘freezing’ of the droplet’s motion in an image with spatial resolution of $0.81 \mu\text{m}/\text{pixel}$. The technique used makes sure to capture an image of each drop formation event by synchronizing camera shutter (max 30 fps) and flash with the droplet emission frequency of the printhead. To achieve this time-critical behavior, dedicated signal generators are used to trigger the individual image acquisition components. First a trigger is sent to the waveform generator which then simultaneously emits a driving pulse for the printhead and a TTL signal to a delay generator. This delay generator in turn triggers the CCD camera and sends a burst of TTL signals to the laser illumination. By adjusting the delay time at the delay generator between the incoming TTL signal from the waveform generator and the triggers for camera and illumination, different stages of the drop formation process can be examined. The dissertation also explains how to calculate the required intensity of illumination from the full well capacity and quantum efficiency of the used CCD. Its print head is from Trident.

Furthermore, at the University of Cambridge, a study about impaction and spreading of small droplets [18] made use of a comparable flash photography system. It consisted of a high resolution 1290×960 pixels Prosilica GC1290 CCD camera, 12x Navitar zoom lens and 20ns duration flash.

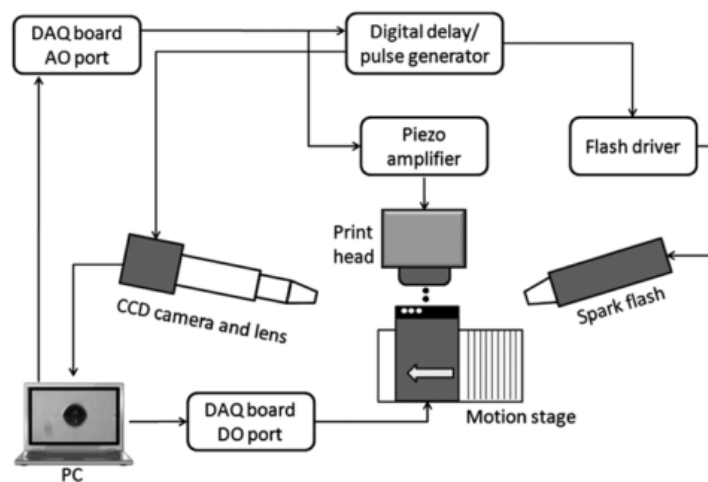


Figure 2-5: Flash photography setup at Cambridge University [18]

Lastly, a system based on a Shimadzu HPV-1 ultra high speed camera was also used at the University of Cambridge. Its function was to analyze meniscus oscillations and nozzle plate flooding [19]. Droplets were emitted using a Xaar CJ126/200 DoD print head and Xaar XUSB controller. Both the used microscope lens (Navitar 12X ultra zoom) and the light flash source (Adapt Electronics Photoflash CU-500) were placed under an angle to the nozzles to maximize the camera illumination. The utilized exposure time could be configured down to $0.25 \mu\text{s}$ at 1 million fps and a resolution of 310×260 pixels. Consequently, a very high temporal and spatial resolution is achieved. This system uses fast shutter time instead of light flashes to capture droplets in motion with minimum blurring.

The only reason for using a pulsed light source in this case is due to the higher possible light output in comparison to continuous light.

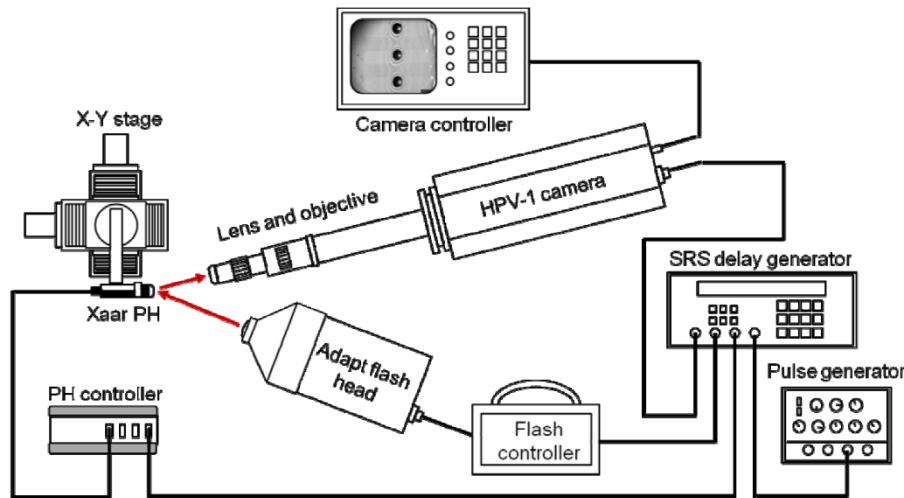


Figure 2-6: Ultra high speed camera setup at Cambridge University [19]

2.1.4 Decisive inkjet printing process parameters for vision

To be able to later on design an appropriate vision system, knowledge also needs to be gathered about the dynamics of the object under inspection (i.e. the droplet). As a safety measure, the system should be built to cope with the highest drop speeds and lowest drop diameters possible. Values for these extremes are obtained by comparing different reports in literature.

A research team from the University of Manchester reported typical drop sizes from 5 to 50 μm and velocities between 1 and 10 m/s after looking into ceramic inks [20]. Another study involving ceramic inks [21] specified remarkably lower values for their tested inks' drop sizes and velocities. These vary respectively between 15 to 20 μm and roughly 4 to 8 m/s. Moreover, a pharmaceutical study on printed medicine [22] mentions drop sizes from 10 up to 50 μm for their caffeine based ink. Measuring droplets of the same order of magnitude, 40 μm , a study about inkjet printed electrical interconnections in system-in-package (SiPs)[23] claims a rather high 10.95 m/s firing velocity for tested dielectric inks and 4.55 m/s for conductive inks. Similar to the aforementioned conductive inks, were the droplet speeds of 2 to 4 m/s measured in a Jetlab setup for experiments on substrate drop coalescence [12]. Their notes on drop size exceeded the much found range of 20 to 50 μm with measurements of up to 60 microns. Furthermore in a specific study on inkjet drop formation and deposition [17], normal drop sizes of 40 to 50 μm are noted. Tested impact velocities varied between 2 and 12 m/s with a nozzle to substrate distance of 2 mm, much higher than the 0.8 mm used in a research group for satellite-free inkjets with PEDOT:PSS [11] which utilized exceptionally high droplet speeds ranging from 12 to 15 m/s.

Table 2-1: Ranges of drop speed and diameter found in literature

drop speed		
lower limit	upper limit	unit
1	15	m/s
drop diameter		
lower limit	upper limit	unit
5	60	μm

According to literature, the vision system to be built should support extreme drop speeds of up to 15m/s and drop diameters as low as 5 μm . This can be observed in the above table.

2.2 Drop formation and influencing parameters

2.2.1 Drop formation stages/physics

The physics behind drop formation are found to comprise a range of domains including, but not limited to, materials science, acoustics and hydrodynamics. The process begins by applying a drive signal to a piezoelectric crystal in the printhead nozzle, causing it to deform. These deformations procreate acoustic waves which by themselves not only take part in reflection, absorption and interference, but also agitate the ink fluid column in the nozzle. By purposefully designing the drive signal, precisely aimed agitations can be generated to ultimately attain steady drop formation.

The underlying theories for today's understanding of drop formation reach back as far as the mid 19th century. The first studies on liquid column decay, the relationship of jet diameter to drop size and flow dynamics were first performed by Plateau and Lord Rayleigh, elaborating on earlier measurements by Savart. Their contributions resulted in the Plateau-Rayleigh instability theorem, stating that a stream of water with a wavelength greater than its circumference will break up into individual droplets [24]. When combined with the understanding of Young and Laplace that "the same force, which holds liquid together, is also the driving force behind the break-up of a liquid jet" [25], every foundation for controlled drop formation was in place. After eventually the first (continuous) inkjet device was developed in 1960 at Stanford University, and a decade later also the DoD piezo inkjet, further research looked into the exact behavior of a typical inkjet printhead during operation in order to optimize the drop formation process. Prerequisites were that it should be possible to perform 'drop size modulation' i.e. change the volume of emitted droplets. Furthermore, the speed and volume of emitted droplets should be consistent through time in order to attain even distribution of ink in the printed pattern. Also while keeping printed pattern quality in mind, it is important to avoid tails, satellite drops and air bubbles. Lastly, the obtaining of a straight jet is favored as it contributes to a shorter time of flight and less vulnerability to disturbances.

Inside the printhead, the first step to drop formation occurs at the piezoelectric element which changes shape under the charging by a driving waveform. It should be noted that in order to reduce oscillations, this waveform can be low-pass filtered. [26] Cross talk between the nozzles is found in all printheads with multiple nozzles and moreover can alter jetting circumstances locally. It can easily be detected from how non actuated channels deform along with an actuated channel. This can either be because the channels are neighboring each other or because the acoustic wave is not completely reflected at the supply and oscillations are passed through the connection to the reservoir. The first one is called ‘local crosstalk’, the latter one ‘acoustic crosstalk’. The charging of the piezo element expands the ink channel and generates a negative acoustic pressure wave.

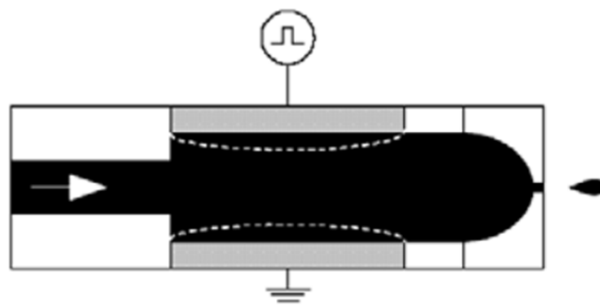


Figure 2-7: Piezo deformation as driving principle for DoD printhead [25]

By studying acoustic impedances, it is found that this wave is reflected at the reservoir side as a positive inversion of itself. De-charging of the piezo element makes the channel return to its former shape and causes a positive pressure wave. When the time between charging and discharging is chosen carefully, the reflected and inverted pressure wave of the charging operation is constructively interfered with by the positive wave of the discharging operation. The resulting higher pressure wave makes for a higher acceleration of the ink and results in drop formation. The manual configuration of a driving waveform is usually based on this principle. Its pulse width is best chosen to correspond to the first eigenfrequency of the ink channel as described above. This first eigenfrequency usually has a value of a few tens of kHz. [25] When a printhead has multiple nozzles, resonances can appear in the printhead structure if many of them are excited simultaneously.

Empirical formulas have been defined for the relationship between nozzle area, nozzle shape, waveform width, drop speed, viscosity, surface tension, channel length, drop size, inlet geometry and the effective speed of sound inside the nozzle. An alternative approach is to consider the ink coming out of the nozzle to be moving at the same speed as the ink inside the nozzle and conclude that a drop will be formed when “the kinetic energy of the ink outside the nozzle becomes equal to the integral

over time of the kinetic energy at the nozzle exit, minus the surface energy of the ink outside the nozzle” [25].

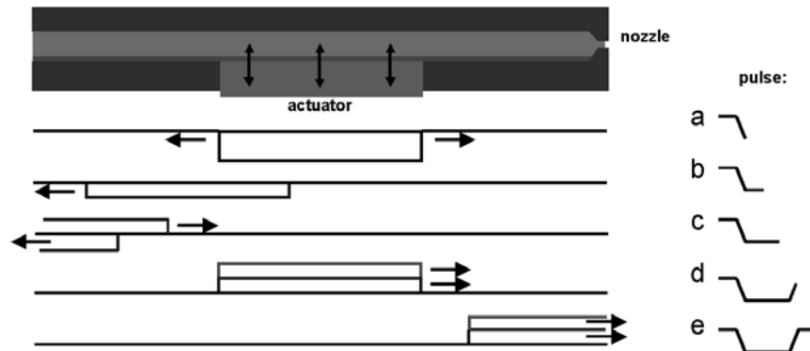


Figure 2-8: Higher pressure waves from constructive interference [25]

Yet another approach is to simulate the ink’s behavior with specialized software like Flow3D. Following from these theoretical models are a few rules of thumb. For instance every m/s change in drop speed is said to correspond to about a 10% adaption of the driving voltage. Elsewhere the actuator displacement is stated to be twice as large as the amount of ejected ink.

2.2.2 Influencing parameters and side effects

The inkjet printhead operation will now be further investigated in detail. First the influence of ink properties is observed along with the related elements in drop formation. After viewing everything from the nozzle’s point of view, a transition is made to the droplet. Right before tail break off, and consequently drop formation, the drop will be connected to the nozzle through a long tail. At first, the ink is ejected at high speeds of up to 20 m/s which is the same speed as the meniscus. As more ink is ejected however, the head of the drop will be slowed down by its connecting tail to the final drop speeds which can be determined by optical inspection. Let it be noted that higher drop speeds result in a shorter time of flight and consequently a smaller sensitivity to disturbances. They can therefore be said to be more desirable. The ink properties viscosity and surface tension have a decisive contribution in the decelerating effect of the tail. In fact, surface tension can be seen as the driving force behind break off. Likewise, inertia should also be kept into consideration, which brings us to the Ohnesorge number.

$$Oh = \frac{\mu}{\sqrt{\rho \sigma L}}$$

Formula 2-1: Ohnesorge number [2]

This dimensionless number is used to reflect how the viscosity (μ), surface tension (σ) and inertia ($\rho \cdot L$) are proportioned relative to each other in an ink and can be used as a measure of printability

regarding a certain nozzle. A higher Ohnesorge rating corresponds with a greater influence of the viscosity and lower expectations towards good printability. The transition from a long ejected trail to a free droplet takes place at the nozzle meniscus, being the point with the largest pressure variance transition. Higher viscosity or lower surface tension are accompanied by longer tails. A proven method to alter an ink's viscosity is by controlled heating of the nozzle. [14]

Aside from ink properties, the circumstances wherein jetting takes place are very much decisive for the eventual drop formation. A remarkable finding in the tail behavior is that after breaking free from the nozzle, it moves away with a high speed towards the main drop. This is due to the very high capillary pressure which exists at the – initially - very small tip of the tail right after it breaks free. As the tail gets closer to the main droplet, it is less stretched meaning its tip will also grow in size. Along with it, the capillary pressure drops and the tip slows down until it eventually reaches a constant speed. Most peculiar is the fact that this tail behavior is completely independent of the main droplet. Hence if the main drop speed exceeds the steady state speed of the tail, the two will never combine. This can be observed at higher waveform amplitudes. Formation of other structures furthermore can be found which are even less desirable than tails and each originate from different aspects of the jetting circumstances. A first type is the formation of secondary drops called ‘satellites’. A distinction into four classes can be made: mist droplets from the secondary tail, long tail satellite drops, fast satellites and slow satellites. First of all, ‘mist droplets’ are extremely small droplets of less than 1pl. They originate from the secondary tail, which is a very fine tail formed between the main long tail and the nozzle at pinch-off. These drops are too small to be seen with the naked eye but are still a detrimental uncertainty in functional printing.

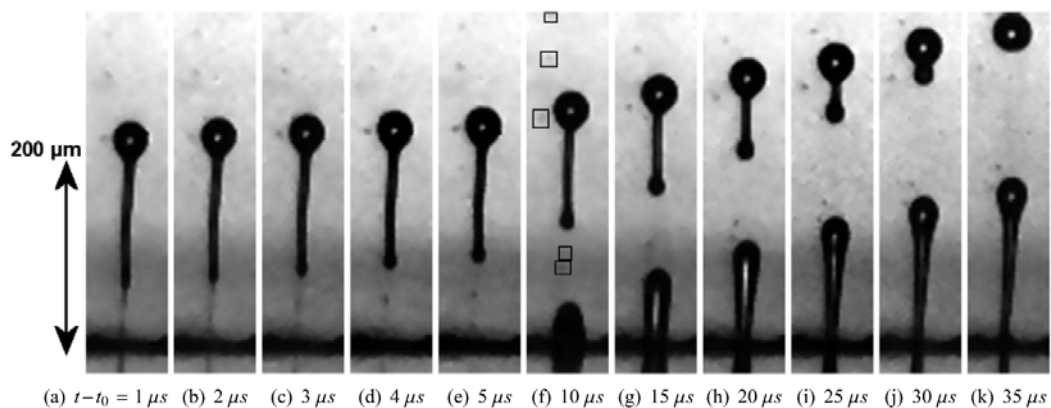


Figure 2-9: Mist droplet satellites (marked with squares) [25]

Secondly, when the main droplet speed exceeds the steady state speed of the main tail, the tail will be stretched. Due to the Rayleigh instability principle and, triggered by noise, this stretching will

inadvertently lead to a break-up of the tail into droplets. These are called ‘long tail satellites’. The total surface energy of all droplets together will be lower than that of the tail.

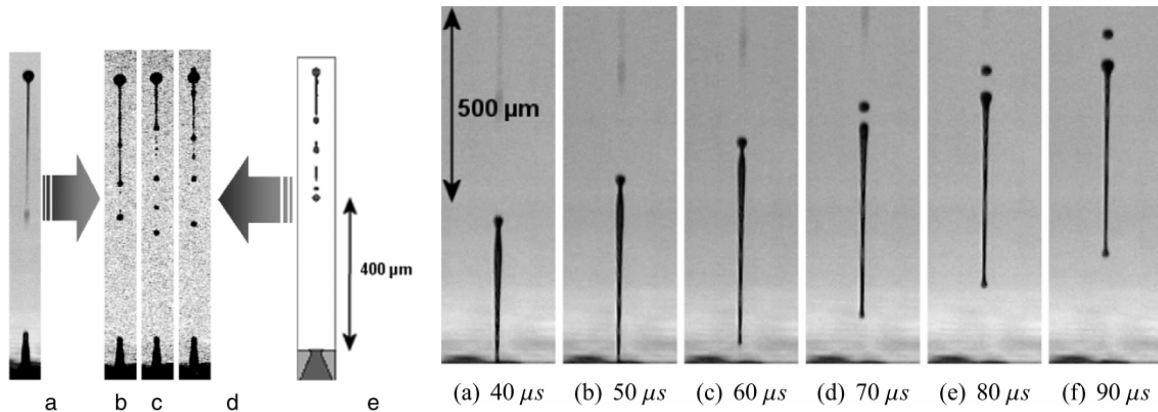


Figure 2-10: Long tail break-up into satellites [25]

Figure 2-11: Fast satellite in front of the main droplet [25]

A third category to be observed are ‘fast satellites’ and only occur at high drop speeds. Fast satellites originate as part of the drop moves at a higher speed in front of the rest, effectively breaking loose and becoming a separate leading drop. The ink is already accelerated too much while coming out of the nozzle, causing it to overcome the surface tension and break away from the rest. One way the initial acceleration can be controlled, is by the rise time of the driving waveform. Faster rise times result in higher pressure peaks and higher acceleration (and vice versa).

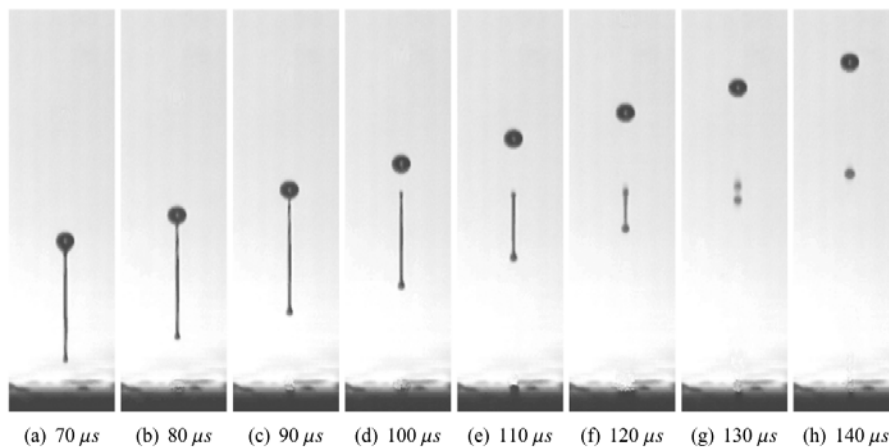


Figure 2-12: Slow trailing drop break off from main drop (slow satellite formation) [25]

‘Slow satellites’ are seen as a final category. These satellites arise from a break off of the main tail into a slower droplet which trails the main droplet. The break-off is stimulated by the presence of a minimum in tail width which in turn is a result of having two positive pressure peaks during drop formation. One way to get these two positive pressure peaks is by having a waveform with a large pulse

width. The negative charging pulse will already be reflected and have reached the nozzle as a positive pulse before the positive discharging pulse arrives.

Another important phenomenon is the refilling of the nozzle and the nozzle plate wetting it can result into. Refilling takes place due to the residual vibrations in the channel after drop ejection. Over the period of a few oscillations the nozzle meniscus is effectively displaced outwards, causing the nozzle to refill. Overfilling of the nozzle is a phenomenon which can also be observed when the driving waveform and thus its resulting residual vibrations are fairly strong, causing the meniscus to be displaced even more outward.

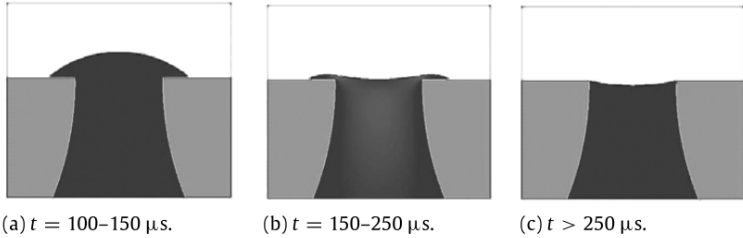


Figure 2-13: Nozzle plate wetting from overfilling [25]

The ink channel will then be filled with an unusually large amount of ink. In some occasions, the excess ink leads to a wetting of the nozzle plate. Another possible cause of wetting however is drop formation failure. When the drop fails to break off, drop speeds decrease until adjacent drops merge to form a large pending drop which eventually spreads to the nozzle plate. Since there then is an extra thin film on the nozzle plate, the channel impedance is increased. Higher pressure amplitudes thereby result from the reflection of pressure waves at the nozzle. Drop formation will not occur in the same manner as without this thin film. The added mass at the nozzle increases the inertia which has to be surmounted, leading to a decrease in drop speeds. This is however partly compensated by the higher pressure amplitudes. Furthermore, in the same way overfilling leads to nozzle plate flooding, the thin film on a wetted nozzle plate also induces further disturbances to the normal ink jetting behavior in the form of air bubbles. The vast majority is formed by air entrainment at the nozzle.

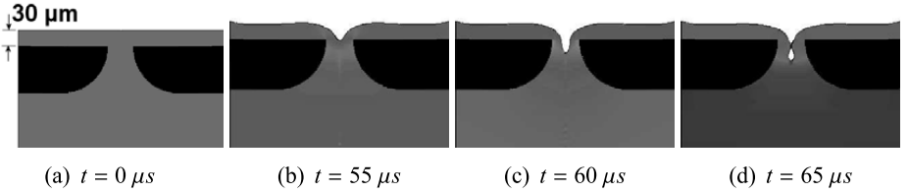


Figure 2-14: Air entrapment from flooded nozzle dynamics [25]

When the nozzle meniscus is pulled back, ink flows from the nozzle plate into the nozzle and forms an end cap to the air column that came in with the retreating meniscus. Depending on the position of an

air bubble in the ink channel, other behavior can be noted. For small bubbles, an increase in drop speed can be found due to the bubble oscillations resonating with the meniscus movement. However, after a certain limit has been reached, the drop speed falls rapidly with larger bubble sizes until drop formation eventually fails. The bubble is then of the same magnitude as the acoustic displacement and counteracts it. A possible way to eventually recover from air bubble disturbances is by jetting out the bubble. Other environmental conditions can also be found which affect the bubble: these are diffusion and dissolution. During operation, the bubble will grow by rectified diffusion. Dissolved air in the ink will diffuse into the bubble under influence of the acoustic pressure variations inside the nozzle. If no ink is being transported (meaning nozzle actuation has stopped), the rectified diffusion process will be brought to a standstill and the bubble will slowly decrease in size due to dissolution in the surrounding ink. It should be noted that dissolving a certain volume of air from the bubble takes 2 to 3 times longer in comparison to gaining it from rectified diffusion. Also, rectified diffusion is positively influenced by higher actuation amplitudes. By lowering both the waveform amplitude and the repetition rate, air bubbles can be removed from the nozzle through dissolution in the ink.

Careful waveform design should not only aim to prevent long tails, air bubbles and secondary drops but also to precisely deliver exact amounts of ink. A higher ejection volume cannot always be obtained by increasing the drop speed, and therefore the driving amplitude, as this also eventually implies the creation of fast satellites. Alternatively the driving pulse width can be increased, corresponding to an extension of the time during which ink is transported outwards. However as was earlier mentioned, the pulse width should be tuned to the first eigenfrequency of the ink channel. When deviating from this rule of thumb, a higher waveform amplitude is needed to obtain similar drop speeds. Another way to perform drop size modulation is by changing the driving waveform slopes. A smaller rising slope means less ink will be brought into the channel before ejection. In order to still deliver the same amount of energy, the amplitude of the second slope then needs to be higher. As a result, the waveform will have a negative going part of the second slope. Also, a third slope is introduced to discharge the nozzle before applying a new waveform. If this reasoning is applied to the original unipolar waveform, the totality of these modifications leads to the widely used bipolar waveform. These waveforms moreover have the additional asset of a much higher splitting speed. An insurmountable side effect however is the higher level of residual vibrations. Furthermore pre-actuation can be used to modulate drop size. Essentially this method relies on the fact that prior to the ejection of the main droplet, the nozzle is excited at a reduced level to push out a small amount of ink in front of the nozzle. This volume of extra ink is then carried along by the main droplet. In a similar concept, multiple droplets can be ejected in a short burst whereby the last droplet should have a higher speed. In this manner, the droplet will catch up with the slower ones and form a single droplet with higher volume.

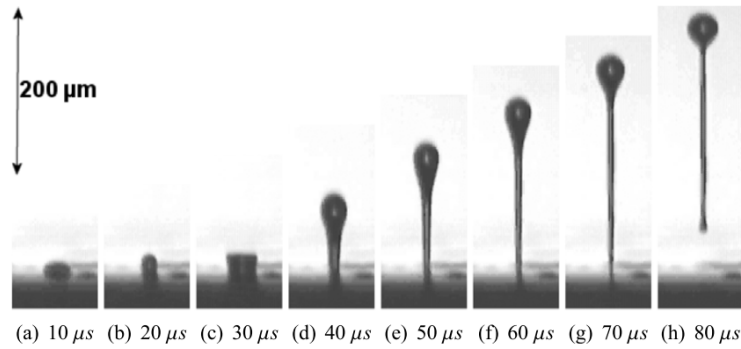


Figure 2-15: Pre-actuation followed by the main droplet at 30 μ s [25]

As a counterpart to pre-actuation, break pulses can hold back a small volume from being ejected if they occur while the main part of the drop is being pushed out. These pulses therefore can be used as yet another means of drop size modulation and incidentally even dampen residual vibrations. When combined with fast satellite formation, these break pulses can make sure only the small satellite drop is effectively ejected whereas the main drop formation is brought to a standstill. Very small droplets can thus be formed. Lastly it should be clear that the effective inside diameter of the nozzle also plays a role in defining the size of ejected drops. Yet its contribution is not extremely confining as the range of attainable drop sizes can even overlap between different nozzle sizes. [14]

Even though stable drop formation can be seen as a reproducible process, the first drop in any given ink jetting burst can often be found to deviate from the others.

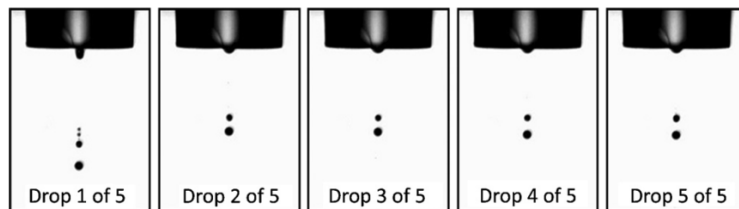


Figure 2-16: First drop dissimilarity [27]

This phenomenon is called the ‘first drop problem’ and can be observed even with only a small interval of about 30 ms between each burst. However, the same term is used to denote to dissimilarities which occur due to the presence of solvent evaporation and its resulting residue particles at the nozzle.

Because of the short time interval, the first kind is thought to occur regardless of evaporating solvent. Hypotheses around its origins are based on both acoustic instability and wetting of the nozzle. On one hand, acoustic instability could be established because the wait for subsequent acoustic pulses which mutually reinforce each other is too long between bursts. Wetting of the nozzle however will only occur once drops are being dispensed. The difference between the first drop and the other ones then lies in the fact that the first drop is formed at a relatively dry nozzle plate, while the rest isn't. This

makes for a smaller size of first drops in the first kind of first drop problem. On the other hand, irregularities which emanate from residue particles can be observed as nozzle clogging or misfiring.

A small summary is now made as an overview to this extensive section.

First of all, ink properties like viscosity and surface tension, along with the mechanical property inertia were found to influence drop formation and then used to calculate the Ohnesorge number which indicates the ease of printability of a certain ink for a certain nozzle. Next, capillary pressure variations inside the droplet, environmental noise and the acoustic properties of the ink channel were identified as influencing factors which are harder to control. Other decisive variables which can directly be controlled, were: drop speed, drop acceleration, timing of acoustic waves in the ink channel, nozzle plate wetting due to overfilling and the presence of air bubbles (balance between rectified diffusion and dissolution). They can respectively be controlled by adjusting the following parameters in the waveform: amplitude, rise and fall time, pulse width, amplitude (again) and the frequency by which the waveform is applied.

Methods to control the volume output were also presented. Changing the amplitude or pulse width of the waveform is the most straightforward method, but most likely alters other aspects as well.

Switching to a bipolar waveform and adjusting its positive to negative amplitude ratio is a first viable possibility, aside from alternatives like pre-actuation and break pulses. Naturally, the nozzle diameter also plays a role.

The section was ended by a remark about irregularities between the first ejected droplet and all following, called the 'first drop problem'.

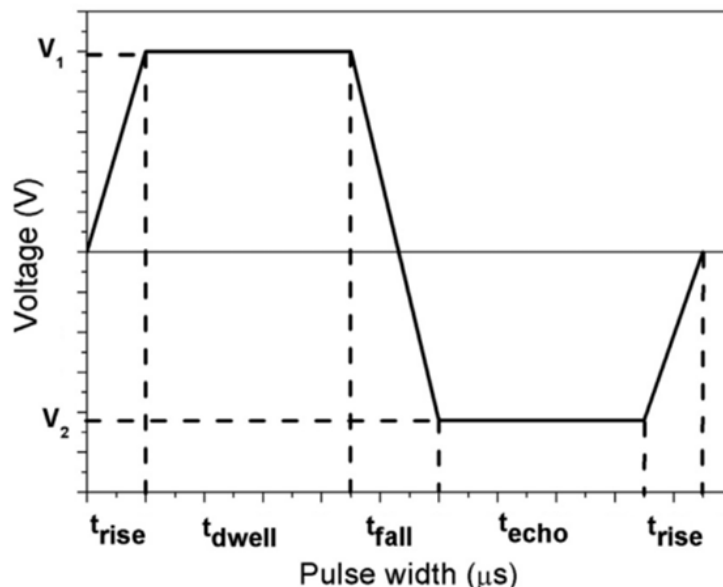


Figure 2-17: General form and parameters of a bipolar waveform [13]

2.3 Machine Vision

2.3.1 Fundamental parameters

Five fundamental parameters have to be taken into consideration when setting up an imaging system, these are: resolution, field of view, working distance, sensor size and depth of field. [28]

First of all, the minimum measurable feature size has to be determined. This feature size must correspond with at least two pixels in the digitized image. Next a field of view (FOV) needs to be chosen as to include all details under inspection but still be as small as possible. The minimum sensor resolution can then be calculated as follows:

$$\text{Sensor resolution} = \left(\frac{FOV}{\text{smallest feature size}} \right) * 2$$

Formula 2-2: Minimum sensor resolution [29]

At this point, the only thing left before choosing a camera is to balance a sensor size value (typically 1/3", 1/2" or 2/3") along with needed lens focal length according to:

$$\text{Focal length} = \frac{\text{sensor size} * \text{working distance}}{FOV}$$

Formula 2-3: Focal length [29]

With the working distance being the distance from the front of the lens to the object under inspection. The focal length then is coupled to the magnification of the object under inspection and to the viewing angle. Longer focal lengths result in a greater magnification and smaller angle of view while shorter ones result in wide angle images with less detail. Another lens parameter is called 'depth of field' and represents the ability of a lens to keep an object in focus with varying distance to the lens. Stronger variations require a greater depth of field and are typically solved by using telecentric lenses. Apart from a greater depth of field, these lenses also have a very low distortion and limit perspective errors. [30]

When placing the camera, special attention should also be paid to the attained perspective. An ideal situation would include a camera axis perpendicular to the object under inspection. Other perspectives complicate image processing but could still be used.

2.3.2 Lens

Lenses are typically chosen as to match the requirements of the previously mentioned analysis. However, the lens itself can introduce deviations in the resulting image. Normal, entocentric lenses exhibit both perspective errors as well as a varying magnification as the distance to the object changes.

On top of this the apparent shape of an object also changes as it moves out of the center of the FOV. Entocentric lenses hence cannot be used to make very precise measurements.

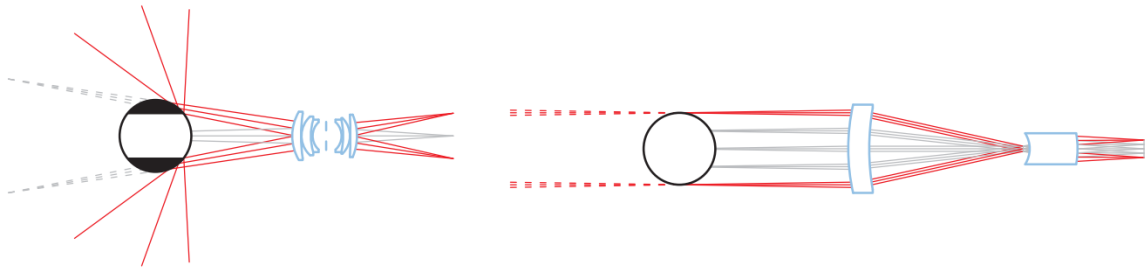


Figure 2-18: Comparison of entocentric (left) and telecentric (right) lenses [30]

To solve these issues, telecentric lenses can be used. These lenses are specifically designed to only pass collimated light parallel to the optical axis and therefore have essentially an infinite focal length. The formula containing FOV, magnification and sensor size, which was mentioned earlier, can in this case be simplified to:

$$FOV = (sensor\ size)/magnification$$

$$FOV = \frac{sensor\ size}{magnification}$$

Formula 2-4: Magnification for telecentric lenses [29]

Apart from a fixed working distance and magnification, their relatively high depth of field makes this type of lens easy to work with. Another strong point of telecentric lenses is that they do not suffer from the prism effect where white light is split up into its constituent wavelengths. The prism effect indeed can only occur if different wavelengths which refract under different angles are allowed to reach the image sensor, which is not the case for telecentric lenses. Only collinear light is allowed to pass so if a certain wavelength is refracted under a different angle, it won't constitute to the resulting image. This essentially means that the image will be sharper and better to perform measurements on. A last major advantage lies in the fact that there is no edge position uncertainty for backlit objects. Normally border effects make for an inaccurately defined edge because light from behind the object is reflected into the lens.

2.3.3 Lighting

Lighting is often referred to as one of the most important aspects of an imaging system. [31]–[33] It can significantly reduce image processing complexity and processing time by enhancing the quality of the image which is being fed to the image processing software.

Generally speaking there are three acceptance criteria for a machine vision lighting analysis. First of all the features of interest should have maximum contrast while, secondly, the contrast elsewhere should be minimized. Finally the chosen lighting setup should suffice for all occurring imaging circumstances.

A variety of lighting sources can be used. These range from fluorescent and LED to mercury and xenon and are characterized by their intensity, spectral content, life expectancy and heat output. The most widely used sources are fluorescent and LED, while xenon is usually limited to strobing applications and mercury to fluorescence studies.

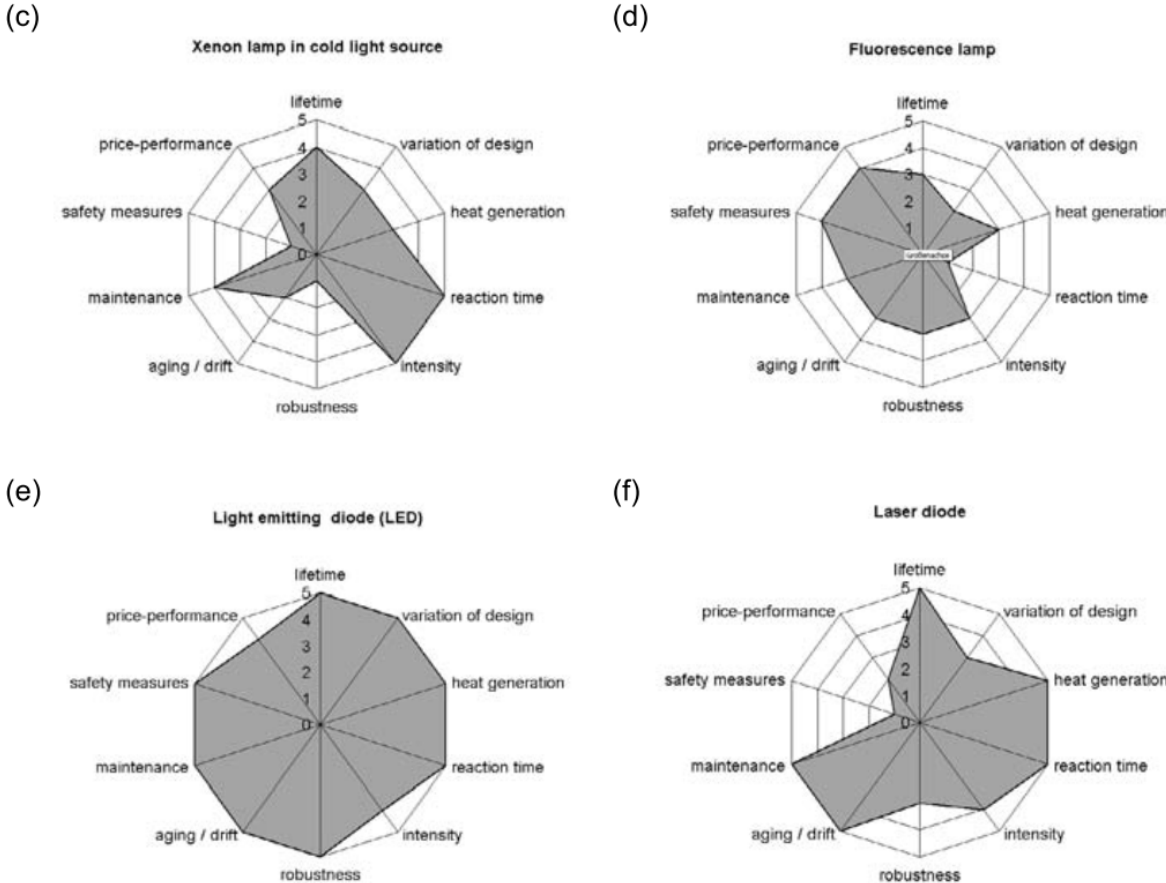


Figure 2-19: Comparison of typical light sources [29]

As is the case for all lighting needs, LEDs are increasingly more used in machine vision applications, even as a strobed lighting source. They emit almost monochromatic light, achieve higher and higher efficiencies with every new development and have the highest life expectancies. Moreover, a ten-fold current overload can be applied in strobed operation if the duty cycle is kept low enough. This results in an up to ten times higher lighting intensity. [29]

If an even higher intensity is wanted, be it continuous or flash based, Xenon lamps are found to be the most common solution. Their almost continuous spectral output makes for a balanced white light which makes sure the original colors of any imaged object are not influenced during illumination.

Flash durations vary from 1 μs to several milliseconds. Frequencies of up to 1kHz are possible while keeping a life expectancy of millions of flashes. Its usage however isn't always practical due to the large and expensive peripherals necessary for operation and the fact that it relies on high voltages. [29]

Laser light sources form another alternative but rarely find usage in machine vision. There are two main reasons for this: safety issues and speckle. The safety issues are based on the very high intensity light that lasers produce, up to the point of being harmful to operators. Speckle patterns on the other hand are in fact interference patterns between the emitted coherent light waves. These patterns constantly change over time and can complicate or even prohibit further image processing.

To optimally use its output, sometimes a matching of lighting source spectral content to camera sensor spectral sensitivity is performed. Furthermore, narrow wavelength sources can be coupled with a band pass filter to shield the system from ambient light and thus make it more independent from its environment. Other ways to deal with ambient light are physical enclosures or high power strobing with short duration pulses.

The sample surface – light interaction is another field of interest for machine vision. Differences in the sample surface's nature (shape, geometry, reflectivity, ...) lead to different amounts of light reflected to the camera, as do changes in relative lighting position to the sample surface. In a worst case scenario, lighting artifacts like glare can always be removed by using polarizing filters. Variations in penetration depth are also found. IR light is better at penetrating polymer materials while deep blue or UV light is preferred for imaging surface features.

Four basic illumination techniques can be used as a starting point to apply the above principles on. The first one is back lighting and is used to detect or measure objects with maximum contrast. Next we have diffuse (full bright field) lighting for surfaces which tend to reflect. Directional (partial bright field) lighting on the other hand performs poorly on specular surfaces, creating a hotspot reflection.

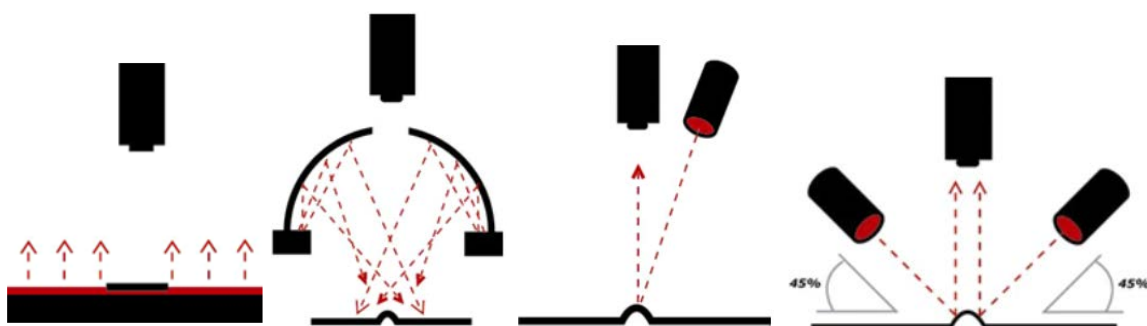


Figure 2-20: back, diffuse, directional and dark field lighting, left to right [33]

Its directionality can however be used to enhance detail. Dark field lighting finally is used for emphasizing surface imperfections as only the light which is scattered by the sample can be

directed into the camera. Bright field and dark field images differ mostly in the fact that the first is the result of high angle incident light, while the latter originates from low angle incident light.

2.3.4 Camera

Many different camera options can be chosen from while composing a vision system. First of all, one has to differentiate between analog and digital cameras. Both terms allude to electronic cameras, leaving film-based cameras aside as they are not interesting to machine vision. Every imaging action essentially begins in the analog domain: photons are converted to electrons in the photovoltaic effect and amplified to a voltage which can vary continuously. Afterwards a choice can be made to move on to the digital domain for signal processing or to stay analog. Analog cameras are characterized by the fact that from ingoing light to outgoing signal, every step in between uses analog signals. Analog signal processing (ASP) is a field of its own, be it very limited when compared to digital signal processing (DSP). When using an analog camera, a PC frame grabber is necessary to make image processing possible. The frame grabber digitizes its incoming analog signal into discrete frames, essentially behaving as an analog-to-digital converter (ADC). One of the biggest disadvantages of analog cameras is their vulnerability to noise, making them less precise and consistently performing. Digital cameras on the other hand convert the continuous information from the camera sensor, after ASP (which is still needed), into discrete levels represented by bits. This enables the use of sophisticated DSP and digital image processing features making these cameras more versatile and fit for bad imaging environments. Also, since digital signals are immune to common noise, the only possible moment for noise to interfere is before ADC quantization; at the image sensor and ASP circuitry. Most digital cameras transfer their image data through Firewire, USB, Camera Link or GigaBit Ethernet. Some however reconstruct their digital data to an analog output signal, offering the advantages of a digital camera while still being compatible with analog setups.

If we only consider image sensor technology, machine vision cameras can be divided into two groups: CCD and CMOS. A CCD or Charge Coupled Device was first invented for analog storage and shift registers. It consists of a series of special on chip capacitors which store charge. By alternately driving different capacitor pads, the charge can be 'led' from one capacitor to another. After realizing that silicon also is light sensitive, CCD arrays were used as imaging sensors. Each capacitance would now act as a pixel and store charge equivalent to its incident light. Charges are then shifted out of the sensor towards output amplifiers and ASP circuitry. This can be done based on three methods. 'Full frame CCD' as a first method shifts the obtained charges directly out of the exposed CCD array and needs an external strobe or shutter. Second, 'frame transfer' first shifts all charges from the exposed array into a dark, storage array before shifting it further to the output. Third and last, 'interline

transfer' shifts every column into an accompanying storage CCD shift register. By doing this, a new image can be obtained while the current one is being shifted out. Interline transfer by itself can be done by reading and showing one image alternately as only the odd or only the even rows. This is called 'interlaced' and its sole reason for existence are historical limitations in readout speed, but it still is considered an industry standard. The need for a storage CCD shift register half the size of the column length is an asset. A disadvantage however is that it isn't suitable for imaging moving objects because odd and even lines are exposed differently. Another way of performing interline transfer is 'progressively'. This is the more straightforward approach where the shift register is of the same size as the image height and thus further reduces the exposable surface area. All pixels are moved into the storage shift register at the same time. This makes precise control of the integration time possible as its operation describes a global electronic shutter.

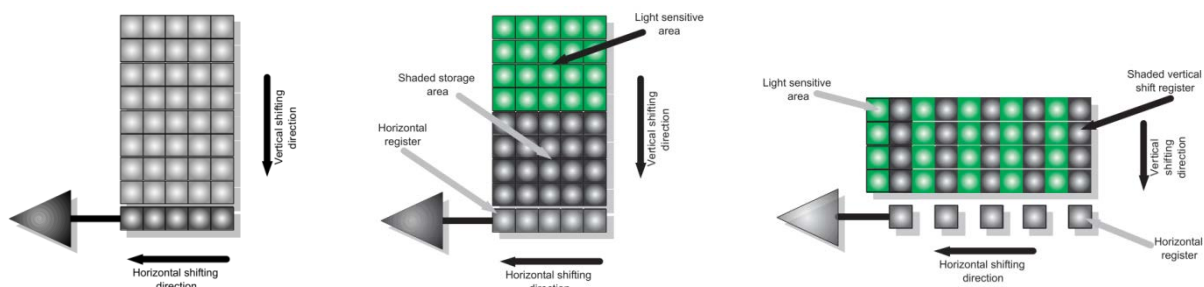


Figure 2-21: Full frame CCD, frame transfer and interline transfer [29]

CMOS sensors (Complementary Metal-Oxide Semiconductor, named after the technology used) on the other hand do not shift charges around to output amplifiers but instead convert the charge into a voltage using extra circuitry which is built into every pixel. This reduces the sensitivity of CMOS per unit area compared to CCD. However, each pixel now is individually addressable making windowing very easy and a lot faster because only the necessary pixels are read out. Very high pixel rates can be obtained as no charge needs to be shifted around and the outputs can be multiplexed. This makes it a suitable technology for high speed imaging, but only when configured with a global shutter. Cheaper versions have a simpler, rolling shutter which resets the image line by line after reading it. CMOS sensors can also contain additional components such as AD conversion and a timing generator on-chip where as they would've been separate components in a CCD camera.

Within the above mentioned camera categories, further differences lay in the particular specifications details. A certain camera type can differ between models in terms of resolution, image throughput or FPS, number of inputs and outputs, quantum efficiency, sensor size and the fact if it registers color or black and white (mono). It should be noted that color cameras are made by adding filters to black and white pixels to obtain RGB information. Consequently, these filters each block two thirds of the

spectrum which makes every color cameras per definition far less sensitive in comparison to its mono counterpart.

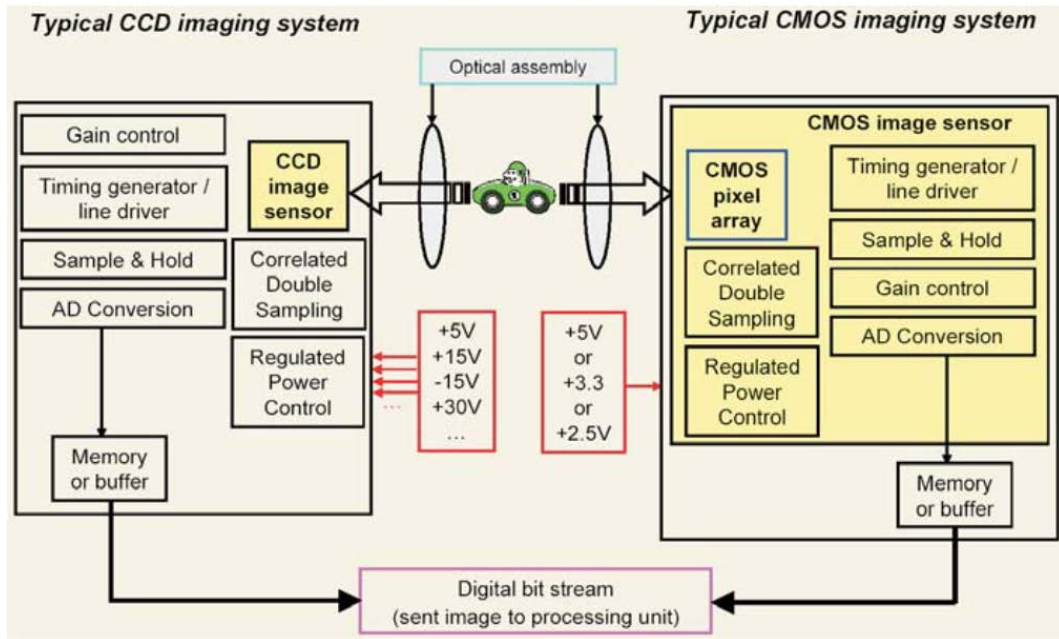


Figure 2-22: CCD to CMOS integration comparison [29]

Sensitivity considerations also apply to the sensor's resolution. More pixels on the same sensor size means less area for incident light on each pixel. A higher resolution variant of a certain size camera sensor therefore is less sensitive since the same amount of incident light is divided among more pixels. Another measure of sensitivity is a camera's quantum efficiency. It indicates the yield of photons which successfully produce charge carriers (electrons) in the photovoltaic effect and is given as a percentage. By combining these aforementioned considerations, a camera with a certain sensitivity can be selected to match a specific application. Typical high sensitivity applications are high speed imaging and imaging under low light circumstances. The maximum possible frame rate however is not only linked to the sensor's sensitivity, it can also be bottle necked by slow performance of the accompanying readout electronics or image processing system. Lastly, the number of inputs and outputs is only important in consideration to the vision system's intended triggering and monitoring operations. It does not affect the imaging operation per se, but can be used as a means to control it.

3. Materials and methods

3.1 Ink jetting, imaging and triggering methods

3.1.1 Ink jetting

From literature study it was derived that ink jetting can be done using one of following methods: continuous, electrostatic or drop-on-demand. Since drop-on-demand (DoD) is far more reliable and versatile than the others, it is the preferred method for using in drop formation studies. Within the DoD technology there is another subdivision: bubble jet DoD and piezo DoD.

Bubble jet DoD ink jetting utilizes thin film heaters to locally heat the ink in order to produce a gas bubble. The gas bubble exerts a pressure on surrounding ink, thereby pushes it out of the nozzle and causes an ink drop to break off when the bubble collapses. It is the most common ink jet technology, used in everyday home printers, but is far from versatile in tuning drop size and speed. Also, because the ink is being heated, contamination of the ink occurs by burnt particles and direct contact with the thin film heater. Because of this vicious self contamination cycle, drop formation circumstances continuously change therefore the drop formation process will not be consistent through time.

Piezo DoD ink jetting on the other hand is a much cleaner and versatile method. It comprises a glass capillary being alternatively squeezed and expanded by a piezo element in order to split off droplets. The chemical contents of the ink thereby are in no circumstances altered. This makes for a more stable drop formation coming from better consistency of the ink's formulation. The pressure is now regulated directly by the piezo element and therefore tuning of its driving signal will have more direct implications in the drop formation process. For its clean, stable and precisely tunable operation, piezo drop-on-demand printing is preferred in functional printing above bubblejet.

3.1.2 Image acquisition

Based upon the findings in literature, a few methods were looked into for imaging fast travelling inkjet drops. But first a list of minimum requirements was composed to keep in mind. It was found in literature that *ad extremum* small droplets of about 5 μm travelling at velocities of up to 15m/s can be created by piezo ink jetting. More practical minimum requirements were hereof deduced stating that a droplet with 10 μm minimum drop size and 10m/s maximum drop speed should be imaged across a 1mm gap from nozzle to substrate. The imaging rate is not of great concern as a standard frame rate of 30 images per second would already suffice to draw relatively fast conclusions about a tested ink-waveform combination. By enlarging our region of interest from a certain area along the path from nozzle to substrate to the whole path between nozzle and substrate, the best overview of the whole

drop formation process is made. The system is therefore envisioned to be more versatile as it would provide insight into, apart from the actual drop formation, oscillations in the nozzle, bounce back at collision and eventually spreading on the substrate. Very short exposure times furthermore have to be attained since small, fast moving objects are imaged and motion blurring would otherwise easily reach the same order of magnitude as the droplet's size.

Three main approaches were thought of for acquiring images from the falling droplets: First of all a super high speed camera can be used, combined with a constant light source. Second a normal speed camera can be operated in continuous mode, capturing images at its maximum frame rate, with a strobe light that is synced to the jetting device. Last, an adaptation of the second method can be performed whereby both the camera as well as the strobe light are synced to the jetting device.

High speed camera

A high speed camera would be the most straightforward approach to this problem. It would continuously record images, capturing every behavioral detail of a single droplet as it falls. The main assets of this approach are the ease of imaging operation, low component count and low overall system complexity. The camera would be fitted with a proper lens to obtain the 1mm FOV and be used in conjunction with a high intensity continuous backlight. However, due to the large size, weight and price tag of the camera on its own, it would not be a viable solution and will not be further discussed in this dissertation.

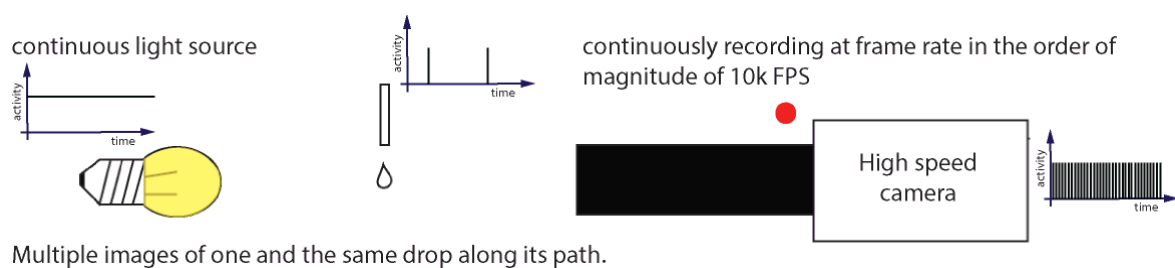


Figure 3-1: Schematic overview of high speed camera observations

Continuous mode camera, strobe light synced to jetting device

Drop formation can also be imaged by placing a continuously running camera in front of the jetting device while a strobed backlight illuminates it from behind. By tuning the strobing frequency to the droplet stream, images can be obtained of droplets while being ejected. Specialized ink jetting equipment from Microfab and Microdrop are equipped with a dedicated output for syncing light strobes with the nozzle's driving signal. If the delay between the driving signal and the light pulse is altered, a different moment in the drop formation process can be viewed. At high drop rates, the drop emission frequency will surpass the imaging frequency of the camera. A single image from the camera will contain information from multiple ejected droplets. Effectively, an overlay of the different drops

can be observed in the resulting image. Because of the high reproducibility of stable ink jet drop formation this is not a problem. Each time a drop is formed with the same driving waveform, it will exhibit the exact same dynamics and result in the same image. This also implies that multiple strobe flashes contribute to the image. An imaging operation which has two flashes in its exposure time will naturally yield an image which is twice as bright. The same reasoning applies to images with even more strobe flashes. Therefore images acquired in this manner will be more clear.

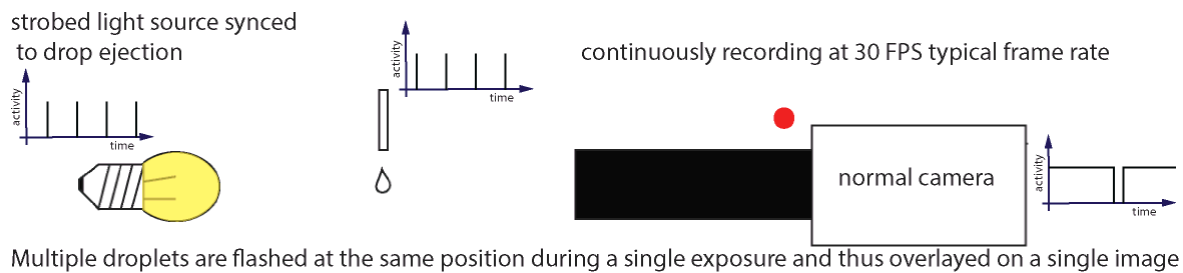


Figure 3-2: Schematic overview of continuous mode camera imaging w/ strobe synced to nozzle

This approach however would add an extra layer of complexity as, apart from a camera, lens and backlight, now a strobe controller would also be necessary. Furthermore the timing between strobe controller and jetting device is a critical aspect for stable imaging. Aside from a boost in clarity, the contribution of multiple droplets to a single image can on the other hand be seen as a loss in accuracy. In practice the timing between components as well as the drop formation reproducibility will not be 100% consistent. Therefore the position of multiple droplets will not exactly line up when overlaid in a single image. It will thus not be completely representative for a single drop formation action. Even more important maybe is the fact that it would be impossible to observe irreproducible events which differ for every drop formation process. It is a viable solution because small, relatively low tech components can be used, giving the system not only the portability but also the affordability which was envisioned. Alternatives should however be further looked into.

Triggered mode camera, both strobe light and camera synced to jetting device

The last inspected method for imaging ejected droplets is even more bound to critical timing between each component. Not only the strobe light is synced to the jetting device, but the camera is as well. Only a single droplet will be observed during the length of each image capturing operation, therefore no accuracy is lost in comparison to the high speed camera approach. The camera is set up in the same way as in the previous method but instead of continuously running at its highest frame rate, it will only acquire an image when triggered by the ink jetting device.

Different component triggering concepts result in different behavior in consideration to the jetting frequency. This concept adds timing complexity to the free running camera method but further requires the same equipment, including the strobe controller. It however does not suffer from all the

setbacks from overlaying information of multiple drops. Irreproducible events can also be inspected but the images will be less clear when using the same flash intensity. This method is favored over the previous one as it makes more efficient use of the necessary equipment.

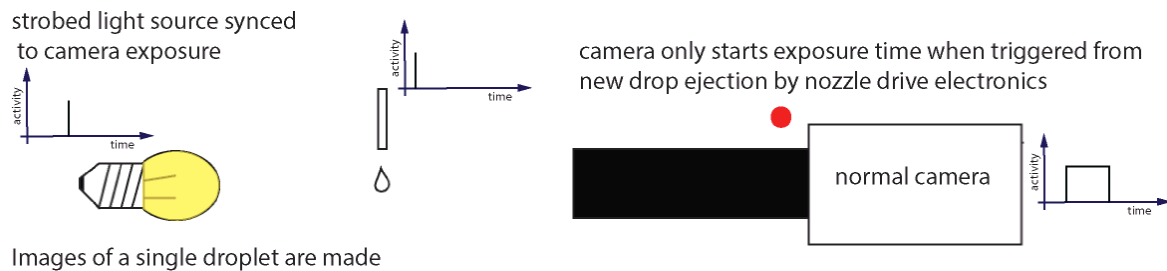


Figure 3-3: Schematic overview of triggered mode camera imaging

3.1.3 Precise timing between components

The image acquisition method of choice has very strict requirements regarding the triggering of individual components. Each component has to be triggered on a distinct moment in time with as less jitter as possible. Two methods were looked into for this aspect: one controls everything from the top level meaning the control software that sits on top of the hardware setup, the other on specific hardware for sending triggers with possible preprogrammed delays.

From control software

One could be tricked into believing this behavior can be gained from dedicated software running within a standard operating system environment. Surely, when using a development environment like LabVIEW, counters are available to rely on for activating certain functions at a preset moment. An internal event could then send a triggering signal over a DAQ interface to the corresponding equipment which should be triggered at that time. However, due to the very nature of a standard operating system, its precision is inherently limited to the millisecond range. The resulting timing would not be suitable in terms of resolution nor in consistency as the processing of events within the program can always be interrupted by critical system components.

Non standard operating systems were then looked into as a possible solution. So-called Real Time operating systems are specifically designed to meet precise and consistent timing requirements of software. A real time module even exists as an extension of the LabVIEW environment which brings precision levels to the microsecond range. It however requires specific hardware with enhanced drivers for running the RT environment and I/O would only be possible to hardware which also has drivers supporting real time operation. The imposed timing requirements would be met after building such a system but in itself the act of building it is not trivial. The ability to run normal Windows programs

aside from the main program would be sacrificed as well as having a straightforward graphical user interface.

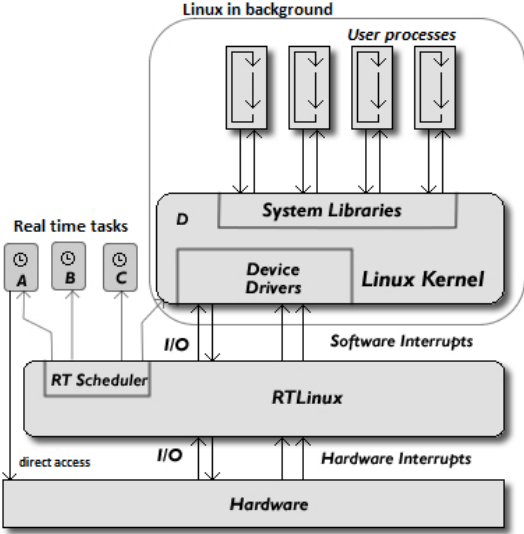


Figure 3-4: RT OS as an extra layer between OS and hardware [34]

Using real time software would in theory be a valid option in meeting the precise timing constraints. It is however likely that this approach imposes more additional problems than it solves.

Relying on hardware

A separate dedicated timing controller can also be used. Once triggered, it activates its outputs one by one based on a timing schedule which is programmed in beforehand. On one hand such a piece of dedicated hardware does meet the necessary time resolution and precise repeatability, but on the other hand it increases component count and the corresponding price tag of the system sensibly.

A final approach would rely on the outputs of each component for triggering each other. Machine vision cameras and drive electronics for laboratory ink jetting equipment in most cases are found to have outputs specifically for interacting with peripherals. While machine vision cameras have general purpose inputs and outputs which can be configured through software, ink jetting drive electronics only feature a strobe output for synchronizing with a strobe light. Since these outputs are designed for timing purposes, their performance thus is certainly adequate. A major advantage of this method lies in the fact that no additional components are needed. By delivering the necessary timing behavior at no extra cost, this method is preferred above all others.

3.2 Component choice

3.2.1 Ink jetting components

Ink jet testing equipment from different vendors was identified from which subsequently the parts presented below were selected.

Printhead

The PH-47 room temperature printhead from Microfab was chosen. It features a 25ml removable glass reservoir and its typical drop volume range goes from 5pl up to 0.5nl. MJ-AT-01 nozzles with orifice diameters of 10 to 80 μ m can be used. For this case, the 80 μ m orifice is used because it enables the highest possible drop size range and thus makes sure the drop size can be increased if difficulties should arise with imaging very small droplets.

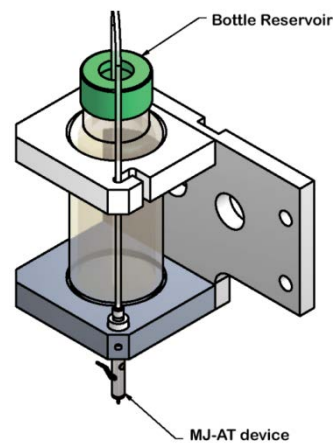


Figure 3-5: MicroFab PH-47 printhead [35]

Drive electronics

The Microfab JetDrive III is used for delivering unipolar or bipolar waveform driving signals to the piezo inkjet nozzle. The waveform can be configured in a piecewise fashion through the JetDrive's RS232 interface. The maximum amplitude is from +140V tot -140V and can be adjusted in 1V steps. A DC component can also be added. Furthermore, the rise, dwell and fall times allow for 1 μ s adjustment steps. Revision D was used in this study which supports a total pulse length of 4095 μ s and maximum width of a single timepiece of 3276 μ s. Operation is done either in single mode or continuous mode. In single mode, a certain amount of drops is ejected per trigger event. In continuous mode jetting starts at the trigger and continuous until a specific command is given to make it stop. Lastly, it also features a strobe signal output for triggering an external strobe light. The delay between driving waveform and strobe signal output is also configurable through the RS232 interface.



Figure 3-6: JetDrive III nozzle drive electronics [36]

3.2.2 Machine vision components

When translated into the machine vision domain, the following criteria are noted: a region of interest of about 1mm, 200ns maximum effective exposure time, a relative resolution of minimum 1 pixel per μm and a minimum frame rate of 30fps. Even though the choice of components was done relative to each other, each of them will now be addressed briefly in an order which seemed most logical to the author.

Camera

The primary features for which the Allied Vision Tech Manta G-125B camera was chosen are its global shutter and 1296x964 pixel resolution. [37] The former ensures high timing precision is possible by exposing all pixels during the same interval while the latter ensures a high spatial precision. Mounting of this camera will be done sideways to align its highest resolution axis with the path from nozzle to substrate. At full resolution, the 30fps minimum requirement is aptly matched. Higher frame rates can even be achieved when the region of interest is limited to a subsection of the full image height. Another important feature is its small pixel size. At only $3,75\mu\text{m} \times 3,75\mu\text{m}$ more details will be made visible for the same magnification level, contributing to a higher precision. The Manta series is advertised as a sensitive camera, built around the Sony ICX445 sensor. Its 50-55% peak quantum efficiency is reached at a wavelength just below 600nm. The G-125B's exposure time can be set as low as $21\mu\text{s}$.

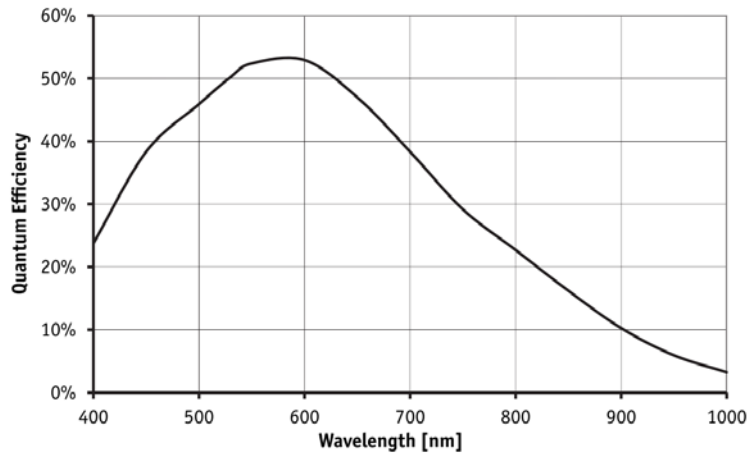


Figure 3-7: Manta G-125B spectral sensitivity [37]

A mono camera was preferred above color for the intended application because of its more efficient handling of incident light, meaning that no selective filtering is applied. Also, color feedback just is not of effective interest for the intended use. Connecting the Manta G-125B to peripherals can be done either through a Gigabit Ethernet port or 12-pin Hirose connector. Image transfer, altering imaging parameters and software triggering can all be performed through the Ethernet interface. The Hirose connector on the other hand holds connections for power, GPIO and RS232. [37] The GPIO's can be configured to initially receive a hardware (not necessarily TTL) trigger for starting image caption and subsequently wait for a precisely timed interval before sending a trigger to synchronize the flash. On the mechanical side this camera is small and light weight, ideal for building a testing platform which should remain more or less portable.

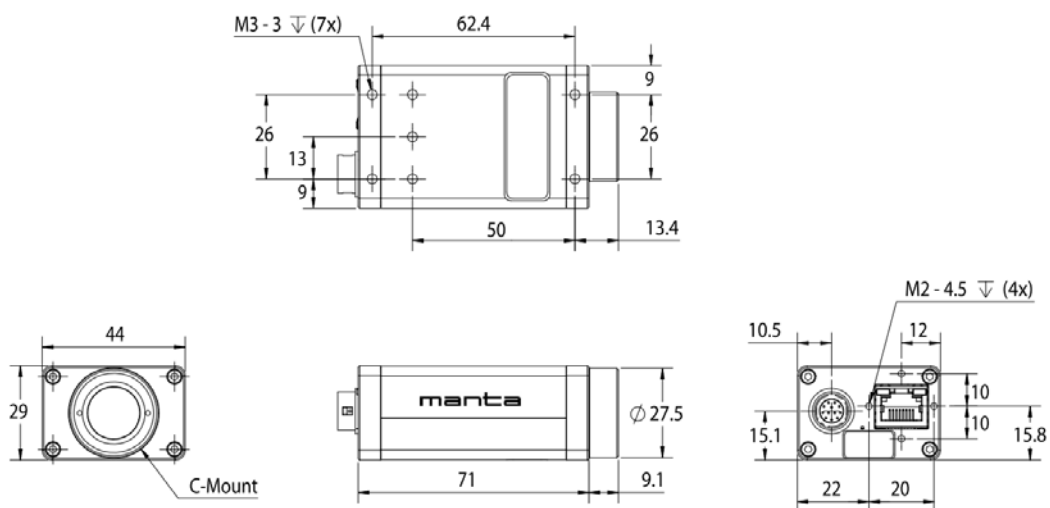


Figure 3-8: Manta camera technical drawing [38]

Lens

Complementary to the Manta G-125B's $3,75\mu\text{m} \times 3,75\mu\text{m}$ pixel size is the 4 times magnification level of the Opto Engineering TC4M 004-C lens. The combination of both elements makes for an ideally sub-micrometer precision. Every pixel in the resulting image then corresponds to a $0,9375\mu\text{m}$ distance in real life (3,75 divided by 4). This lens is furthermore of the bi-telecentric kind. It reduces deteriorating influences from reflection and diffraction and features a constant magnification level. Its working distance from lens to object has to be set to 57,1mm and its rather large image depth of 0,1mm can compensate small spacing variations. From a mechanical point of view it is a large, heavy lens about twice the length of the Manta camera it is attached to.

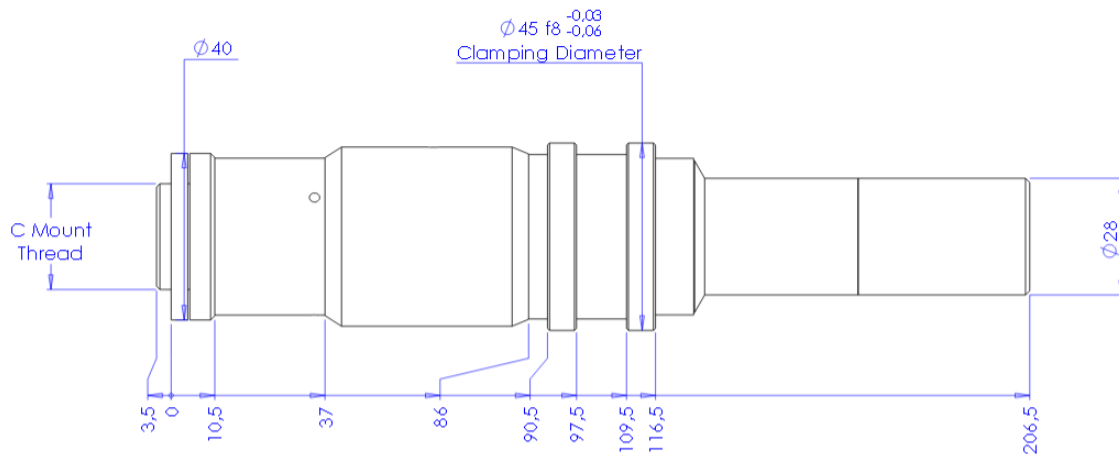


Figure 3-9: TC4M-004C technical drawing [39]

Lighting

Opto Engineering LTCL 023-G

To further supplement the telecentric setup, an Opto Engineering LTCL 023-G telecentric backlight [40] was added. It further reduces errors and since the emitted light is collimated, far less will be rejected by the telecentric lens. The telecentric nature of the lens indeed makes it so that only collinear light is allowed to pass to the sensor. The led used in this backlight is a green Seoul Semiconductor X42182 Z-Power Series led with typical 525nm dominant wavelength [41]. Wiring the backlight can be done in two ways: through a built-in control circuit which allows for dimming the lamp using a screwdriver or directly by circumventing the control circuitry and wiring directly to the led. Even though the led's datasheet mentions a 1000mA absolute maximum forward current (at $T_j = 90^\circ\text{C}$), the lamp is only rated for 350mA forward current by Opto Engineering. The most logical reason for this would be due to thermal constraint considerations from the lamp design. Another important feature from the X42182 led is that its datasheet already mentions guidelines for overdriving the led in pulsed operation. At a frequency of 1kHz and at 10% duty cycle a forward current of 1800mA can be attained. The lighting efficiency is expressed in lumens per watt (lm/W). Calculated from a 350mA

forward current, 3.25V forward current and 70lm typical light output, this would come in at slightly under 80lm/W.

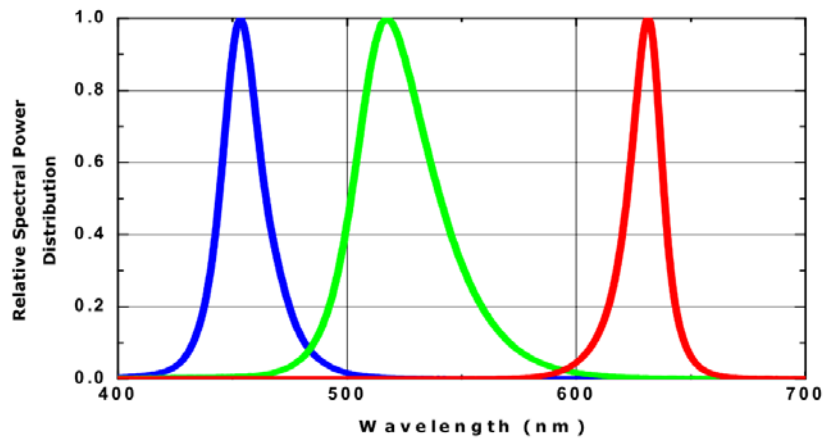


Figure 3-10: X42182 relative spectral power distribution (only green is relevant) [41]

Generic 10W power led

Temporarily chosen as a stand-in, this led is subjectively noted to emit a lot of light. No datasheet was found as this part was not specifically purchased for the flash photography system and efforts in identifying a manufacturer or part number did not work out. The led die consists of a 3 by 3 array of smaller led's and has a forward voltage of 9-12V depending on the current applied. The maximum current rating for continuous operation is 1000mA if a decent heat sink is applied.

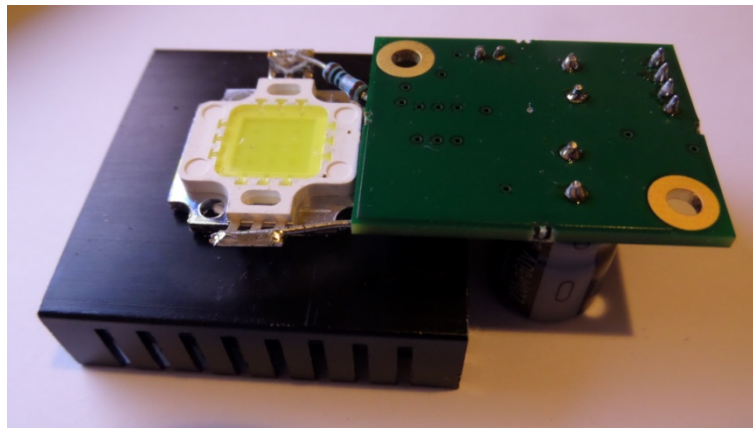


Figure 3-11: Generic power led with attached PP880 drive module

Cree XLamp XM-L U2

Another led light source was selected based on its high lumen output, forward current rating and large amount of available information: the Cree XM-L U2 [42] from the XLamp product family. Its main characteristics include: a 3000mA maximum continuous forward current rating, 150°C maximum junction temperature, 125° viewing angle and 300lm minimum luminous flux at 700mA forward current and 2.9V forward voltage. The resulting luminous efficiency is calculated to be no less than

147lm/W. The purpose of this higher efficiency led is to emit more light during the short lighting interval and thus increase the overall image brightness. Its dominant waveform is situated around approximately 445nm but since it emits cool white light, more constituting wavelengths can be found in the spectral power distribution. The typical turn-on time of Cree XLamp leds is also given and is a very useful fact for the current application. It is rated at 10 nanoseconds or less. [43]

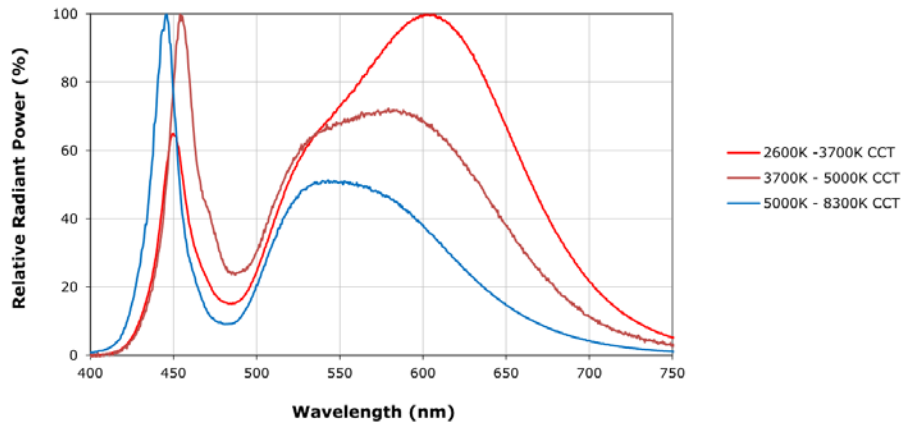


Figure 3-12: Cree XM-L U2 spectral output depicted in blue [42]

Strobe controller

This certainly was the most difficult component to source because of the extreme timing constraints. A Gardasoft PP880 was ultimately selected. The main reason why it was chosen is because it is able to pulse a led lighting source for a duration of 0.1 μ s up to 2ms in 0.2 μ s steps. This means it can deliver a pulse width which is half of the already extreme 200ns initial requirement stated at the beginning of this chapter. The strobe controller moreover features eight separate driving output channels, a trigger input and an RS232 interface. Also a delay can be imposed on the output in reference to an incoming trigger pulse. This delay can range from 5 μ s to 2ms in 0.2 μ s steps. Two separate power supplies can furthermore be used on a single PP880: one for the logic circuitry and one for the driving electronics. The driving signal amplitude is limited to 3 volts below the drive electronics power supply voltage and fully adjustable for each separate channel. The maximum driving electronics power supply voltage is 48V so a driving pulse can have an amplitude up to 45V. All adjustments to the drive pulse parameters can be made through the serial interface and saved to non-volatile memory. A minor flaw for the PP880 was found in the fact that it does not support constant current driving, a feature which is very useful when working with led's. Instead, a current limiting resistor should be placed in series with the led while it is driven with constant voltage.

3.2.3 Mechanical support

A mechanical base was designed by a colleague to fit the backlight, ink jet nozzle and camera. It enables the precise alignment of each component as necessary to place the nozzle in the camera's 1mm

FOV. Some flexibility was also provided in the mechanical support. By fixing the z-axis of every component's clamping structure with threaded holes and rods, all components can be adjusted in height separately. Along with z-axis control, the nozzle also was provided with a separate sliding mechanism for adjusting it along the optical axis. This adjustment was made so the operator would be able to manually put the nozzle in focus. In a later revision, threaded holes and rods were added to this sliding mechanism for the optical axis. It reduced both blockage of the sliding mechanism as well as the strength necessary to perform adjustments, allowing for more precision.

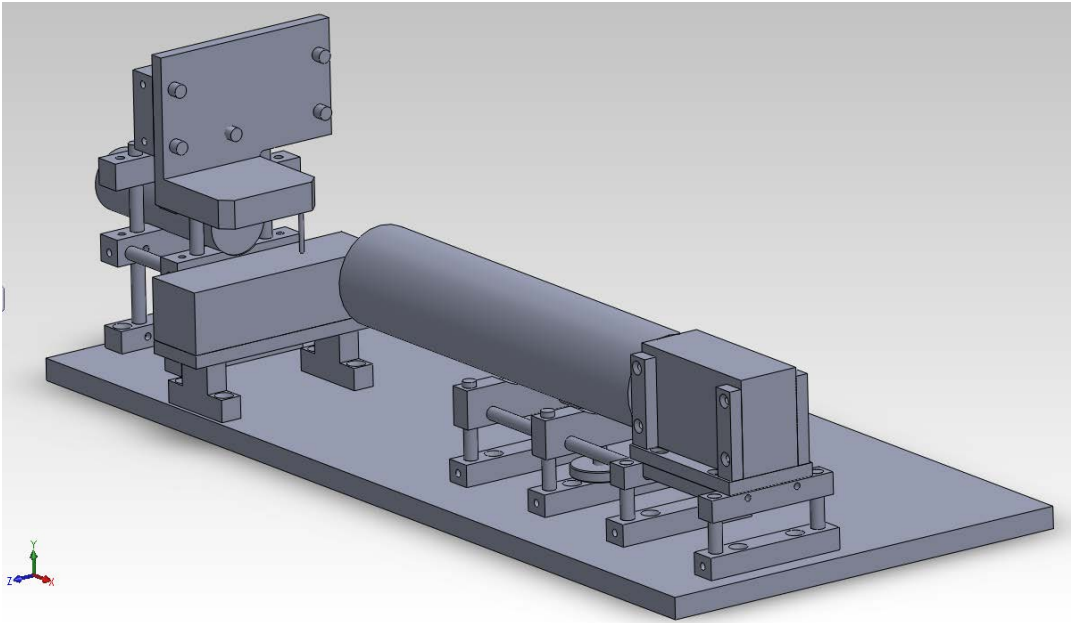


Figure 3-13: CAD design of mechanical base

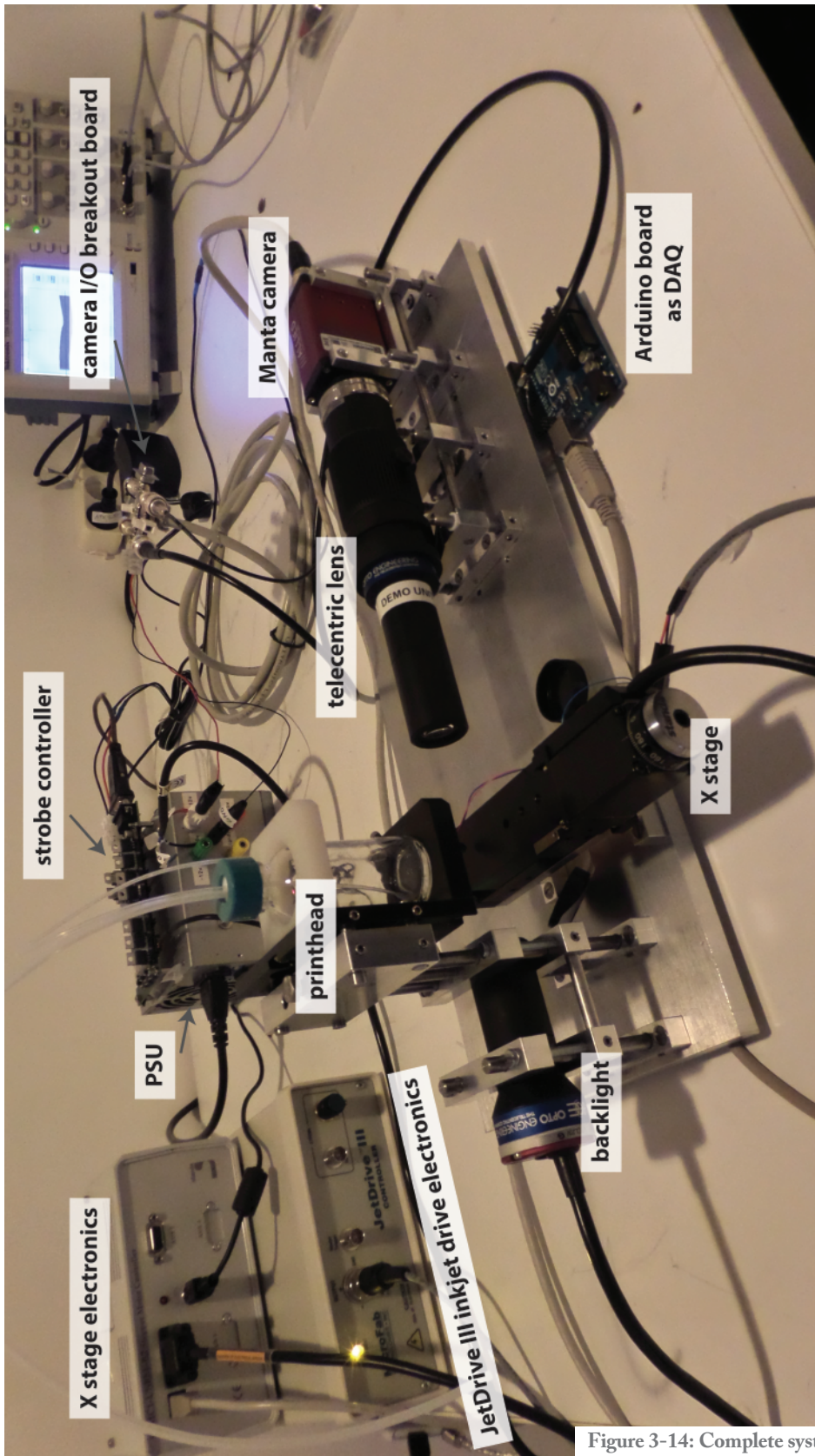


Figure 3-14: Complete system overview

3.3 Implementation of the trigger system

A decision was already made to obtain precise timing constraint in the setup by using hardware delay timers and triggers between components. Now that the parts are identified, special care should be taken in wiring them all together. To obtain a single drop formation image, everything should be timed respective to the moment the ink jet driving waveform is applied to the nozzle. Relative to this, the camera should start to record an image a few microseconds before the moment which needs to be inspected. While the camera is already exposed, the strobe controller should furthermore pulse the strobe light in the middle of the exposure operation. The moment in which the image is made ultimately corresponds to the moment wherein the strobe light is flashed.

Before wiring everything together, a brief look should first be taken at the different input and output specifications and possible wiring variations. In total the following components should be interfaced to each other: ink jet drive electronics, camera and strobe controller.

3.3.1 Component I/O specifications

JetDrive III

The JetDrive III manual states that both its external trigger input and strobe output are of the 5V TTL kind. The pulse width of the strobe output was found to be about 5 μ s. Its logic high level however was found to be little over 3V.

Manta G-125B

The Manta series of cameras has two opto-isolated inputs and two opto-isolated outputs. Each input can be driven without current limiting resistor for voltages up to 24V DC.

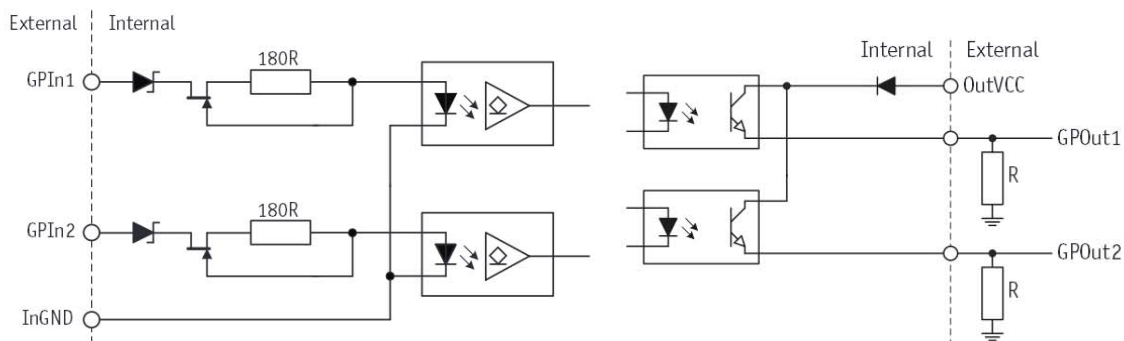


Figure 3-15: Input (left) and output (right) schematic for Manta camera

Input signals within the range of 0V to 1V are processed as a logic low, 3V tot 24V as a logic high. The minimum input pulse width is 6 μ s and a debounce time of 44 μ s is always in place. As stated before, the JetDrive strobe output pulse amplitude is about 3V. This is only just above the minimum requirement of the Manta's input high logic level. Therefore an amplifier circuit was constructed

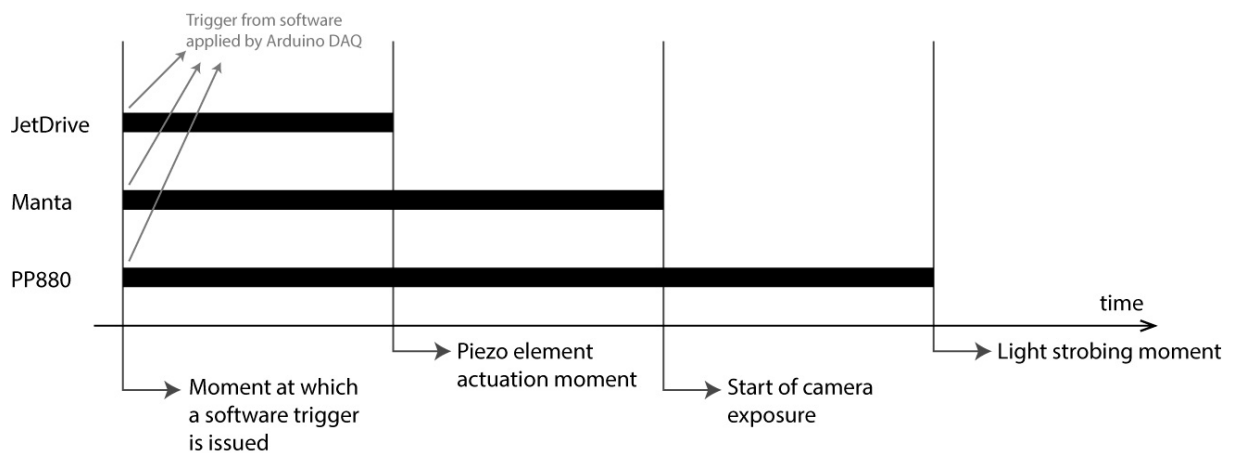
consisting of two inverted amplifier stages based on logic FETs. This circuit would rescale the 3V pulse to an amplitude corresponding to the rail voltage fed to it. Even though 12V would also be possible, 5V were fed to the amplifying circuit coming from the Arduino.

PP880

The only logic input of interest in timing here is the sole external trigger input. It consists of an opto-isolating led in series with two 330Ω resistors. The input logic levels for the PP880 are defined as 0V to 1V for a logic low and 5V to 12V for a logic high. When an external trigger is applied, all eight channels will be pulsed simultaneously.

3.3.2 Variations in triggering

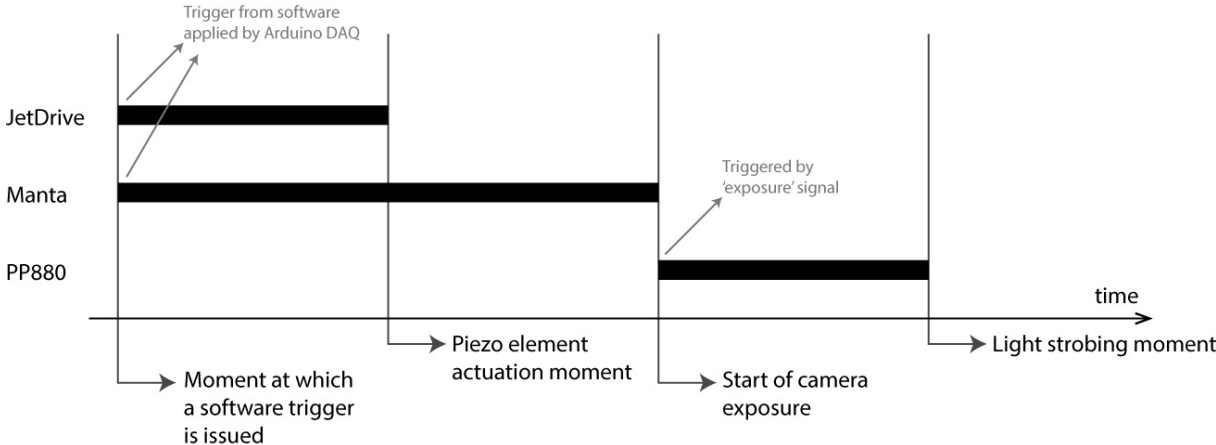
Three manners in which triggering can be implemented will now be looked into. A first way of making every single component active at its respective time is by first programming each with its own delay time and then triggering them all at once. After this master trigger is applied to all devices at once, every device will wait by itself for an internal timer (depicted below by a horizontal black bar) to reach its preset value. When this value is reached, the device will become active. This is the most simple case to implement as all three devices will be driven by the same signal. In usage it however is not practical. The camera and strobe for instance always need to be synchronized to each other. Because if the camera's delay needs to be increased by a certain amount, the strobe controller's should be adjusted with the same amount.



Graph 3-1: Triggering configuration 1 - all at once

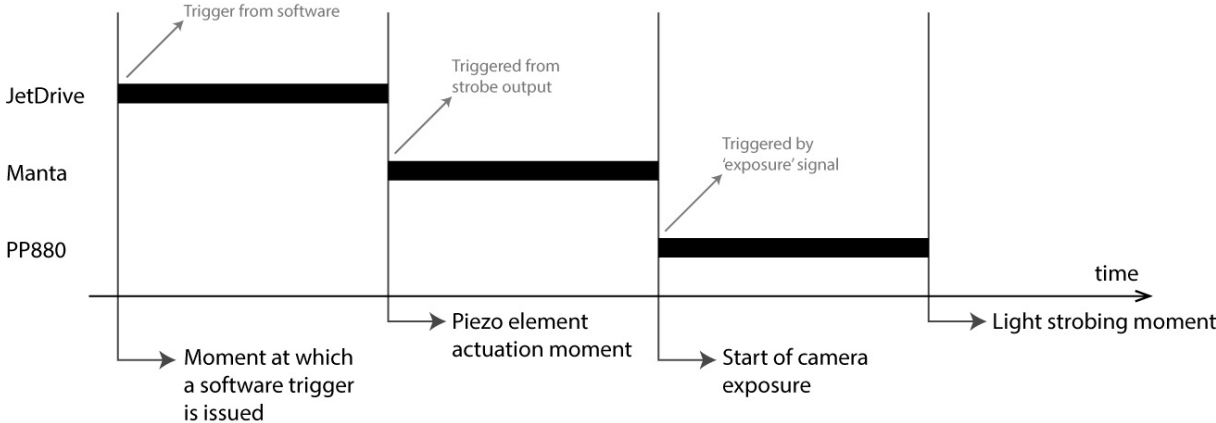
This brings us to the second implementation. The strobe controller's external trigger input is now connected to the camera's general purpose output, making them inherently synchronized. The series of events now are as follows: first both the ink jet drive electronics and camera are triggered while, upon becoming active itself, the camera triggers the strobe controller. The Manta camera is very versatile in this aspect as it allows the designer to chose which internal signal is presented at the output. A custom

signal can even be made by using an internal signal and delaying it. In the camera this custom internal signal is called the 'strobe'. Another prominent internal signal is the 'exposure' signal which is driven high while the camera is exposing. For building a custom 'strobe' signal, the 'exposure' signal was chosen and delayed for 5 μ s. This method is less influenced by timing jitter. When the camera's active moment shifts due to timing jitter, the strobes active moment shifts with it.



Graph 3-2: Triggering configuration 2 - strobe synced to camera

The timing of the imaging moment relative to the driving signal output is now adjusted as a camera parameter. Another option is also possible by triggering the camera from the strobe output of the ink jet drive electronics. Now the master trigger coming from control software initiates a domino effect by first triggering the drive electronics, who then after a certain delay triggers the camera which by itself triggers the strobe controller after 5 μ s. Because the delay of the strobe output on the drive electronics is more easily adjusted than the external trigger delay of the camera, this method is preferred.



Graph 3-3: Triggering configuration 3 - domino effect

A small downside to it however resides in the fact that the intrinsic delays from both the driving electronics strobe output and the camera input are now added up. This makes it impossible to do

inspection of the nozzle at a moment earlier than the sum of their intrinsic delay values in reference to input trigger moment of the ink jet driving electronics. By chaining the elements one after another, their timing jitter uncertainties will also add up. The last device in this chain will suffer the most of it: the strobe controller's output pulse moment can vary because of its own timing jitter, the camera's or the jitter of the ink jet drive electronics.

3.4 System operation verification

After building this system, further efforts were needed to verify its operation precisely.

3.4.1 Strobe light output

Being the single most important part of a flash photography system, the led's operation was checked. Measurements had to be made to inspect if the light source output reflected its driving pulse timing precisely and to observe changes in light output with different pulse amplitudes.

Intensity measurements

First of all the intensity was inspected while the light source continuously emitted light. Later on the same was done for strobed light. For both cases, deductions were made based upon camera images. Since the light source always functions as a backlight to the object under inspection, this means the light beam was pointed directly into the camera. To monitor possible led degradation from high pulsed currents, reference images were frequently made from continuous light at reference power.

Timing measurements

At least as important as its intensity in this setup is the light pulse's timing. Verification of the driving pulse was done directly by probing it with a Tektronix TDS 1002B digital oscilloscope across the drive signal leads. Since inspection should be done on a single pulse, the oscilloscope is operated in 'single shot' mode. Only conclusions for the input of the light source could be drawn from these measurements. Direct insights into possible delays between applying the drive signal and effective light output could not be gathered. Because of the very short pulse length, it was even not always possible with the naked eye to detect if light was being outputted at all. Direct optical measurements were then looked into.

Calibrated photodiode

First a calibrated silicon photodiode was borrowed from the *laser research department*. It consisted of a metal enclosure with a small window and BNC connector. After soldering a BNC connector breakout, the photodiode was then directly connected to the oscilloscope leads. To capture as much light as possible, it is placed directly in front of the light source. Its output signals typically lie within the millivolt range.

Small Si solar cell

As the noise levels of the Tektronix TDS 1002B also lie within the millivolt range, another approach was tried for detecting light pulses. A small mono crystalline silicon solar cell had been equipped with leads and attached to an acrylic base plate. This solar cell maintains a voltage of maximum .5V at 500mA. Again in order to capture as many light as possible, the solar cell was placed directly in front of the light source.

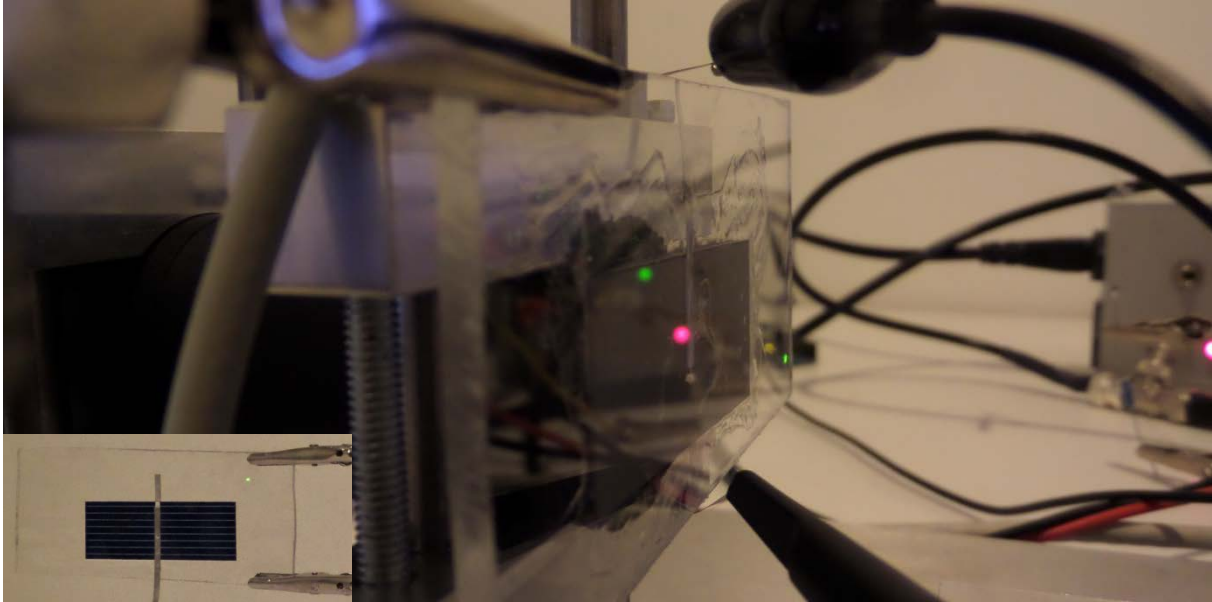


Figure 3-16: Placement of the PV cell in front of light source - PV cell detail in inlay

Its intrinsic reaction time is unknown but as it essentially is a large photodiode, this should be around the same order of magnitude as the previously inspected photodiode. Photovoltaic cells are however known for their relatively large capacitance, which will result in RC discharging behavior at its falling edge. To limit this behavior, a 1Ω load was placed over the PV cell's terminals.

3.4.2 Individual component input-output delay

Because a time critical hardware delay chain was made in this setup, intrinsic delay measurements should also be made for each component individually. By programming no added delay in the component and observing the ingoing trigger pulse along with the component's output, this delay was measured on the oscilloscope. Precise values are taken from the built in 'cursor' option of the TDS 1002B. Timing jitter is also inherently present, influencing the measured delay. To account for this, a range of 40 input-output delay measurements was taken for each individual device. After applying statistics, a value for the delay could be concluded along with an order of magnitude for the timing jitter. An Arduino UNO was configured as data acquisition (DAQ) device for LabVIEW. From a command in the software, a trigger was sent from the Arduino to the tested device's trigger input.

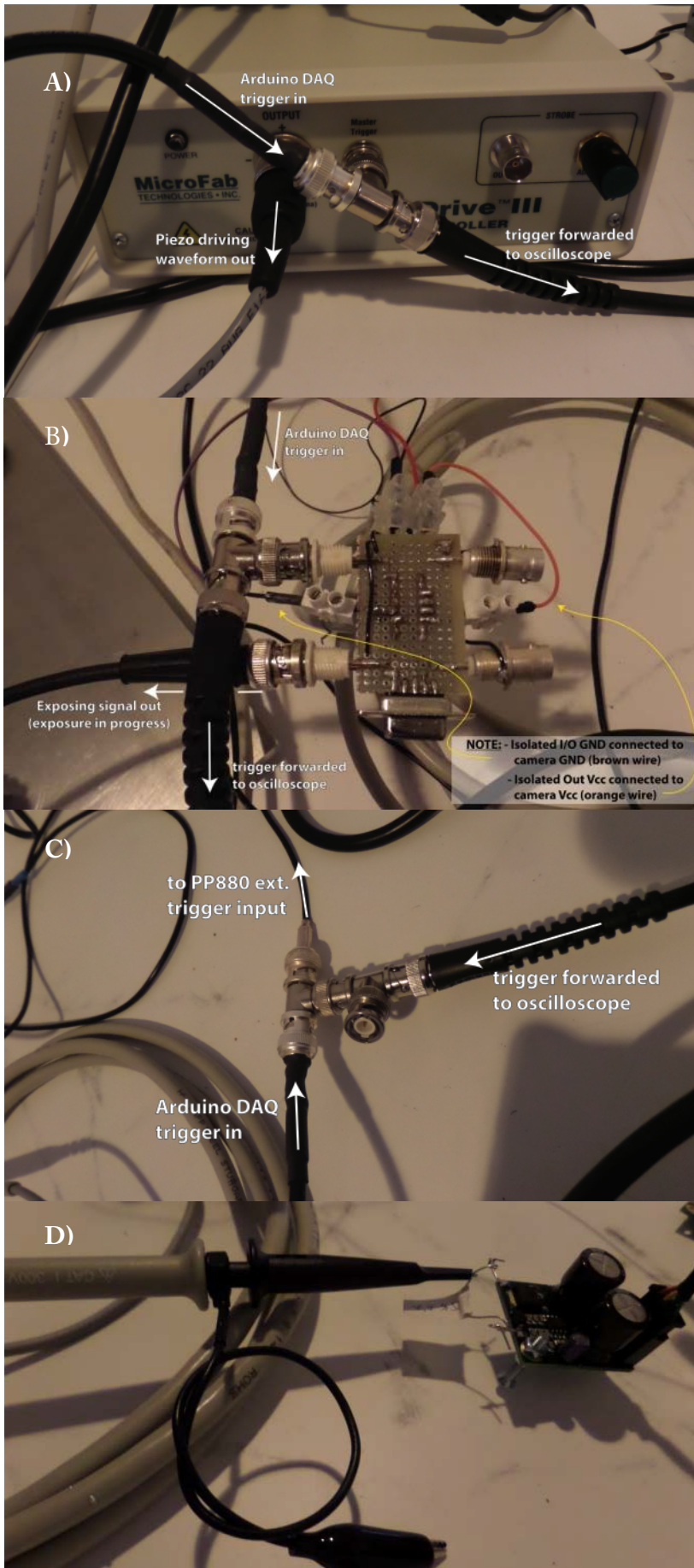


Figure 3-17:
 Delay measurements wiring
 for JetDrive (A),
 Manta (B)
 and PP880 (C)
 along with oscilloscope
 connection to the strobe
 controller driver module with
 dummy load (D)

4. Measurements and results

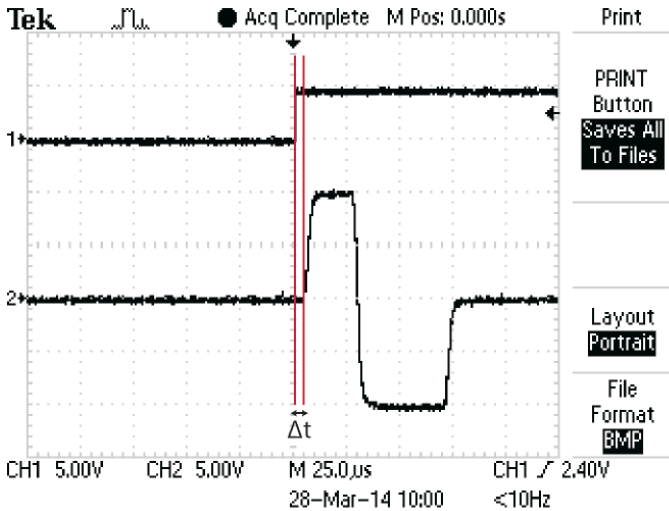
4.1 Delay measurements

Delay measurements were performed on every device to map their possible intrinsic timing delay and timing jitter. These values are of uttermost importance to account for when determining at which instance relative to the driving waveform an image was made. Values for timing jitter moreover are needed to determine the error margin of a drop speed calculation. In this subsection measurement results and their statistical processing are presented for the input-output delays of ink jet drive electronics, camera and strobe controller. This processing is done as follows: Outliers were defined as values lying more than 1.5 times the interquartile range (IQR) below or above respectively the lower and upper quartile. After removing the outliers, a mean and standard deviation was calculated and subjected to a few presumptions. First of all it was presumed that each measured delay variable followed the normal distribution. Second, from having a relatively large number of data points (40) it was presumed that the calculated mean and standard deviation represent those of the population.

4.1.1 Jet Drive III ink jet drive electronics

The measurements table which can be found in appendix A represents the time interval in μs between the external triggering moment and the leading edge of the bipolar driving waveform from the JetDrive. The left column denotes the order in which each measurement was taken. The right column the time interval in microseconds.

Each of these measurements are based on the following signal comparison:



Graph 4-1: Scope image of delay between trigger input and waveform output

All measurements were made using $1.00\mu\text{s}$ per division on the time scale as opposed to the 25 times less precise time scale used in the above overview screen.

Statistics were then applied to these measurements. After removing the outliers, a mean as well as standard deviation were calculated from the remaining dataset. Their values are as follows (in μs):

Table 4-1: Statistic results of JetDrive III delay measurements

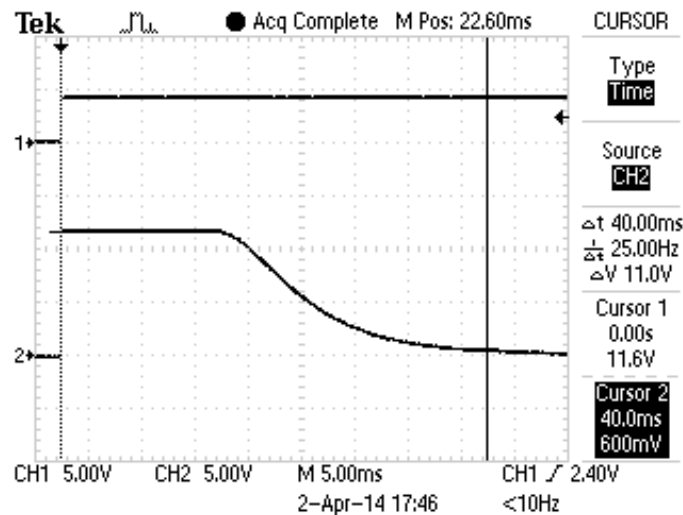
mean	4,171
std dev.	0,287

Following from the measured values as presumed to reflect the population, it can be said with a 95% certainty that the intrinsic delay of the JetDrive III at any given instant lies within the range of $3.597\mu\text{s}$ up to $4.745\mu\text{s}$. This corresponds to a mean value of $4.171\mu\text{s}$ with $\pm 0.574\mu\text{s}$ timing jitter.

4.1.2 Manta G-125B camera

The same kind of delay measurements were made for the camera's I/O delay behavior. This resulted in the dataset as depicted in appendix B. The left column again denotes the measurement's sequence number while the right column represents the measured intrinsic delay in microseconds.

Measurements were made of the time interval between the leading edge of the trigger input and the leading edge of the 'exposure' signal at the camera output. The general signal shapes are as follows:



Graph 4-2: Scope image of delay between trigger input and 'exposure' signal output

Even though it cannot be seen on this overview, a relatively large intrinsic delay is found between both signals. After removing outliers and calculating mean and standard deviation for the data sample, the following results were obtained (in μs).

Table 4-2: Statistic results of Manta G-125B delay measurements

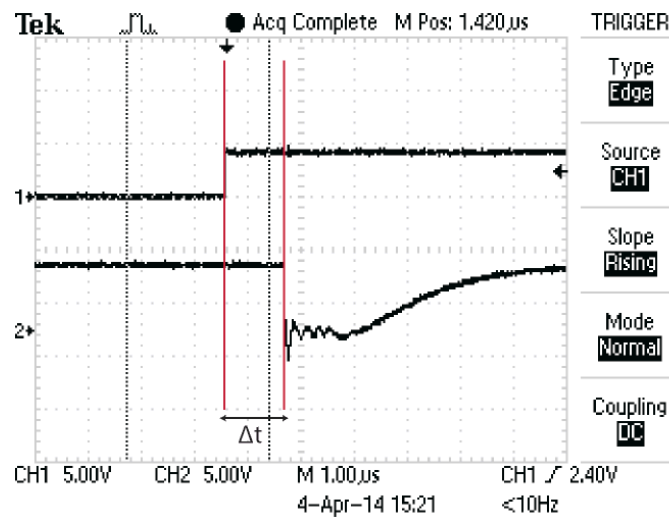
mean	9,803
std dev.	0,082

Under the same presumptions used for the ink jet drive electronics statistics, a 95% confidence interval for the camera delay is now found to range from 9.639 μ s to 9.967 μ s. This can also be interpreted as a mean value of 9.803 μ s with $\pm 0.164\mu$ s timing jitter.

4.1.3 PP880 strobe controller

Lastly, the same methodology was applied to the strobe controller. This time the time difference between the leading edge of the trigger input and the leading edge of the outgoing strobe pulse is measured. The results can be found in appendix C. The left column describes the order in which measurements were taken. The right column denotes the measured intrinsic delay in microseconds.

An overview of the signal shapes was also made. Note that for the strobe pulse signal a falling edge should be viewed. This is due to the fact that the driver module of the PP880 acts as an open drain output, effectively connecting the circuit to ground when activated. While not switched, the supply voltage will be measured at the terminals. The I/O delay behavior was measured using a relatively large (1.2k Ω) dummy load across the driver module's terminals. When combined with the open drain behavior, a fast discharging and slow charging of the measured node's capacitance is observed.



Graph 4-3: Scope image of delay between trigger input and light source drive pulse output

Outliers were removed from the data and the following values for mean and standard deviation were calculated (in μ s).

Table 4-3: Statistic results of PP880 delay measurements

mean	1,089
std dev.	0,029

While attaining the same presumptions as made earlier, the range from $1.031\mu\text{s}$ up to $1.147\mu\text{s}$ will contain all possible strobe pulse output delays with 95% certainty. An alternative representation for this delay is as a mean value of $1.089\mu\text{s}$ with a timing jitter of $\pm 0.058\mu\text{s}$.

4.2 Drop visualization

A few tuning and optimization steps have been performed before proceeding on to capturing images with a strobed backlight. Later on, when imaging with strobed backlight, two different light sources will be used. The steps listed below are found to contribute to the image quality of both options.

The first one of these steps was to manually locate the effective focal point. It was thereby found that very small changes in distance to the lens could result in tremendous improvements in image sharpness. Placing the nozzle in focus was however not possible at first. It could only be accurately brought into focus after adding adjustment screws which allowed sub-millimeter precision to the nozzle's optical axis slide mechanism. A tremendous improvement in accuracy was obtained by moving the nozzle less than a millimeter. The full printhead was then imaged by slightly tilting the lens and merging the resulting small partial images. It is good to have an idea of what the whole printhead looks like from the camera's standpoint. Based on this observation it would later on be easier to orientate oneself if the lens was tilted slightly and became misaligned. The composite image is shown below and gives a good overall impression of the imaging performance which can be achieved with the current setup.

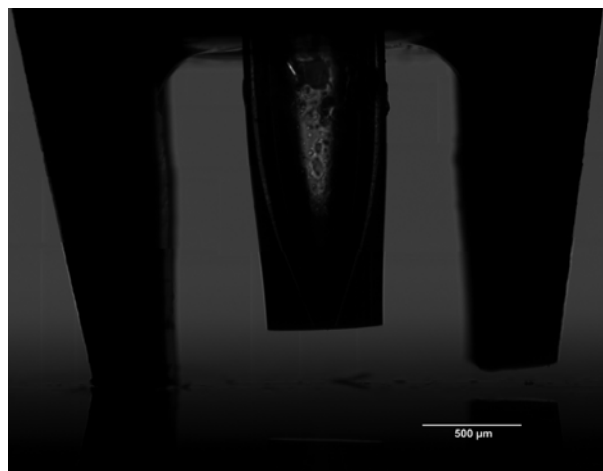


Figure 4-1: Composite overview of the nozzle from the camera's perspective

Later on, adaptations were made while moving on to strobed images. A strobe controller driver module was then connected to the backlight with a minimum connection distance to avoid large parasitic capacitances. Furthermore, the camera's exposure time was set at its minimum value of $21\mu\text{s}$ while the strobe controller pulse width was set to its maximum value of $5\mu\text{s}$.

A certain amount of light had to be collected during this $5\mu\text{s}$ interval to ensure a good contrast between object and background. Therefore the amplitude of the light source's driving pulse was increased stepwise while observing the intensity at the camera's image output. Correct signal synchronization was also constantly monitored for with the oscilloscope during these operations. A further improvement was then made by replacing the wirewound current limiting power resistor by its thin film counterpart. This was done because wirewound resistors essentially are coils of nichrome wire which can alter the transient behavior with their inductance.

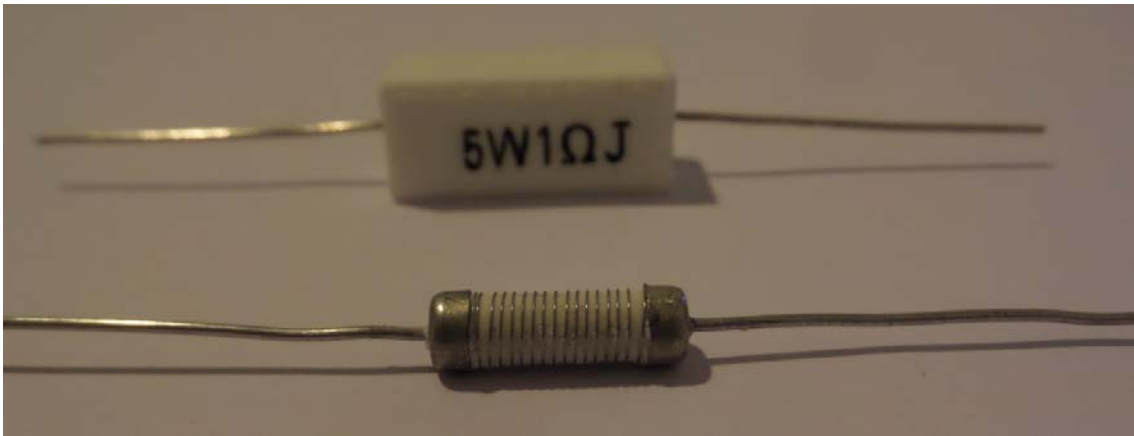


Figure 4-2: Exposed nichrome wire coil and normal wirewound resistor as reference

Ultimately, it was found that not the limiting of current to a safe level was difficult, but rather the increasing of light output to a significant amount. A lot of strobed imaging operations resulted in completely dark images, most remarkably so for the telecentric backlight. The setup was then fitted with a different power led, one which was readily available, to be able to quickly resume progress. This generic power led indeed was found to emit enough light to notably improve the image's intensity. It should however be driven at the highest pulse amplitudes, which cause the led light source to be stressed and degrade, in order to make clear differentiation between object and background possible.

A disadvantage of the generic power led lies in the fact that it also demonstrates resistive behavior. When increasing the voltage across both the led and the current limiting resistor, the voltage across the led did not remain constant but instead increased along with the applied voltage. The effect however was reversible, meaning that by lowering the voltage, the led voltage would also drop and the same expected image clarity was obtained as before. In hindsight, this added resistivity is attributed to degradation of the power led. Also, seeing this light source was not of the telecentric kind, static

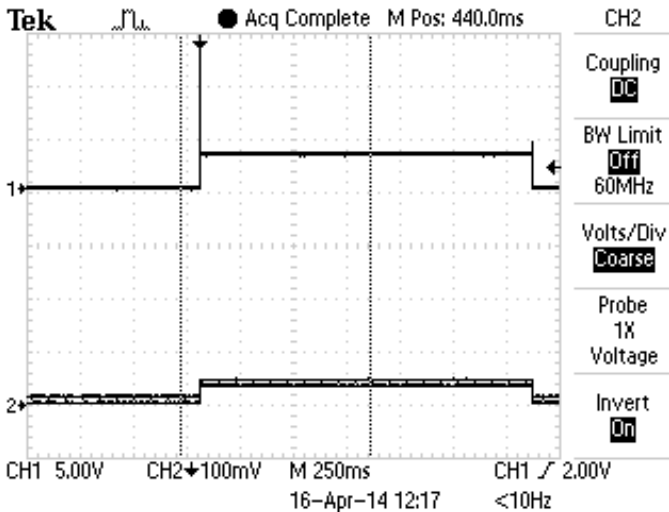
images of objects were made to compare its image quality. If the object was placed precisely at the lens's working distance, a clear image could be produced which was only slightly less sharp than with the telecentric backlight. This can presumably be credited to the fact that a telecentric lens is still being used.

The presence of an optical light pulse and its timing need to be verified at this point to further investigate the strobed imaging operation. The bottleneck for exposure time could even lie in the delay caused by the recombination time of electrons and holes in the led. This verification process is explained in the following two subsections.

4.2.1 Telecentric backlight

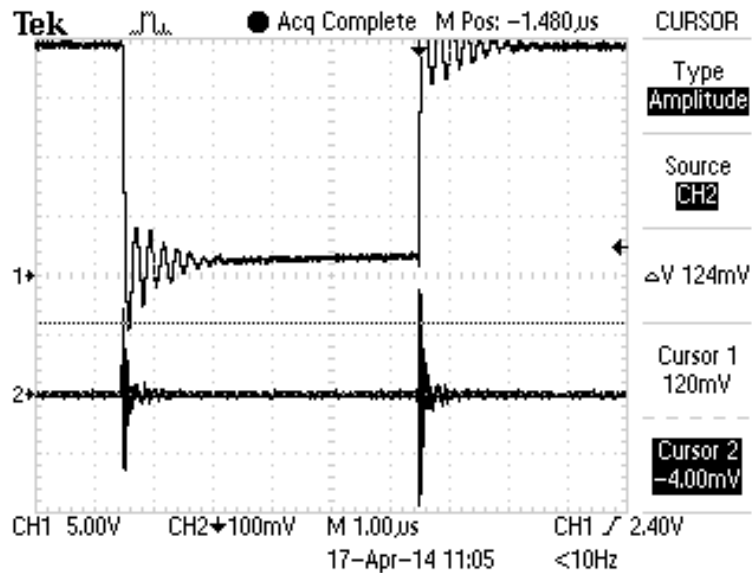
Crude optical output measurements were further performed to verify this light source's strobe light operation. For a first set of observations of the telecentric backlight, a calibrated silicon photodiode was connected to the oscilloscope. At the continuous reference light output, a signal of about 6mV was measured with very low signal to noise ratio (SNR). From strobed light operation a few measurements were made showing only spikes corresponding to the edges of the driving pulse. The signal in between the spikes however remained flat, indicating no light or not enough light reached the diode to produce a decent level of output. A remark was made for the first time that the spikes maybe resulted from RF interference and not from a light pulse.

To further inspect the optical output, measurements were also made by placing a PV cell directly in front of the lamp and connecting it to the oscilloscope. It was given a 1Ω load to reduce possible RC timing transients to a minimum. In response to continuous light a voltage level of about 50mV was measured across the terminals. Following this, strobed light operation was inspected in the same manner.



Graph 4-4: Scope image of optical response (CH2) on long >1s driving pulse

First a set of measurements was taken with no sign of any response when a drive pulse was applied. The current was increased up to 3.5A with no significant results. The lamp however still appeared to function when continuously driven at its 350mA reference current. After replacing the wire wound resistor with a thin film of the same value, the measurements were repeated with a higher precision on the time scale. A response was observed but just like with the photodiode, it was limited to spikes at the edges of the driving pulse.

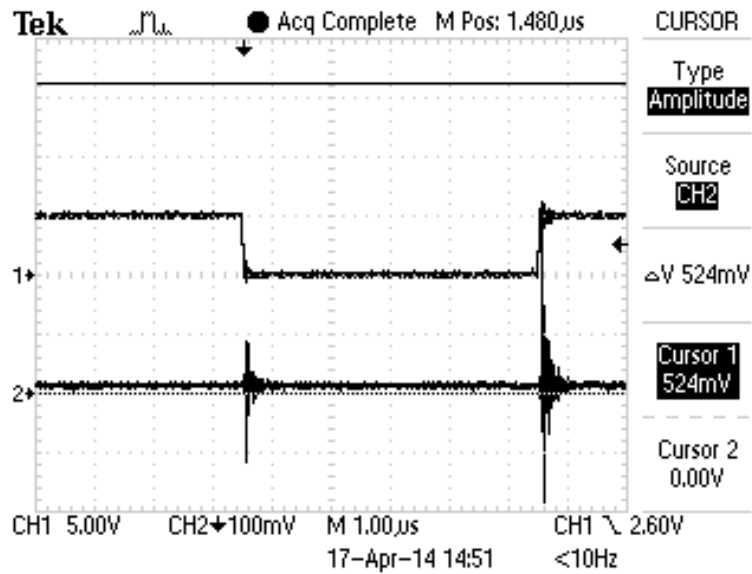


Graph 4-5: Scope image of optical response (CH2) on short 5µs driving pulse

These observations again rather pointed towards RF interference than to detection of effective light output. To rule out the first, a few alternative measurements were performed. Pulse widths of 1µs and 100ns were also used to inspect their influence on the output.

First a driver module was taken with only a dummy load (as was used for delay characterization). When pulsing this module with 1.2kΩ resistor at the highest amplitude, no response was observed in the PV cell signal. The same observation was made for a 5.6Ω resistor. Then the lamp was again pulsed at 20.75V with a current limiting resistor of 1Ω and calculated current of 17.5A. This time strong spikes were again found at the edges of the pulse. When the PV cell was put on the other side of the device, and hence out of the possible emitted light's path, spikes were still observed. After verifying the lamp still functioned in continuous mode, pulse width was again adjusted to 5µs for final measurements. When putting the PV cell directly in front of the light source, spikes were again observed.

For a last measurement, the cell was now put directly above the lamp to be sure it would definitely receive no light from it at all. Spikes were still observed.

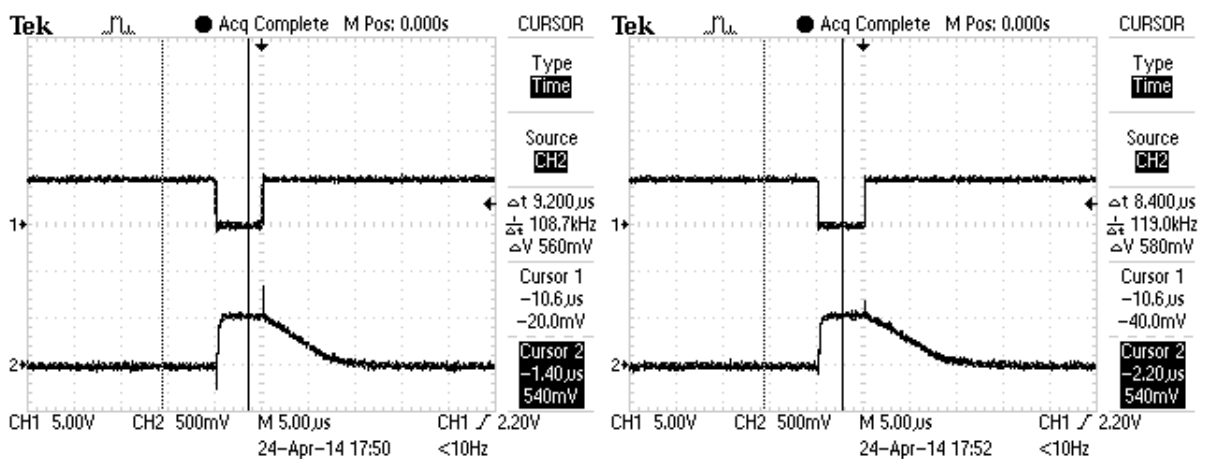


Graph 4-6: Scope image of optical response (CH2) measured above lamp

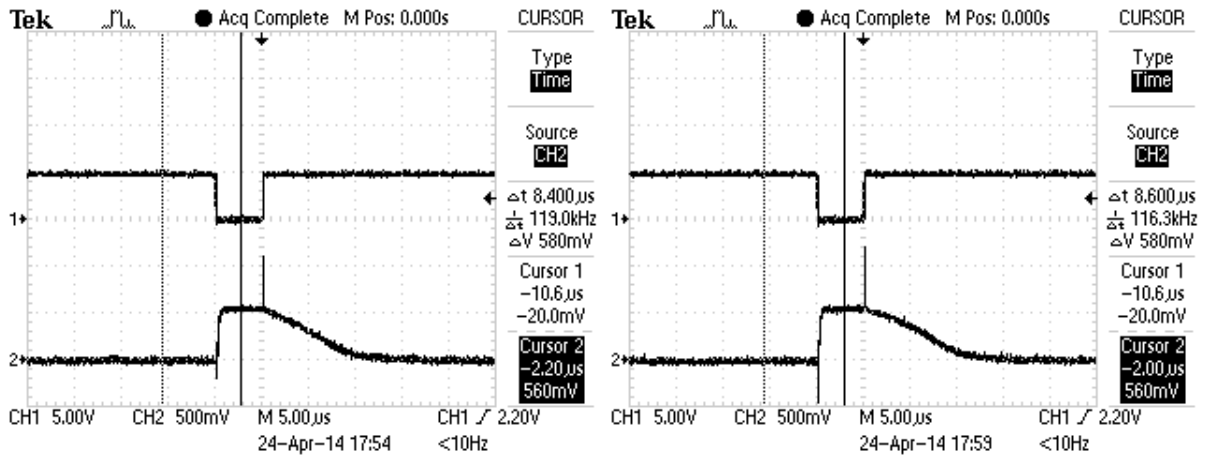
This served as conclusive evidence that all measurements just represented RF interference. When driven in strobed operation, the telecentric lamp simply would not emit any light. The light can therefore not be of further use in the setup and was not used in strobed operation to image falling droplets.

4.2.2 Generic power led

Measurements were once again taken from the light source's optical output with the same PV cell while monitoring with the oscilloscope. Pulse amplitudes of 28, 32, 36 and 40V were used.



Graph 4-7: Scope images of optical response on 28V (left) and 32V (right) pulse amplitudes



Graph 4-8: Scope images of optical response on 34V (left) and 36V (right) pulse amplitudes

Based on the oscilloscope images, it can be found that the led certainly starts to emit light at about the same instant it gets a drive signal. Not much can be said about the end of the light output as it is uncertain if The gradual slope at the right side of the pulse shape is known to be caused both by the finite speed of charge carriers as they travel to led's pn junction to recombine as well as by capacitive behavior of the solar cell. A detailed distinction between each effect's contribution however cannot be made. The slope was observed to become less steep as more current was sent through the led, indicating the effect of the finite recombination speed.

Finally, after verifying the operation of each component on its own and under static conditions, dynamic images are now made from droplets being ejected from the ink jet nozzle with the generic power led. A 5µs strobe pulse duration was used during a 21µs camera exposure time. The bipolar driving waveform for the piezo ink jet nozzle had an amplitude of +20V to -20V, 3µs rise and fall time, 20µs dwell time, 40µs echo time and 3µs final rise time.

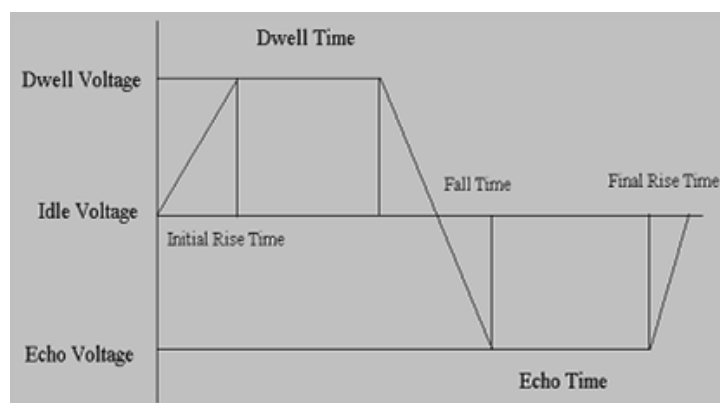


Figure 4-3: JetDrive III bipolar waveform parameters [44]

The solvent used was demineralized water. Relatively dark images were obtained because two out of the three on chip led rows of the generic power led had been burned through. An image is supplied below to give an idea of the original image clarity.

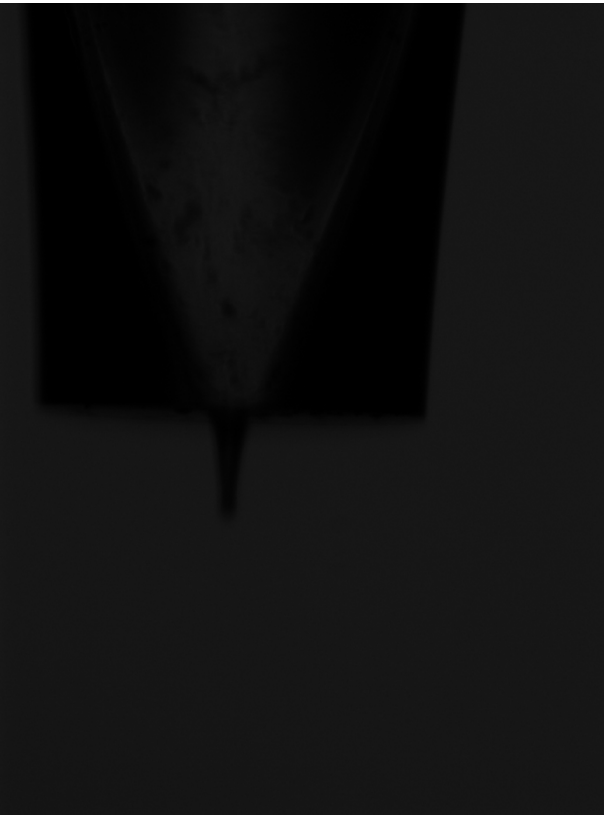


Figure 4-4: Original image as obtained with the developed vision system and generic power led

As can be observed, the contrast between object and background in the image was sufficient to be able to perform measurements. For further presentation and processing however, all images were also thresholded. Eventually, an impression of drop formation was successfully captured as a sequence of images from different droplets at successively larger delays from the nozzle actuation moment. A selection of drop formation stages for a single printhead configuration are depicted below in a series of thresholded images from the vision system.

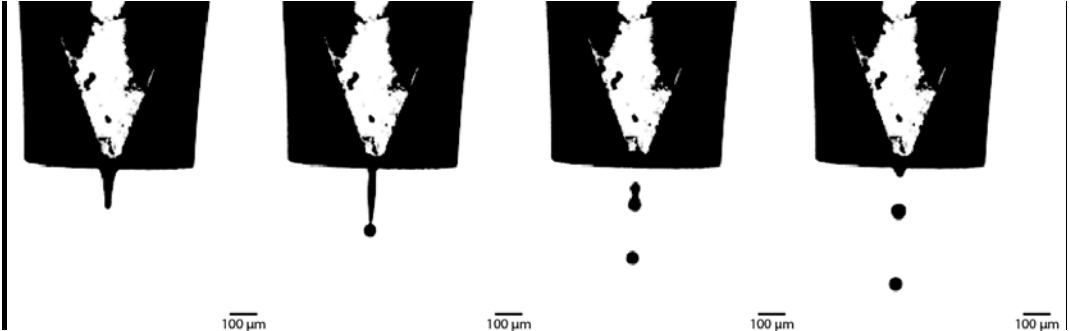


Figure 4-5: Imaged drop formation at 30μs, 60μs, 90μs and 125μs

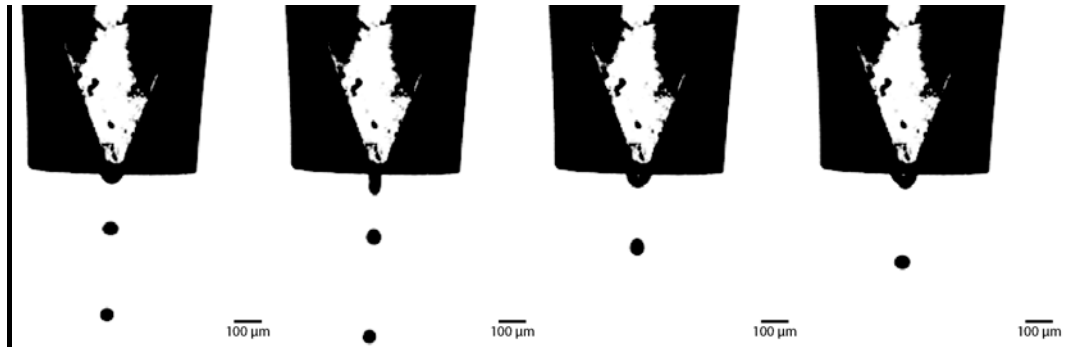


Figure 4-6: Imaged drop formation at 155 μ s, 180 μ s, 210 μ s and 255 μ s

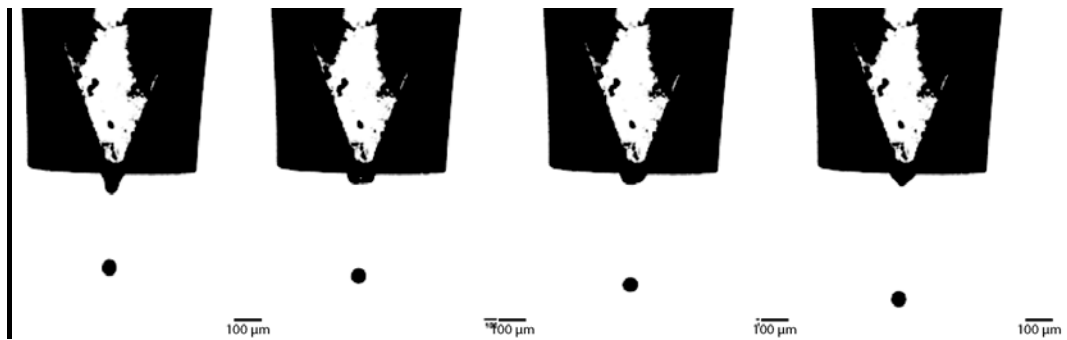


Figure 4-7: Imaged drop formation at 275 μ s, 300 μ s, 325 μ s and 370 μ s

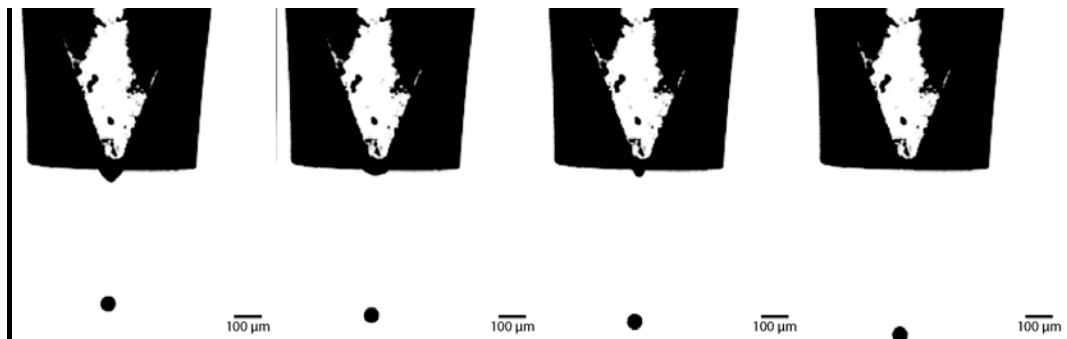


Figure 4-8: Imaged drop formation at 295 μ s, 430 μ s, 450 μ s and 485 μ s

In total, over 100 images were captured of the drop formation process. These ranged from a delay of 30 μ s to nozzle actuation to a delay of 540 μ s with steps between images of 5 μ s. It was found that this specific drop formation showed occurrence of a fast satellite, travelling in front of the main droplet at higher speeds. Since sufficient quality has now been obtained, further efforts can be put into characterizing the resulting drop by means of images taken of its drop formation process.

4.3 Drop characterization

'ImageJ' image processing freeware is now used to determine the drop size and speed. Since it is easier to determine 2D area of the imaged drop than it is to determine drop diameter, the diameter will be derived from the area by presuming a perfect circle. A first set of measurements will be done based on the image at 180 μ s. Its binary version can be found below. As was concluded from the long sequence of images which were depicted earlier, the inspected drop formation includes a fast satellite which travels at higher speeds in front of the main droplet. The main droplet is typically larger and slower when compared to its corresponding fast satellite.



Figure 4-9: Imaged drop formation at 180 μ s

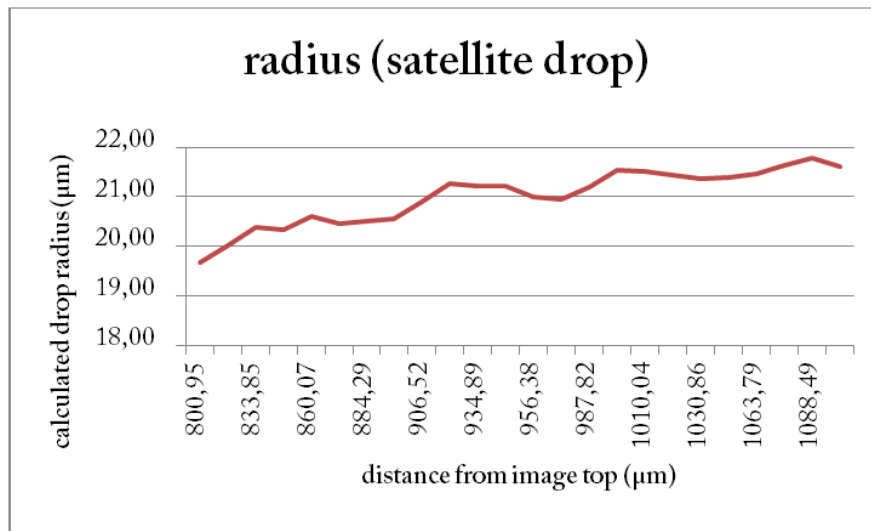
According to ImageJ, the top droplet's area contains 2268.7 pixels, the bottom's 1780.3 pixels. When considering the fact that each square pixel corresponds to a width and height of 0.9375 μ m, each pixel is found to match an area of 0,8789 μ m². The top droplet's area thus measures 1994.0 μ m² and the bottom one 1564.7 μ m². If both were imaged as ideal circles, their respective radii would be 25.2 μ m and 22.3 μ m. If a further assumption is then made that both are perfect spheres, their respective volumes would be 66980 μ m³ and 46560 μ m³ or 66.98pl and 46.56pl.

When this reasoning is now further applied to all images which were taken along the droplets path, a better founded estimate can be made of the effective droplet's radius and volume, along with its speed. Out of the 103 images taken, the satellite drop was depicted on 24 images. Possibly along with the satellite drop, 78 images furthermore showed the main droplet.

First of all all images went through a similar procedure as was illustrated for the single image above. The only addition now is that the xy coordinates of the centre of mass are now also measured in

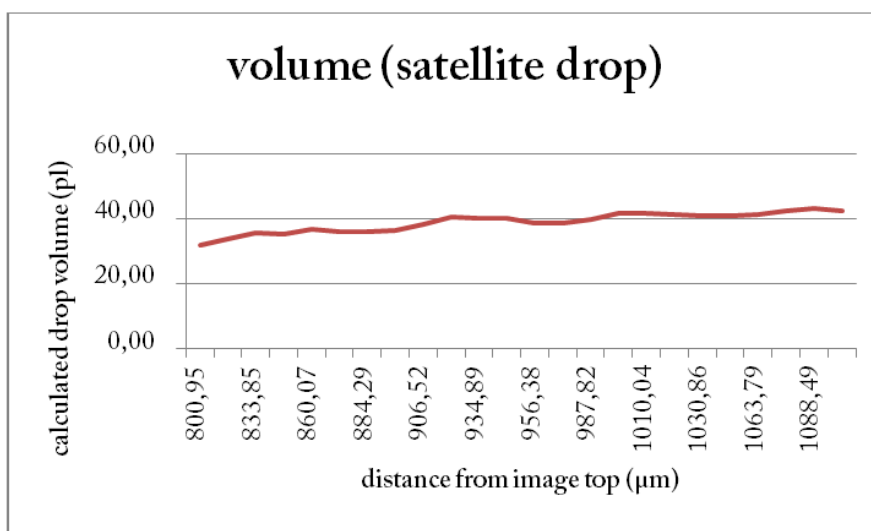
ImageJ along with the area and converted from pixel units into respectively μm and μm^2 . From the area, again a radius and volume is calculated while assuming perfect spheres. The y coordinate (in μm) of subsequent images is subtracted from each other and divided by $5\mu\text{s}$ (time between images) to obtain the average velocity during the time interval between both images. This will be taken as an estimate of the *instantaneous drop speed* in the image. By plotting each of these calculated variables against the corresponding y center of mass coordinate at which they were found, a visual representation was made.

These visual representations shall now first be discussed for the satellite droplet.



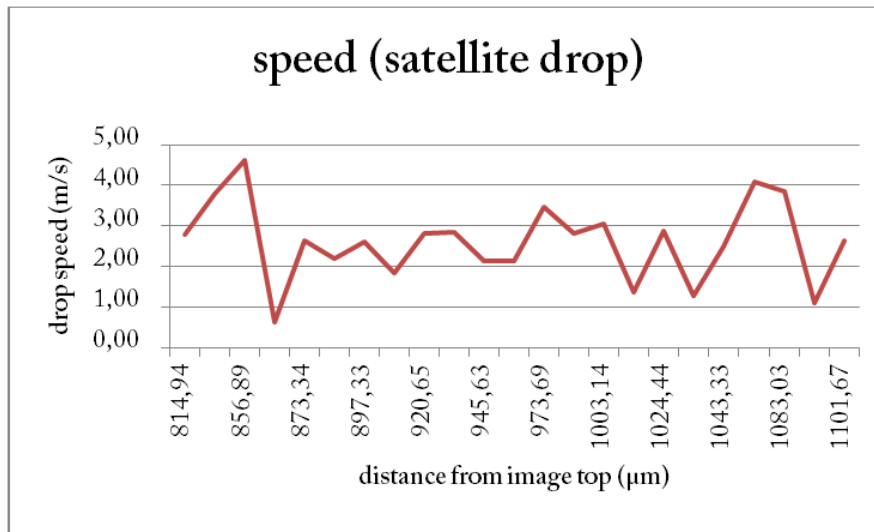
Graph 4-9: Satellite drop radius as a function of distance

No large variations are seen in the drop radius, but nevertheless a positive going trend is observed. Measurements lie between $19.68\mu\text{m}$ and $21.77\mu\text{m}$, with an average of $21.00\mu\text{m}$.



Graph 4-10: Satellite drop volume as a function of distance

The same observations apply to the droplet volume, since it is mathematically derived from the drop radius depicted above. Measurements range from 31.92pl to 43.24pl, with an average of 38.86pl.



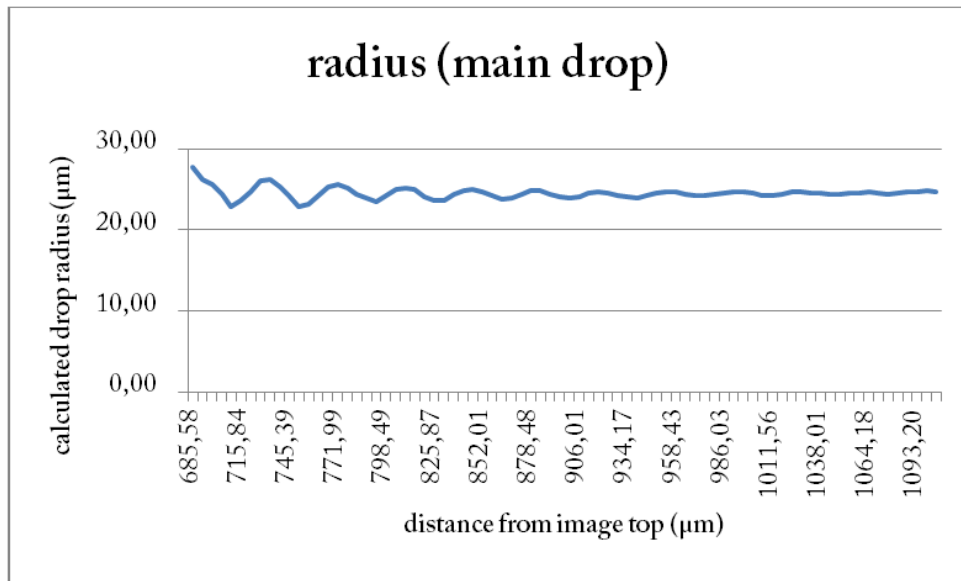
Graph 4-11: Satellite drop speed as a function of distance

The satellite drop speed does show significant variations. Peak calculated values lie as high as 4.61m/s and as low as 0,64m/s, with an average of 2.61m/s. The largest changes in value are more or less situated right after break off and just before reaching the substrate.

The notable positive trend in both drop radius and volume could possibly be declared by expansion of the ink's volume as its pressure drops from the level applied to it at ejection to the ambient pressure of its surroundings. Another possibility, however more unlikely, would be that the droplet is a perfect sphere at the beginning. This means it has a minimal surface area for a given volume. On its way to the substrate the droplet would then deviate more and more of the perfect sphere, giving it a larger surface area for the same volume. As the current processing algorithm uses a 2D projection of the surface area to determine radius and volume, this series of events could also lead to the recording of a positive going trend like the one which was noted in the graph.

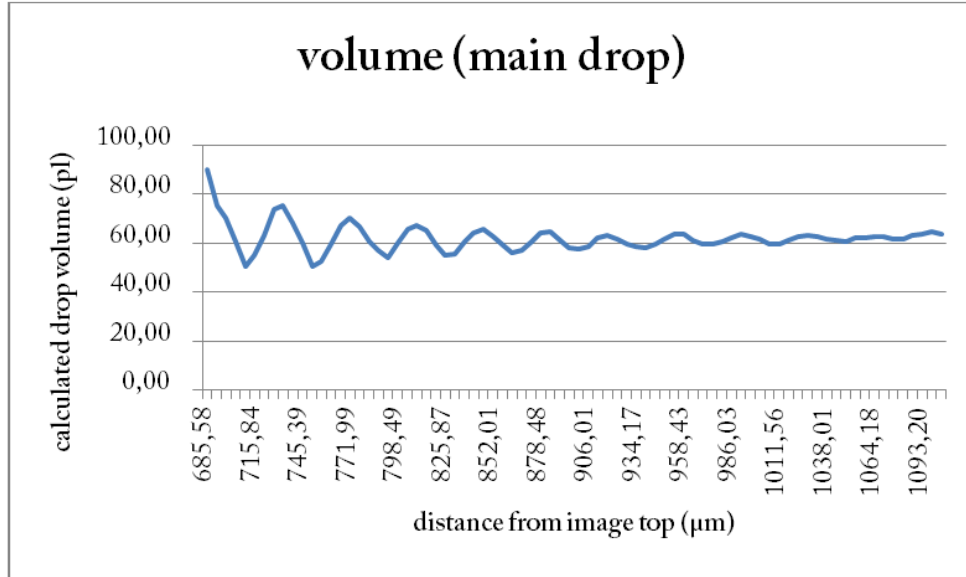
The drop speed on the other hand demonstrates an evolution which is more peculiar and difficult to explain. The alternating acceleration and deceleration do remind of an accordion or caterpillar like movement by which the front end first moves forward, then waits for the back end, then moves forward, waits again, ... Variations of the position of centre of mass within the droplet coming from deformation of the drop shape could cause our observation of this effect. No notable periodical deformation was however observed. A conclusive logical explanation thus was not found. Edge effects of the surrounding air current at nozzle and substrate could possibly lie at the base of the large variations at the beginning and ending of the graph.

Subsequently, let us direct attention to the corresponding graphs for the main droplet. Since more measurements (images) were made of the droplet in flight, more detail is expected to be found.



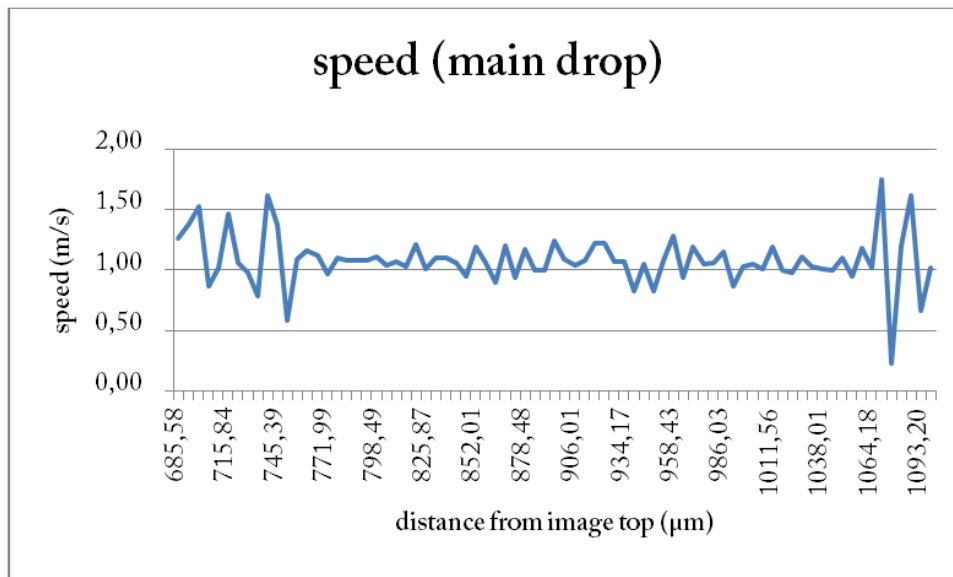
Graph 4-12: Main drop radius as a function of distance

The main drop's calculated radius clearly shows the behavior of a damped oscillation. Measurements now range from 27.78µm to 22.90µm with a mean of 25.86µm.



Graph 4-13: Main drop volume as a function of distance

Since the calculated volume is again derived from the radius, it also shows a damped oscillating behavior. Calculated volumes reach as high as 89.92pl and as low as 50.31pl, with an average value of 65.36pl.



Graph 4-14: Main drop speed as a function of distance

The main droplet moves a lot slower than the satellite drop. Its highest peak value lies at 1.75m/s while its slowest measurement comes in at 0.23m/s. The average drop speed of the main droplet is 1.08m/s, which is less than half of the satellite drop's average speed. This time, the largest deviations in drop speed are more clearly found to be situated at the beginning and ending of the graph.

First of all, a very logical explanation can be formed to declare the oscillations in the main drop's radius and volume graphs. They are caused by obvious mechanical oscillations within the droplet itself, as can be observed with the naked eye from the sequence of images captured with the vision system. The oscillations cause the shape of the droplet to deform periodically. When remembering that the radius is calculated from the area of a 2D projection of this shape, the relation between both is directly found. Every oscillation consists of a positive and negative deviation to the perfect spherical shape when only considering its 2D projection. The mean value however should not be used to represent the actual drop volume and corresponding radius in a perfect sphere, since it will not correspond to the properties of the droplet at rest. Instead, a value should be picked at the moment when the oscillation is as much damped as possible to represent the droplets steady state value. So instead of the respective means of radius and volume of 25.86μm and 65.36pl calculated from all values, the values at the end of the graph should be considered more: 24.54μm and 61.94pl are found by averaging only the last 20 measurements of both radius and volume.

The curious behavior of the drop speed measurements is found in more detail due to the higher amount of measurements. Variations of the y coordinate of the centre of mass, coming from the oscillating deformation, can lie at the root of these observations because the speed is calculated from the difference in vertical position. This would however imply that the damped oscillating behavior should also be observed in the drop speed graph, which is not (directly) the case. Again, larger swings

in drop speed are found just after leaving the nozzle and just before the substrate. The variations at the nozzle could potentially be declared by the large oscillations at those positions, but these oscillations are long gone when the droplet reaches the substrate and its drop speed starts to swing again.

When comparing the measurements of the satellite drop to those of the main drop, a first difference can be found in the level of detail which is found in the graphs. Because the satellite drop only appears in 24 images, its data resolution is much lower in comparison to that of the main drop. Oscillations could only be clearly observed in the radius and volume graphs of the main drop but possibly they were also present in the satellite drop and masked by its low amount of measurements. A similarity between both however lies in the fact that the drop speed of each displays its largest variances at measuring points close to the nozzle and substrate. Direct plausible explanations were not found for this, however the hypothesis of deviating air currents (turbulence) at either end still stands until corrected.

5. Discussion and conclusion

The main objective of this thesis was to build a vision system which is capable of imaging ink jet droplets along their path from nozzle to substrate. Its purpose lies in the fact that it should be used to characterize newly developed functional inks in order to precisely match them with an appropriate waveform for ultimate accuracy in drop-on-demand inkjet printing.

An extensive literature study was performed at the beginning of this master's thesis. In a first section, all different variants of ink jet printing were discussed along with entire commercial functional inkjet systems as well as separately available components and custom built solutions. These systems later served as models to compare the developed system to. Upper and lower boundaries on respectively drop speed and drop diameter were also obtained from literature as referential circumstances to keep in mind with system design. The different stages of drop formation and its many influencing parameters were also comprehensively studied as a basis for intended waveform optimization. A lot of side effects were also found to occur. Luckily, all of these could be omitted by adapting the nozzle's driving signal. Besides this, the machine vision domain was also explored. The five fundamental parameters were discussed as well as the three main components: lens, lighting and camera. Different options and configurations were looked into and compared to each other in preparation of material selection.

After this theoretical approach, practical choices were presented in terms of methods and components by which functional droplets should be jetted and inspected. A vision system with telecentric backlight and lens was built around a drop-on-demand inkjet nozzle with large orifice. Theoretically, a sub-micrometer pixel precision was obtained in the spatial domain with almost no edge uncertainty, while the time domain features a sub-microsecond exposure time. Backlight options included a telecentric backlight, generic power led and high performance Cree led. Further considerations were also made regarding triggering implementation, where a domino effect was preferred, and regarding possible ways to verify correct functioning of the system, where measurements of light output as well as input-output delay were proposed.

These input-output delays for each component were then statistically derived from sets of measurements to serve as an indication of the timing precision of falling droplet images. The greatest intrinsic delay was found at the camera, while the greatest variation occurred at the ink jet drive electronics. Timing jitter was practically defined to be less than $1\mu\text{s}$ for each component. Further measurements hereafter included drop visualization. First, a few optimization steps were presented along with a high resolution composite image of the nozzle as viewed by the vision system. Next, adaptations were applied to facilitate the transient behavior of the light source's driving pulse. Optical verification measurements of the telecentric backlight were then performed. By placing the

measuring solar cell above the lamp, spikes were then ruled out to originate from emitted light and attributed to RF interference. The telecentric lamp was therefore concluded to emit no light under pulsed operation and replaced by the generic power led for which viable response was indeed found. A drop formation was subsequently imaged with the generic power led at intervals of five microseconds and further processed with ImageJ. Conclusive indications were given of the imaged droplet's radius, volume and speed, as well as of how these parameters varied along its path between nozzle and substrate. Oscillations in the main droplet were noted and mapped with the vision system and subsequent image processing. A phenomenon was also observed in which the drop speed would swing significantly stronger when close to either the nozzle or the substrate and a hypothesis was formulated in which this was caused by deviating air currents at either end.

In conclusion, this master's thesis has successfully reached its goals of developing a vision system for drop formation and obtaining a vast understanding of possible influences on the drop formation process. The characterization of a series of untested inks as well as an optimization of the driving waveform according to these characteristics however have not been fully performed and are kept for future elaborations. Furthermore, a first upgrade to the system should be replacing the generic power led by the characterized Cree led light with higher lumen output per watt. It is expected to result in shorter possible exposure times which still yield useful images. Apart from this, the image processing which was now performed semi-automatically with ImageJ should in the future be fully automated within LabView and integrated into the setup's current control program. Lastly, automatic or semi-automatic waveform optimization would be an extremely valuable tool for the functional inkjet printing industry and should certainly be further looked into. This dissertation can then be used as a useful starting point in understanding how drop formation can be influenced and which side effects can occur. Essentially, the waveform should be designed to cause stable drop formation without side effects. Since these requirements can all be visually inspected, the design of this waveform can be performed by adding intelligence to the vision system. A first approach would be to let the setup run overnight and try every possible combination of parameters. In a second stage, drop formation theory should then be converted into a set of guidelines by which the computer can narrow down its search intervals. Good insight from practical experience with waveform tuning would be a key asset in this endeavor.

6. Literature

- [1] H. Dong, W. W. Carr, and J. F. Morris, "Visualization of drop-on-demand inkjet: Drop formation and deposition," *Rev. Sci. Instrum.*, vol. 77, no. 8, p. 085101, 2006.
- [2] G. D. Martin, S. D. Hoath, and I. M. Hutchings, "Inkjet printing - the physics of manipulating liquid jets and drops," *J. Phys. Conf. Ser.*, vol. 105, p. 012001, Mar. 2008.
- [3] Y.-M. Kim, S.-U. Son, J.-Y. Choi, D.-Y. Byun, and S.-H. Lee, "Design and Fabrication of Electrostatic Inkjet Head using Silicon Micromachining Technology," *JSTSJournal Semicond. Technol. Sci.*, vol. 8, no. 2, pp. 121–127, Jun. 2008.
- [4] P. Calvert, "Inkjet Printing for Materials and Devices," *Chem. Mater.*, vol. 13, no. 10, pp. 3299–3305, Oct. 2001.
- [5] Optomec, "AerosolJet 300 datasheet." [Online]. Available: http://www.optomec.com/downloads/Optomec_AerosolJet_DataSheet.pdf.
- [6] Roth & Rau B.V., "PiXDRO LP50." [Online]. Available: http://www.roth-rau.de/konzern/roth/container/downloads/produkte/FactSheet_PiXDRO_LP50.pdf.
- [7] Fujifilm USA, "Dimatix Materials Printer DMP-2831." [Online]. Available: <http://www.fujifilmusa.com/shared/bin/PDS00085-DMP2831.pdf>.
- [8] Microfab Technologies, "Jetlab 4 spec sheet." [Online]. Available: http://www.microfab.com/images/pdfs/v.4/jetlab4_specs_mf5.pdf.
- [9] Microdrop Technologies, "Microdispenser System , MD-E-3000," 2010. [Online]. Available: http://www.microdrop.de/Electronics.html?file=t1_files/Download_PDF/Microdrop_System_1210.pdf.
- [10] Microfab Technologies, "JetDrive III Drive Electronics," 2013. [Online]. Available: http://www.microfab.com/images/pdfs/v.4/jetdrive3_mf5.pdf.
- [11] S. D. Hoath, S. Jung, W.-K. Hsiao, and I. M. Hutchings, "How PEDOT:PSS solutions produce satellite-free inkjets," *Org. Electron.*, vol. 13, no. 12, pp. 3259–3262, Dec. 2012.

- [12] J. Stringer and B. Derby, "Limits to feature size and resolution in ink jet printing," *J. Eur. Ceram. Soc.*, vol. 29, no. 5, pp. 913–918, Mar. 2009.
- [13] M. Vilardell, X. Granados, S. Ricart, I. Van Driessche, a. Palau, T. Puig, and X. Obradors, "Flexible manufacturing of functional ceramic coatings by inkjet printing," *Thin Solid Films*, Sep. 2013.
- [14] D. Cibis, "Influencing Parameters in Droplet Formation for DoD Printing of Conductive Inks," *Proc. 4th Int. Conf. Ceram.*, pp. 417–423, 2008.
- [15] D. Cibis and K. Krüger, "DoD-Printing of Conductive Silver Tracks," no. 0, 2004.
- [16] E. a. Tholén, U. W. Gedde, D. B. Haviland, a. Oko, N. Sanandaji, and M. S. Hedenqvist, "Inkjet printing as a possible route to study confined crystal structures," *Eur. Polym. J.*, vol. 49, no. 1, pp. 203–208, Jan. 2012.
- [17] H. Dong, "Drop-on-demand inkjet drop formation and deposition," Georgia Institute of Technology, 2006.
- [18] S. Jung and I. M. Hutchings, "The impact and spreading of a small liquid drop on a non-porous substrate over an extended time scale," *Soft Matter*, vol. 8, no. 9, p. 2686, 2012.
- [19] W. Hsiao, S. Hoath, G. Martin, and I. Hutchings, "Jetting, In-Nozzle Meniscus Motion and Nozzle-Plate Flooding in an Industrial Drop-on-Demand Print Head," *Proc 27th Int. Conf. Digit. Print. Technol. NIP27*, 2011.
- [20] B. Derby, "Inkjet printing ceramics: From drops to solid," *J. Eur. Ceram. Soc.*, vol. 31, no. 14, pp. 2543–2550, Nov. 2011.
- [21] J. Ebert, E. Özkol, and R. Telle, "An experimental analysis of the influence of the ink properties on the drop formation for direct thermal inkjet printing of high solid content aqueous 3Y-TZP suspensions," *J. Eur. Ceram. Soc.*, vol. 30, no. 7, pp. 1669–1678, May 2010.
- [22] N. Genina, D. Fors, M. Palo, J. Peltonen, and N. Sandler, "Behavior of printable formulations of loperamide and caffeine on different substrates--effect of print density in inkjet printing.," *Int. J. Pharm.*, vol. 453, no. 2, pp. 488–97, Sep. 2013.

- [23] M. Mäntysalo, U. Caglar, P. Mansikkamäki, E. Halonen, S. Koskinen, V. Pekkanen, K. Kaija, E. Kunnari, J. Niittyneen, and K. Laine, "Utilizing inkjet printing to fabricate electrical interconnections in a system-in-package," *Microelectron. Eng.*, vol. 87, no. 11, pp. 2382–2390, Nov. 2010.
- [24] Lord Rayleigh, "On the instability of jets," *Proc. London Math. Soc.*, vol. 10, pp. 4–13, 1878.
- [25] H. Wijshoff, "The dynamics of the piezo inkjet printhead operation," *Phys. Rep.*, vol. 491, no. 4–5, pp. 77–177, Jun. 2010.
- [26] D. Cibis, "Optimization of a DoD Print Head Signal for the Ink-Jetting of Conductive Circuits."
- [27] A. Famili, S. a. Palkar, and W. J. Baldy, "First drop dissimilarity in drop-on-demand inkjet devices," *Phys. Fluids*, vol. 23, no. 1, p. 012109, 2011.
- [28] National Instruments, "Image Acquisition System Setup," *Imaging Fundamentals*, 2011. [Online]. Available: <http://www.ni.com/white-paper/4229/en/>.
- [29] A. Hornberg, *Handbook of Machine Vision*. Weinheim, Germany: Wiley-VCH Verlag GmbH & Co. KGaA, 2006.
- [30] Opto Engineering, "Telecentric Lenses : basic information and working principles," *Telecentric lens tutorial*. [Online]. Available: <http://www.opto-engineering.com/resources/telecentric-lenses-tutorial>.
- [31] National Instruments, "A Practical Guide to Machine Vision Lighting - Part I," *Machine Vision Fundamentals*, 2012. [Online]. Available: <http://www.ni.com/white-paper/6901/en/>.
- [32] National Instruments, "A Practical Guide to Machine Vision Lighting - Part II," *Machine Vision Fundamentals*, 2013. [Online]. Available: <http://www.ni.com/white-paper/6902/en/>.
- [33] National Instruments, "A Practical Guide to Machine Vision Lighting - Part III," *Machine Vision Fundamentals*, 2013. [Online]. Available: <http://www.ni.com/white-paper/6903/en/>.
- [34] L. Rutten, "Cursus Real-time OS." pp. 1–80, 2014.
- [35] Microfab Technologies, "PH-47 product sheet." [Online]. Available: <http://www.microfab.com/images/pdfs/ph-47-mf4>.

- [36] Microfab Technologies, "JetDrive III Drive Electronics." [Online]. Available: http://www.microfab.com/archive/equipment/pdf/jetdrive3_mf1.pdf.
- [37] Allied Vision Technologies GmbH, "AVT Manta Technical Manual," no. September. pp. 1–156, 2013.
- [38] Allied Vision Technologies GmbH, "Technical Drawing : Manta Type A standard housing," vol. 3, 2013.
- [39] Opto Engineering, "TC4M 004-C technical drawing," 2006. [Online]. Available: <http://www.opto-engineering.com/media/downloads/schematics/21579-0-a.pdf>.
- [40] Opto Engineering, "collimated LED illuminator - LTCL023-G.PDF." .
- [41] Seoul Semiconductors, "X42182 technical datasheet," no. May. pp. 1–30, 2013.
- [42] Cree, "XLamp XM-L LEDs Product family data sheet," pp. 1–13, 2013.
- [43] Cree, "Pulsed Over-Current Driving of Cree ® XLamp ® LEDs : Information and Cautions." pp. 1–11, 2012.
- [44] Microfab Technologies, "JetDrive III LabVIEW Interface Manual." 2005.

Appendix A: JetDrive delay measurements data

#	value
1	3,600
2	4,600
3	3,880
4	4,400
5	3,960
6	4,280
7	4,240
8	4,080
9	4,520
10	4,280
11	4,480
12	4,560
13	4,040
14	3,800
15	4,160
16	3,640
17	4,040
18	4,320
19	4,120
20	3,760

#	value
21	4,440
22	4,480
23	4,240
24	4,000
25	3,720
26	3,840
27	4,280
28	4,160
29	4,040
30	4,000
31	3,960
32	4,440
33	4,280
34	4,680
35	3,920
36	4,080
37	4,320
38	4,520
39	4,000
40	4,680

Appendix B: Manta delay measurements data

#	value
1	9,700
2	9,800
3	9,800
4	9,700
5	9,700
6	9,700
7	9,500
8	9,700
9	9,800
10	9,800
11	9,800
12	9,800
13	12,700
14	9,700
15	9,700
16	9,800

#	value
21	12,400
22	14,800
23	9,900
24	9,900
25	9,800
26	9,800
27	9,800
28	9,900
29	9,900
30	14,200
31	9,900
32	9,800
33	9,800
34	10,000
35	9,900
36	12,500

17	9,900
18	10,700
19	9,700
20	14,800

37	9,900
38	9,800
39	9,700
40	9,800

Appendix C: PP880 delay measurements data

#	value
1	1,130
2	1,090
3	1,080
4	1,130
5	1,080
6	1,110
7	1,060
8	1,100
9	1,090
10	1,120
11	1,100
12	1,040
13	1,100
14	1,110
15	1,080
16	1,070
17	1,130
18	1,110
19	1,050
20	1,050

#	value
21	1,070
22	1,120
23	1,120
24	1,050
25	1,070
26	1,090
27	1,080
28	1,130
29	1,080
30	1,120
31	1,080
32	1,040
33	1,050
34	1,100
35	1,080
36	1,130
37	1,120
38	1,110
39	1,040
40	1,040

Appendix D: Drop characterization data

		SATELLITE										
		pixels			μm			μm	m/s	μm	μm^3	pl
t (in μs)	area	xm	ym	area	xm	ym	ydiff	vy	radius	volume		
65	1384,3	333,5	854,3	1216,6	312,6	801,0			19,68	31924	31,92	
70	1433,5	332,6	869,3	1259,9	311,8	814,9	13,99	2,80	20,03	33641	33,64	
75	1484,5	331,3	889,4	1304,7	310,6	833,9	18,91	3,78	20,38	35452	35,45	
80	1476,6	328,7	914,0	1297,8	308,2	856,9	23,04	4,61	20,32	35169	35,17	
85	1517,0	328,7	917,4	1333,3	308,1	860,1	3,18	0,64	20,60	36623	36,62	
90	1495,0	328,0	931,6	1314,0	307,5	873,3	13,27	2,65	20,45	35830	35,83	
95	1502,1	327,5	943,2	1320,2	307,0	884,3	10,96	2,19	20,50	36083	36,08	
100	1510,8	327,0	957,1	1327,9	306,6	897,3	13,03	2,61	20,56	36400	36,40	

105	1560,9	326,6	967,0	1371,9	306,2	906,5	9,19	1,84	20,90	38226	38,23
110	1618,1	325,9	982,0	1422,1	305,5	920,6	14,13	2,83	21,28	40343	40,34
115	1609,3	325,2	997,2	1414,4	304,9	934,9	14,24	2,85	21,22	40015	40,02
120	1609,3	324,9	1008,7	1414,4	304,6	945,6	10,74	2,15	21,22	40015	40,02
125	1575,0	324,1	1020,1	1384,3	303,8	956,4	10,75	2,15	20,99	38743	38,74
130	1569,7	323,6	1038,6	1379,6	303,4	973,7	17,31	3,46	20,96	38549	38,55
135	1604,0	322,9	1053,7	1409,8	302,7	987,8	14,13	2,83	21,18	39819	39,82
140	1656,7	322,5	1070,0	1456,1	302,3	1003,1	15,32	3,06	21,53	41798	41,80
145	1654,1	322,0	1077,4	1453,8	301,9	1010,0	6,90	1,38	21,51	41699	41,70
150	1641,8	321,4	1092,7	1443,0	301,3	1024,4	14,40	2,88	21,43	41234	41,23
155	1630,4	321,3	1099,6	1432,9	301,2	1030,9	6,42	1,28	21,36	40804	40,80
160	1633,9	320,6	1112,9	1436,0	300,6	1043,3	12,47	2,49	21,38	40936	40,94
165	1646,2	319,8	1134,7	1446,8	299,8	1063,8	20,46	4,09	21,46	41400	41,40
170	1672,6	319,0	1155,2	1470,0	299,0	1083,0	19,24	3,85	21,63	42398	42,40
175	1694,5	318,8	1161,1	1489,3	298,8	1088,5	5,46	1,09	21,77	43237	43,24
180	1669,0	317,8	1175,1	1466,9	297,9	1101,7	13,18	2,64	21,61	42265	42,26
AVERAGE VALUES								2,61	21,00		38,86
area	xm	ym	area	xm	ym	ydifff	vy	radius	volume		
pixels			µm			µm	m/s	µm	µm ³	pl	

MAIN

t (in µs)	pixels			µm			µm	m/s	µm	µm ³	pl
	area	xm	ym	area	xm	ym	ydifff	vy	radius	volume	
95	2758,9	336,0	731,3	2424,8	315,0	685,6			27,78	89821	89,82
100	2448,6	335,8	738,0	2152,1	314,9	691,9	6,32	1,26	26,17	75104	75,10
105	2340,5	335,6	745,4	2057,1	314,6	698,8	6,90	1,38	25,59	70186	70,19
110	2127,0	335,4	753,5	1869,4	314,4	706,4	7,64	1,53	24,39	60802	60,80
115	1880,9	335,1	758,1	1653,1	314,2	710,8	4,32	0,86	22,94	50561	50,56
120	1989,8	335,2	763,6	1748,9	314,2	715,8	5,09	1,02	23,59	55018	55,02
125	2181,4	334,7	771,4	1917,3	313,8	723,2	7,35	1,47	24,70	63153	63,15
130	2418,8	334,5	777,1	2125,9	313,6	728,5	5,30	1,06	26,01	73733	73,73
135	2448,6	334,4	782,3	2152,1	313,5	733,4	4,89	0,98	26,17	75104	75,10
140	2301,0	334,2	786,4	2022,3	313,3	737,3	3,91	0,78	25,37	68414	68,41
145	2110,3	334,1	795,1	1854,7	313,2	745,4	8,10	1,62	24,30	60087	60,09
150	1874,7	333,8	802,4	1647,7	312,9	752,3	6,87	1,37	22,90	50313	50,31
155	1933,6	333,8	805,5	1699,4	313,0	755,2	2,90	0,58	23,26	52702	52,70
160	2097,9	333,5	811,3	1843,9	312,7	760,6	5,43	1,09	24,23	59562	59,56
165	2276,4	333,5	817,5	2000,7	312,6	766,4	5,78	1,16	25,24	67320	67,32
170	2344,0	333,3	823,5	2060,2	312,5	772,0	5,62	1,12	25,61	70344	70,34
175	2260,5	333,2	828,6	1986,8	312,3	776,8	4,83	0,97	25,15	66619	66,62
180	2127,0	332,7	834,5	1869,4	311,9	782,3	5,52	1,10	24,39	60802	60,80
185	2043,5	332,6	840,2	1796,0	311,8	787,7	5,39	1,08	23,91	57257	57,26
190	1960,0	332,5	846,0	1722,6	311,8	793,1	5,39	1,08	23,42	53783	53,78
195	2104,1	332,5	851,7	1849,3	311,7	798,5	5,38	1,08	24,26	59824	59,82

200	2240,3	332,4	857,7	1969,0	311,6	804,1	5,57	1,11	25,04	65727	65,73
205	2268,5	332,2	863,2	1993,8	311,4	809,3	5,21	1,04	25,19	66969	66,97
210	2221,9	332,0	868,9	1952,8	311,3	814,6	5,36	1,07	24,93	64917	64,92
215	2080,4	332,0	874,4	1828,5	311,2	819,8	5,17	1,03	24,12	58815	58,82
220	1986,3	331,7	880,9	1745,8	311,0	825,9	6,07	1,21	23,57	54872	54,87
225	2006,5	331,4	886,3	1763,6	310,7	830,9	5,06	1,01	23,69	55712	55,71
230	2124,3	331,2	892,2	1867,1	310,5	836,4	5,51	1,10	24,38	60688	60,69
235	2206,9	331,1	898,1	1939,7	310,4	841,9	5,51	1,10	24,85	64263	64,26
240	2233,3	330,9	903,7	1962,9	310,2	847,3	5,31	1,06	25,00	65418	65,42
245	2172,7	330,9	908,8	1909,6	310,2	852,0	4,75	0,95	24,65	62772	62,77
250	2089,2	330,5	915,2	1836,2	309,9	858,0	5,95	1,19	24,18	59188	59,19
255	2013,6	330,4	920,8	1769,7	309,8	863,3	5,31	1,06	23,73	56005	56,01
260	2041,7	330,3	925,6	1794,5	309,7	867,8	4,50	0,90	23,90	57183	57,18
265	2123,4	330,3	932,0	1866,3	309,6	873,8	6,00	1,20	24,37	60651	60,65
270	2204,3	329,7	937,0	1937,4	309,1	878,5	4,71	0,94	24,83	64148	64,15
275	2213,1	329,5	943,3	1945,1	308,9	884,3	5,85	1,17	24,88	64532	64,53
280	2138,4	329,5	948,6	1879,4	308,9	889,3	5,01	1,00	24,46	61292	61,29
285	2063,7	329,4	954,0	1813,8	308,8	894,4	5,01	1,00	24,03	58108	58,11
290	2054,9	329,4	960,6	1806,0	308,8	900,6	6,22	1,24	23,98	57738	57,74
295	2078,6	329,3	966,4	1826,9	308,7	906,0	5,43	1,09	24,11	58741	58,74
300	2152,4	328,7	972,0	1891,8	308,2	911,2	5,21	1,04	24,54	61898	61,90
305	2185,8	328,8	977,7	1921,1	308,3	916,6	5,40	1,08	24,73	63344	63,34
310	2141,9	328,7	984,3	1882,5	308,2	922,7	6,11	1,22	24,48	61443	61,44
315	2097,9	328,6	990,8	1843,9	308,0	928,8	6,11	1,22	24,23	59562	59,56
320	2078,6	328,2	996,5	1826,9	307,7	934,2	5,32	1,06	24,11	58741	58,74
325	2059,3	327,8	1002,1	1809,9	307,3	939,5	5,32	1,06	24,00	57923	57,92
330	2094,4	328,0	1006,5	1840,8	307,5	943,6	4,12	0,82	24,21	59412	59,41
335	2144,5	327,6	1012,1	1884,8	307,2	948,9	5,25	1,05	24,49	61557	61,56
340	2187,6	327,6	1016,6	1922,7	307,1	953,0	4,16	0,83	24,74	63420	63,42
345	2188,5	327,4	1022,3	1923,5	307,0	958,4	5,41	1,08	24,74	63459	63,46
350	2136,6	327,0	1029,2	1877,9	306,5	964,9	6,42	1,28	24,45	61217	61,22
355	2103,2	327,2	1034,2	1848,5	306,8	969,5	4,67	0,93	24,26	59787	59,79
360	2092,7	327,0	1040,5	1839,3	306,6	975,5	5,96	1,19	24,20	59338	59,34
365	2119,0	327,0	1046,1	1862,4	306,6	980,7	5,25	1,05	24,35	60463	60,46
370	2162,1	326,6	1051,8	1900,3	306,2	986,0	5,30	1,06	24,59	62315	62,32
375	2186,7	326,4	1057,9	1921,9	306,0	991,8	5,77	1,15	24,73	63382	63,38
380	2170,0	326,6	1062,5	1907,2	306,2	996,1	4,31	0,86	24,64	62658	62,66
385	2141,9	325,9	1068,0	1882,5	305,6	1001,2	5,13	1,03	24,48	61443	61,44
390	2094,4	325,8	1073,6	1840,8	305,4	1006,5	5,26	1,05	24,21	59412	59,41
395	2097,9	325,7	1079,0	1843,9	305,4	1011,6	5,05	1,01	24,23	59562	59,56
400	2129,6	325,5	1085,3	1871,7	305,2	1017,5	5,94	1,19	24,41	60915	60,91
405	2170,0	325,5	1090,6	1907,2	305,2	1022,5	4,98	1,00	24,64	62658	62,66
410	2179,7	324,9	1095,8	1915,7	304,6	1027,4	4,87	0,97	24,69	63077	63,08
415	2163,9	324,9	1101,7	1901,8	304,6	1032,9	5,53	1,11	24,60	62391	62,39
420	2148,0	324,8	1107,2	1887,9	304,5	1038,0	5,13	1,03	24,51	61708	61,71

425	2130,5	324,5	1112,6	1872,5	304,2	1043,1	5,06	1,01	24,41	60952	60,95
430	2115,5	324,8	1117,9	1859,3	304,5	1048,1	4,99	1,00	24,33	60312	60,31
435	2152,4	324,3	1123,8	1891,8	304,0	1053,6	5,52	1,10	24,54	61898	61,90
440	2156,0	324,6	1128,9	1894,9	304,3	1058,3	4,73	0,95	24,56	62049	62,05
445	2169,1	323,9	1135,1	1906,5	303,6	1064,2	5,88	1,18	24,63	62619	62,62
450	2166,5	323,8	1140,5	1904,2	303,6	1069,3	5,07	1,01	24,62	62505	62,51
455	2140,1	324,1	1149,8	1881,0	303,9	1078,0	8,73	1,75	24,47	61368	61,37
460	2142,8	323,5	1151,1	1883,3	303,3	1079,1	1,13	0,23	24,48	61481	61,48
465	2174,4	322,9	1157,4	1911,1	302,8	1085,1	5,99	1,20	24,66	62848	62,85
470	2187,6	323,2	1166,1	1922,7	303,0	1093,2	8,10	1,62	24,74	63420	63,42
475	2212,2	323,0	1169,6	1944,3	302,8	1096,5	3,30	0,66	24,88	64494	64,49
480	2192,0	322,7	1175,0	1926,6	302,6	1101,6	5,10	1,02	24,76	63612	63,61
AVERAGE VALUES								1,08	25,86		65,36
area	xm	ym	area	xm	ym	ydiff	vy	radius	volume		
pixels			μm			μm	m/s	μm	μm^3	pl	

Auteursrechtelijke overeenkomst

Ik/wij verlenen het wereldwijde auteursrecht voor de ingediende eindverhandeling:
Flash photography vision system for inkjet drop formation characterization

Richting: **master in de industriële wetenschappen: elektronica-ICT**
Jaar: **2014**

in alle mogelijke mediaformaten, - bestaande en in de toekomst te ontwikkelen - , aan de Universiteit Hasselt.

Niet tegenstaand deze toekenning van het auteursrecht aan de Universiteit Hasselt behoud ik als auteur het recht om de eindverhandeling, - in zijn geheel of gedeeltelijk -, vrij te reproduceren, (her)publiceren of distribueren zonder de toelating te moeten verkrijgen van de Universiteit Hasselt.

Ik bevestig dat de eindverhandeling mijn origineel werk is, en dat ik het recht heb om de rechten te verlenen die in deze overeenkomst worden beschreven. Ik verklaar tevens dat de eindverhandeling, naar mijn weten, het auteursrecht van anderen niet overtreedt.

Ik verklaar tevens dat ik voor het materiaal in de eindverhandeling dat beschermd wordt door het auteursrecht, de nodige toelatingen heb verkregen zodat ik deze ook aan de Universiteit Hasselt kan overdragen en dat dit duidelijk in de tekst en inhoud van de eindverhandeling werd genotificeerd.

Universiteit Hasselt zal mij als auteur(s) van de eindverhandeling identificeren en zal geen wijzigingen aanbrengen aan de eindverhandeling, uitgezonderd deze toegelaten door deze overeenkomst.

Voor akkoord,

Nagels, Steven

Datum: **6/06/2014**